Forced Response Predictions in Modern Centrifugal Compressor Design

by

Caitlin J. Smythe

B.S. (Aerospace Engineering) University of California, San Diego (2002)

Submitted to the Department of Aeronautics and Astronautics in partial fulfillment of the degree of

Master of Science

at the

MASSACHUSETTS INSTITUTE OF TECHNOLOGY

June 2005

Author ..... Department of Aeronautics and Astronautics
May 20, 2005

Certified by..
Choon S. Tan
Senior Research Engineer, Gas Turbine Laboratory
Thesis Supervisor

Certified by... .....
Jaime Peraire
Professor of Aeronautics and Astronautics
Chair, Committee on Graduate Students

Forced Response Predictions in Modern Centrifugal Compressor Design

by

Caitlin J. Smythe

Submitted to the Department of Aeronautics and Astronautics on May 20, 2005 in partial fulfillment of the requirements for the degree of Master of Science

Abstract

A computational interrogation of the time-averaged and time-unsteady flow fields of two centrifugal compressors of nearly identical design (the enhanced, which encountered aeromechanical difficulty, and production, which did not encounter any such difficulty) is undertaken in an effort to establish a causal link between impeller-diffuser interactions and the forced response behavior of the impeller blades. Through comparison of time-averaged flow variable and performance estimates with test rig data, the three-dimensional, unsteady, Reynolds-averaged Navier-Stokes flow solver (MSU Turbo) used in this interrogation is found to be adequate to the task of distinguishing the flow fields of the two centrifugal compressor designs. Thus, it is found that MSU Turbo can be a useful tool in comparing the unsteady flow fields in different centrifugal compressors. In addition, through comparisons of MSU Turbo/ ANSYS® estimates of strain with measured peak strain, MSU Turbo is also found to have the potential, as part of a CFD/ ANSYS® system, for serving as a predictive tool for forced response behavior in centrifugal compressors.

Differences are found in the unsteady flow fields of the two compressors. The fluctuations over time of the unsteady blade loading on the enhanced impeller blades are greater than those on the production impeller blades. In the vaneless space, on each annular plane (from the impeller exit to the diffuser inlet), at a given spanwise location, the enhanced compressor has both a greater spatial variation in pressure and a higher average static pressure than the production compressor. At the diffuser inlet, there are differences in the time-averaged incidence angle distributions of the two compressors.

Based on the observations delineated above, it is hypothesized that the differences in the time-averaged incidence angle distributions are the source of the differences in the pressure field that propagates upstream into the impeller passage, where these differences affect the unsteady blade loading. The differences in the unsteady blade loading then lead to the observed forced response behavior in the two designs.

Thesis Supervisor: Dr. Choon S. Tan
Title: Senior Research Engineer, Gas Turbine Laboratory

Acknowledgements

This research was sponsored by the GUIDE III Consortium under subcontract 127235-1150027 to the Air Force Prime contract F33615-01-C-2186 with Dr. C. Cross as Contract Monitor and with Dr. J. Griffins as subcontract monitor via Carnegie-Mellon University.

I am grateful to the following people that provided help in enabling the successful execution of MSU Turbo on the MIT Gas Turbine Laboratory Computer System: Dr. J. P. Chen and Dr. M. Remotigue and their colleagues of Mississippi State University, Dr. S. Gorrell and Mr. D. Car of the Compressor Research Laboratory (CARL) in the Air Force Research Laboratory (AFRL), Mr. R. Haimes of the MIT ACDL and Mr. P. Warren of the MIT Gas Turbine Laboratory.

I am also grateful to Honeywell Engines, Systems and Services (Honeywell ES&S) for permitting me to work at their facility over the summer, giving the research project a good jumpstart. I am grateful for the help of my coworkers at Honeywell ES&S. Thanks to Dr. J. Liu, my mentor at Honeywell, who provided endless support (both technical and administrative) before, during, and after my visit. Thanks also to Mahmoud Mansour for his contributions for the ADPAC analysis, for his help in getting the TURBO simulations to converge and for is help in understanding the results once converged solutions were obtained. Thanks also to Mr. J. Lentz for his help in understanding the test data results. Finally, thanks go to Dr. J. Panovsky for his advice and technical knowledge, for performing the ANSYS® calculations, and for facilitating the entire project.

My thesis advisor, Dr. Choon Tan provided council and technical guidance throughout my time in the MIT Gas Turbine Lab with a seemingly unending supply of patience.

I would also like to thank the GTL staff for their support, especially:
Dr. Yifang Gong for his technical advice and technical support. Ms. Lori Martinez, Ms. Julie Finn, and Ms. Holly Anderson for their administrative support.

A special thanks goes to Mr. Alfonso Villanueva (a fellow GTL student) for his help with unsteady data post-processing and for his programming expertise.

Table of Contents

Nomenclature

Acronyms and Abbreviations

3-D	3-dimensional
CFD	Computational Fluid Dynamics
corr	Corrected
Cp	Diffuser Pressure Recovery Coefficient
E	Engine Order or Excitation Order
FEA	Finite Element Analysis
FFT	Fast Fourier Transform
HCF	High Cycle Fatigue
Honeywell ES&S	Honeywell Engines, Systems and Services
IDI	Impeller-Diffuser Interaction
LE	Leading Edge
Mass 1	Corrected Flow at which investigation is performed, near design
Mass 2	Corrected Flow at which investigation is performed, near stall
PS	Pressure Surface
RANS	Reynolds-averaged Navier-Stokes
rev	Revolution
SS	Suction Surface
TE	Trailing Edge
TURBO	MSU Turbo

Symbols

°	Degree
α	Flow Angle or Swirl Angle
A	Area
C_L	Center Line
E	Energy
dP	Pps-Pss
i	Flow Direction
j	Spanwise Direction
k	Pitchwise Direction
m	Mass Flow
$\hat{n}$	Unit Vector Normal to the Plane
N	Number of Steps Recorded Over One Period
Π	Pressure ratio
Ps	Static Pressure
ΔPs	Unsteady Pressure Loading
Pps	Static Pressure on the Pressure Surface
Pss	Static Pressure on the Suction Surface
Pt	Total Pressure
ρ	Density
rho	Density
s	Entropy
Δs	Entropy generation
utip	Impeller Tip Velocity
u	Velocity Component in the x-direction
v	Velocity Component in the y-direction
v_r	Radial Velocity

v_θ	Tangential Velocity
w	Velocity Component in the z-direction
Wc	Corrected flow
x	x-coordinate
y	y-coordinate
z	z-coordinate

Subscripts

exit	Diffuser Exit
in	Impeller Inlet
inlet	Diffuser Inlet
max	Maximum
min	Minimum
t	total
tip	Impeller Blade Tip

Operators

^	Mass-averaged
-	Mass-averaged then Time-averaged
.	Time-averaged
$\rightarrow$	Vector Quantity

List of Figures

List of Tables

Chapter 1

Introduction and Technical Background

1.1 Background and Motivation

1.1.1 The Centrifugal Compressor

Centrifugal compressors (Figure 1.1) are used in a wide variety of gas turbine applications from small power plants to aircraft engines as well as in industrial applications. Each application has different design requirements and constraints leading to large variations in compressor geometries. For example, an aircraft engine must be as compact and as light as possible, while for ground-based power plants, weight is not an important design parameter. In addition, the higher rotating speeds of aircraft engines require that close attention be paid to the stresses in the blades.

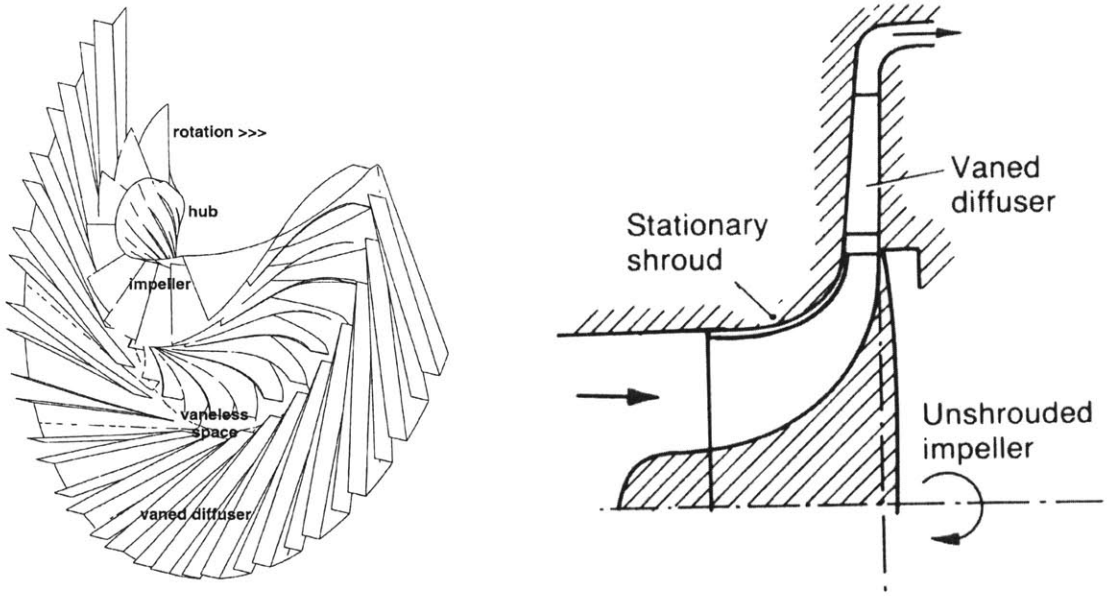

Figure 1.1 - Schematic of a typical centrifugal stage with a vaned diffuser from Krain [3] and the simplified meridional section of a typical centrifugal compressor from Cumpsty [1].

Like axial compressors stages, a centrifugal compressor stage is comprised of a rotating component (the impeller) and a stationary component (the diffuser). However, while the blade-rows in the axial compressor are relatively similar, the impeller and the diffuser are very different [1]. This difference in the similarity of the blade-rows also yields differences in the similarities of the flow paths in the two blade-rows. The flow in the rotor and stator of the axial stages remains mainly axial and/or tangential. By contrast, while the impeller turns the flow from mainly axial and tangential to mostly radial and tangential, the diffuser maintains the radial and tangential flow field exiting the impeller. The other major difference between axial and centrifugal compressors lies in the origin of the pressure rise. In axial compressors, the sole source of pressure rise comes from the translation of kinetic energy to thermal energy by diffusion throughout each stage. On the other hand, the centrifugal compressor gains much of its pressure rise through the change in potential energy of the fluid as the fluid moves radially outward in the impeller. The pressure rise due to this centrifugal force field is not subject to problems with boundary-layer growth and flow separation [2], so a centrifugal compressor stage can attain a higher pressure ratio than a singe axial stage.

The impeller has an axial inlet and radial outlet and is composed of several components: inducer, main blades, splitter blades, hub, and shroud (or casing). The inducer is the (nearly) axial inlet to the impeller and it turns the inlet flow to the angular velocity of the rotor. Torque is applied to the flow by the impeller main blades, which run the length of the impeller flow passage and are attached to the rotating hub. The greater the number of blades, the lower the blade loading is on each blade. In some cases, it is necessary to divide the flow passages further by the addition of splitter blades in order to decrease the blade loading to an acceptable level. The leading edge of the splitter blades are located some distance downstream of the leading edge of the impeller main blades to avoid choking the flow at the inlet, or inducer, region (by avoiding a decrease in effective flow area). The shroud, which covers the impeller, may either rotate with the impeller or remain stationary. A rotating shroud is attached to the rotor by the tips of the impeller blades. Stationary casings are used for applications that run at high rotational speeds, such as aircraft engines, because the stresses on the blades caused by an attached shroud

would be unacceptable. In this case, the shroud is separated from the impeller blade tips by the tip clearance region.

The diffuser is a stationary annular passage that may be separated by blades (a vaned diffuser) or may be left as a single passage (a vaneless diffuser). The purpose of the diffuser is to recover the dynamic pressure head from the flow that exits the impeller at high velocities, yielding a higher pressure rise than the impeller alone. Diffusers have a radial inlet, while the exit plane is dependent on the particular application. Flow into the diffuser is radial with inlet swirl imparted by the impeller blades. The diffuser inlet flow is non-uniform, a result associated with the jet and wake flow structure of the flow exiting the impeller.

The space in the flow path between the impeller and the diffuser without vanes is called the vaneless space or the impeller-diffuser gap. The size of this region affects the degree to which the impeller and the diffuser interact with each other, and hence the likelihood of encountering high cycle fatigue.

1.1.2 High Cycle Fatigue

High cycle fatigue (HCF) is a phenomenon that can lead to catastrophic failures in gas turbine engines. HCF occurs when the vibratory stress in a component exceeds the material capability. There are two major types of vibratory problems encountered in centrifugal compressors, both of which contribute to HCF: flutter, which consists of self-excited oscillations near the natural frequency of the blades, and forced response. Forced response is the vibratory response of a system to external excitations and occurs at multiples of the rotational frequency of the rotor. A common source of excitations on the blades in turbomachinery is the unsteady interaction of the rotor and the stator.

Demands for increased performance and lighter weight in advanced engine designs call for smaller gaps between rotors and stators, which lead to reduced engine size and higher

pressure ratios. Such modern design requirements tend to increase the blade row interaction effects and the likelihood of encountering HCF problems. Currently, HCF cannot be predicted in the early design stage and problems are not discovered until testing or in the field, at which point the cost to redesign is high and the redesign is often at the expense of compressor performance. Existing methods for avoiding HCF in the design process is to use Campbell diagrams (see Figure 1.2) to predict which frequencies will excite a vibratory response.

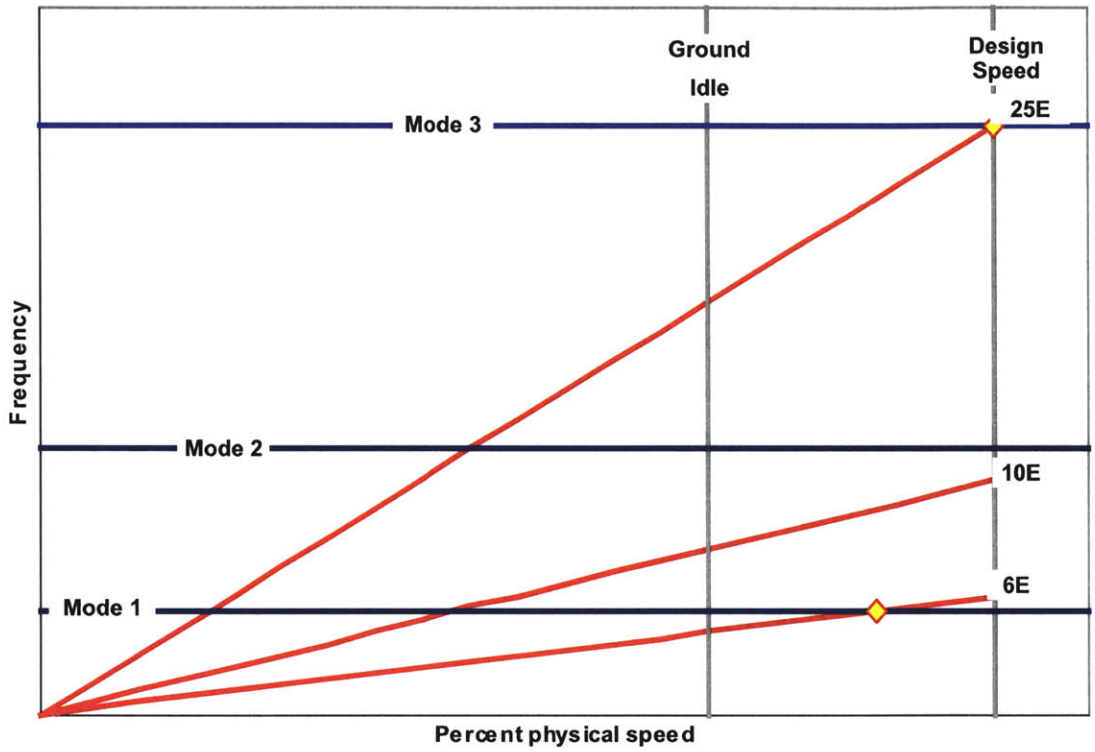

Figure 1.2 - A typical Campbell diagram. The horizontal lines correspond to the vibratory modes, and the red lines are engine orders.

This method cannot predict the strength of the vibratory response at any given frequency, and because all modes cannot be avoided, past experience is used to determine which modes to avoid in design. This reliance on assumptions based on past experience is insufficient for avoiding HCF in advanced engine designs. A more cost-effective method for avoiding HCF is to use computational methods and models to predict HCF early in the design process. Such methods have been widely used for axial stages but significantly less work has been done for centrifugal compressor stages, which are more challenging due to the inherently three-dimensional, unsteady nature of the flow field in

centrifugal machines and the difficulty of modeling the relatively more complicated geometries using CFD.

1.2 Previous Work

In the past twenty years or so, there have been several papers investigating various aspects of the flow field in centrifugal compressors [3-25]. Krain [3,4] studied the effects of vaned and vaneless diffusers on the compressor flow field experimentally. Other papers [5-11, 14-25] examine various aspects of the flow field using various computational fluid dynamic (CFD) tools. In early studies using computational tools, the focus is on determining the ability of computational tools to accurately model flow in centrifugal compressors [5,9,10]. These papers lay the groundwork for using computational methods to perform flow field studies that would have been difficult, if not impossible, to perform experimentally due to difficulty in instrumentation of turbomachinery [6,11]. New studies [24,25] are pushing the limits of CFD tools, modeling flow in increasingly difficult geometries.

Previous research on impeller-diffuser interaction (IDI) in centrifugal compressors has focused on the impact of IDI on compressor performance [7-24]. Using CFD, Phillips [16] found that the pressure rise in the diffuser is strongly affected by flow angle misalignment with the centerline of the diffuser, a finding that was in accord with the experimental investigations of Filipenco [12]. Shum and Shum et al. [18,19] conducted a study using Dawe's UNNEWT code to determine the effect of IDI on centrifugal compressor stage performance. The findings from this study show that the most influential effect of IDI on performance was its effect on tip leakage flow. With increased interaction, and thus increased fluctuations in tip leakage flow, it was found that there are three competing effects: reduced slip (performance benefit), reduced blockage (performance benefit), and increased loss (performance degradation). Due to these competing effects, it was found that there was an optimum radial gap between the

impeller and the diffuser for a maximum impeller performance enhancement; this finding is in accord with the experimental measurements of Rodgers [11]. Building upon Shum's work, Murray (2002) [22] and Murray and Tan (2004) [23] studied the effect of variations in the impeller-diffuser gap and the diffuser vane number on compressor performance. Murray put forward the hypothesis that the effect of these changes in the compressor can be characterized by the non-dimensional ratio of impeller-diffuser gap to diffuser vane pitch. Ziegler et al. [20,21] shed further light on the effect of IDI through experimental testing. In these experiments, it was determined that a change in the impeller-diffuser gap affects both the impeller and the diffuser flow. It was found that a smaller gap causes a smaller wake region at the impeller exit. At the same time, a greater amount of the wake flow is incident upon the diffuser vane pressure surface, which reduces diffuser blade loading and improves diffusion (and thus yields a higher pressure recovery and efficiency). The flow field at the diffuser exit becomes more homogeneous with decreasing radial gap size.

Only recently has the focus been turned to addressing HCF difficulties. The possibility of using computational methods to analyze forced response and predict the occurrence of HCF in centrifugal compressors has previously been explored by Mansour and Kruse [25]. Their predictions of peak strain values on impeller splitter blades using a system of CFD and FEA (finite element analysis) codes compared reasonably with available strain gauge data, giving rise to the inference that HCF predictions using computational methods are entirely feasible. This analysis, though thorough, relied upon the use of a CFD code that did not allow for implementation of phase-lag boundary conditions. Because it did not allow phase-lag boundary conditions, the blade counts had to be modified in the CFD simulations to make the calculation wall-clock times reasonable by avoiding modeling the entire wheel.

1.3 Technical Objectives

The overall goal of this research program is to establish the causal link between the impeller-diffuser interactions and observed aeromechanical difficulties in centrifugal compressor stages. The specific technical objectives are to:

(i) determine the mechanisms in the flow field most responsible for causing the unsteady blade-loading that leads to HCF.

(ii) evaluate a system of computational fluid dynamics (CFD) and structural dynamics analysis as a tool for predicting HCF and determine the necessary elements for an adequate HCF predictive system for centrifugal machines.

To accomplish the goals delineated above, the following questions must be addressed:

(i) What effect does changing the vaneless space (between the impeller exit and the diffuser inlet) have on unsteady impeller-diffuser interactions (i.e. the unsteady pressure field), and hence the loading on the impeller blades)?

(ii) What are the conditions under which a change in the impeller-diffuser gap would lead to aeromechanical difficulty?

(iii) How does the vibratory response estimated by the system of unsteady computational fluid dynamics (CFD) code and structural dynamics analysis compare to test data from a compressor test rig?

1.4 Contributions of thesis

The main contributions of this thesis are twofold:

(1) MSU Turbo is assessed as a computational tool for analyzing the flow field and the time-averaged performance of centrifugal compressor stages by:

- demonstrating the ability of MSU Turbo to generate distinct performance characteristics for two centrifugal compressor stages of nearly identical design: one being the production stage and the other the enhanced stage in which the impeller-diffuser gap has been marginally reduced by growing the impeller tip radius;
- demonstrating the capability of MSU Turbo to generate a computed flow field that is adequate for distinguishing the performance of the enhanced stage from that of the production stage in accordance with the design intent and the test results;
- determining that the unsteady pressure distribution at the impeller trailing edge region of the enhanced stage is consistently stronger than that of the production stage;
- demonstrating that the use of MSU Turbo to compute unsteady flow in an impeller stage, in conjunction with ANSYS® structural dynamic code, yields a trend in the strain level of the impeller blades that is in accord with compressor test rig data.

(2) A hypothesis is formulated: the difference in the time-averaged incidence angle distribution at the diffuser inlet for the two designs results in the observed difference in the unsteady pressure distribution at the impeller trailing edge region, and thus leading to the observed aeromechanical difficulty in one design and not in the other

1.5 Thesis Outline

This thesis is organized as follows:

Chapter 2:

This chapter describes the basic methodology used to investigate the HCF problem. First the technical background is presented. The two centrifugal compressor stages of nearly identical design that are used as research vehicles in the ensuing analysis are described. The motivation for the use of these two compressors in addressing the research questions delineated in Section 1.3 is rationalized. The CFD code that was selected for computing the unsteady three-dimensional flow in the two centrifugal compressors, as well as its use in conjunction with the finite element analysis code ANSYS to estimate the peak strain on each blade, is described.

Chapter 3:

This chapter presents the use of MSU Turbo (TURBO) to generate the performance characteristic of the enhanced and the production stages. This is followed by a presentation of computed strain results from the use of the TURBO/ ANSYS® analysis system for assessment against results from using the ADPAC/ ANSYS® analysis system as well as against available strain gauge data from rig tests. Finally, the computed time-averaged performance of the enhanced stage is contrasted against that of the production stage, and this computed change in performance is compared with previous works.

Chapter 4:

This chapter investigates the sources of the unsteadiness leading to HCF in centrifugal compressors by comparing the flow fields in the impeller and diffuser of the production and enhanced compressors that were obtained by implementing TURBO at the same corrected mass flow for the two compressors. Based on observations made from this

comparison, a hypothesis on the source of the unsteadiness leading to HCF is put forward.

Chapter 5:

This chapter presents a summary of the assessment of the use of TURBO as an analysis and design tool both as a stand-alone CFD code and in combination with FEA tools. It then gives an overview of the comparison between the flow fields of the two compressors. In addition, a hypothesis is presented regarding the source of HCF in centrifugal compressors. Based upon these conclusions, recommendations are put forth for future work needed in this area.

Chapter 2

Technical Approach

2.1 Research Articles: Production vs. Enhanced

To achieve the goals set forth in Section 1.3, two similar centrifugal compressor designs from Honeywell Engines, Systems, & Services (Honeywell ES&S) are examined, building upon previous research performed by Mansour and Kruse [25] on the same compressor designs. The first design is a production compressor. The second compressor is a redesign of the production compressor and is called the enhanced compressor. Both the production and enhanced impeller designs have 17 main and 17 splitter blades and are designed as the first stage of a two-stage centrifugal compressor. Both impellers have non-rotating shrouds that are separated from the blade tips by the same end gap. To produce the enhanced design, the production impeller was modified slightly in both its structural and aerodynamic characteristics in order to achieve a higher pressure ratio. The main difference between the two impellers is a larger impeller exit radius for the enhanced version, resulting in a .55-point decrease in vaneless space and an increase in diffuser inlet Mach number from high subsonic to transonic. Both impellers are designed to use the same 25-vane diffuser.

Although these two impellers are similar in design, they exhibit significant differences in response to the unsteady aerodynamic loads encountered. While the enhanced geometry attained the expected increase in performance during testing, it also encountered strains in the impeller splitter blade high enough to raise HCF concerns. The production geometry had experienced no such difficulties either during testing or in the field. During testing, the maximum strains for both geometries occurred on the pressure surface of the impeller splitter blade at the 25 per rev frequency. This frequency is the same as the blade passing frequency, which indicates that the splitter blade vibrations were excited by impeller-diffuser interactions (IDI). Referring to the Campbell diagrams for

the two compressors (see Figure 2.1), it can be seen that many modes were excited at the 25th engine order. However, none of these excitations caused strains high enough for concern in the production compressor. The highest strain occurred in the 4th mode for the production impeller, and of the mode crossings occurring at the 25th engine order, only the 5th mode caused HCF problems (indicated by the yellow dot on the Campbell diagram Figure 2.1b) in the enhanced compressor.

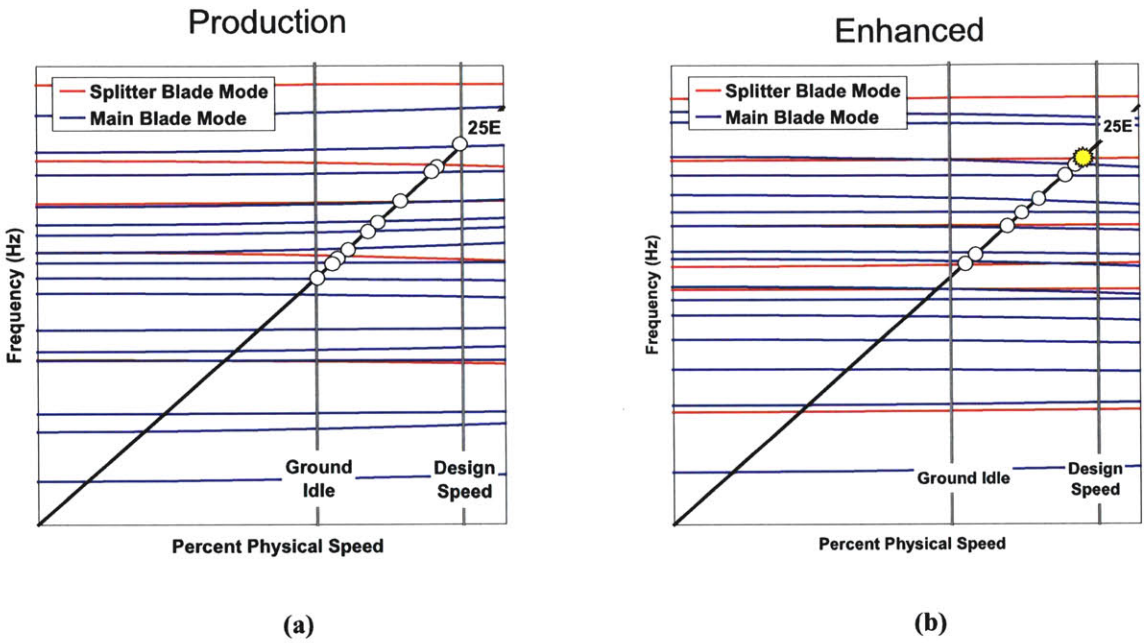

Figure 2.1 - Campbell diagrams for the production and enhanced compressors. The yellow speed crossing is the speed and vibratory mode at which HCF concerns were encountered.

2.2 Computational Tool Description

The system of computational tools used to estimate peak strain on the impeller blades involves the use of both CFD and structural analysis codes. In this system, unsteady pressures on the surfaces of the blades are obtained from time-unsteady simulations of three-dimensional (3-D) flow in the centrifugal stage using MSU Turbo [26]. Forced response analyses are then performed via ANSYS®, a structural analysis code, using the unsteady pressures obtained from the CFD simulations as the excitation force. This

methodology has been explored and assessed previously by Mansour and Kruse [25], using the CFD code Advanced Ducted Propfan Analysis Code (ADPAC) [27].

2.2.1 CFD Simulation

2.2.1.1 MSU TURBO Code Description

MSU Turbo is a multi-block CFD code that uses an implicit time-accurate scheme to solve the 3-D, unsteady, Reynolds-averaged Navier-Stokes (RANS) equations. This CFD code was developed by J. P. Chen of Mississippi State University [26] and may be run in series or in parallel. The multi-block capability enables modeling of complicated geometries, while the ability to run in parallel allows for shorter wall clock times, making this code ideal for modeling complicated turbomachinery such as centrifugal compressors. In order to reduce calculation wall clock times, the parallel version was used for this project. The main advantage of TURBO over other CFD codes is that it can implement phase-lag boundary conditions. Phase-lag boundary conditions allow for modeling of a single blade passage for each blade row by storing time-varying data for a single blade-passing period. Use of these boundary conditions makes it possible to simulate flow through the correct geometry without modeling the entire wheel, decreasing the wall clock time required for each iteration. By modeling the exact geometry, the simulation yields the correct blade passing frequencies, the correct throat area, and hence presumably the associated Mach number distribution.

2.2.1.2 Computational Grids

The TURBO computational grids for both the enhanced and the production compressors were created at Honeywell ES&S. Each geometry is represented by five computational blocks that are in a structured (hexahedral cells), multi-grid format (see Figure 2.2 and Figure 2.3). Blocks 1-4 are part of the rotating component. Block 1 models the inducer region. Blocks 2 and 3 each model half of the impeller; blocks 2 and 3 together form one impeller passage, bounded by the impeller main blade pressure surface on one side of the

passage and the impeller main blade suction surface on the other. Block 4 models part of the vaneless space between the impeller and the diffuser.

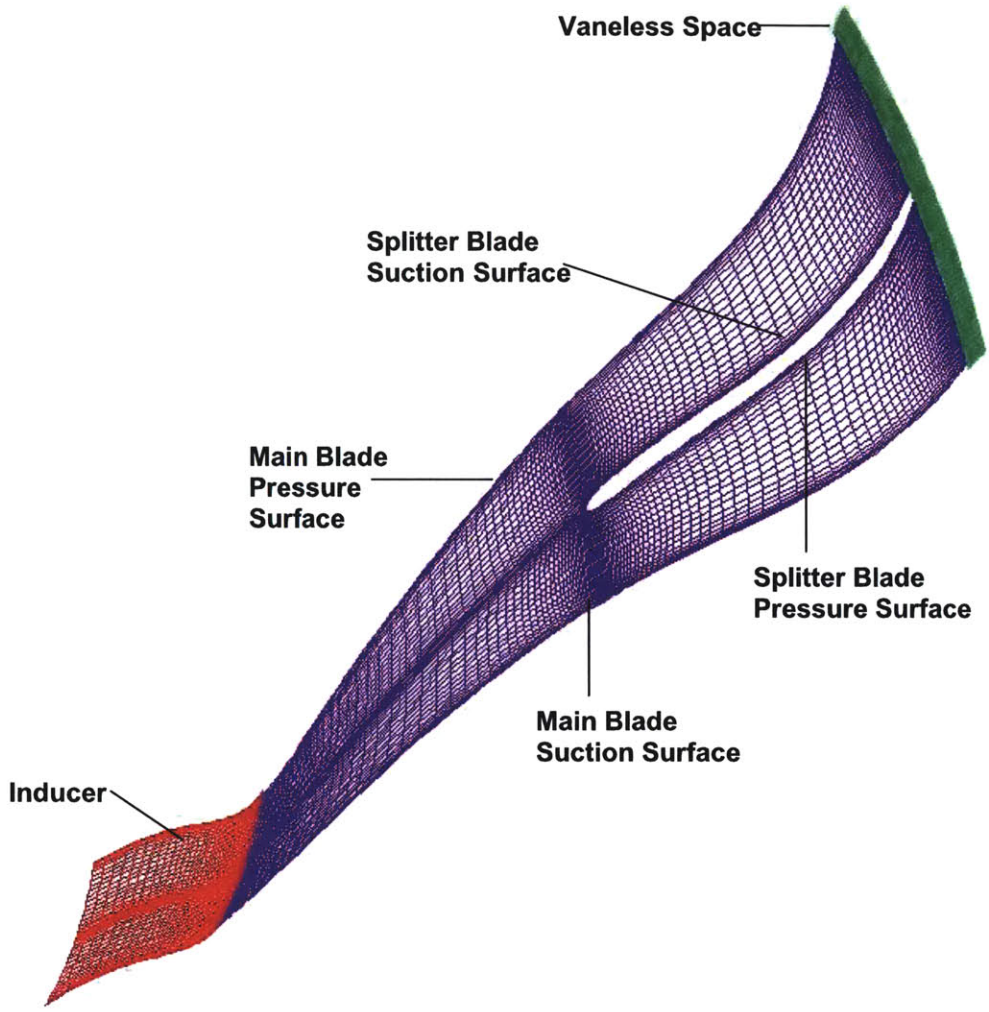

Figure 2.2 – Blocks 1 – 4 of the TURBO computational grids, where block 1 corresponds to the inducer region, blocks 2 and 3 together form one impeller passage, and block 4 corresponds to the first 45% of the vaneless space.

Block 5 is stationary and models the remainder of the vaneless space, one diffuser passage, and some distance downstream of the diffuser vane trailing edge. The numbers of nodes in each direction for the two geometries are tabulated in Table 2.1.

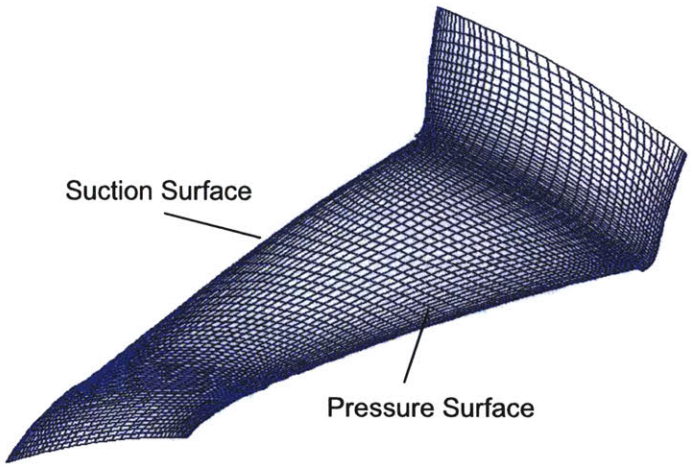

Figure 2.3 - Block 5 of the TURBO computational grids, which includes the last 55% of the vaneless space, one diffuser passage, and some distance downstream of the diffuser vane trailing edge.

	Production			Enhanced		
Block	i	j	k	i	j	k
1	37	51	53	37	51	53
2	134	51	27	134	51	27
3	134	51	27	134	51	27
4	20	51	53	20	51	53
5	103	51	41	97	51	41

Table 2.1- Number of nodes in the flow direction (i), spanwise direction (j) and pitchwise direction (k) in the TURBO computational grids for the production and enhanced compressors.

The ADPAC simulations were all performed by Mahmoud Mansour at Honeywell ES&S. However, the results from these simulations were used for comparing against those from simulations using the MSU Turbo, and so the grids are described briefly below. The computational domain used for the ADPAC simulations for each geometry consists of four blocks. Because ADPAC does not offer phase-lag boundary conditions, the blade counts were modified from 17-17-25 to 16-16-24, creating a periodic sector of two impeller passages and three diffuser passages (see Figure 2.4). The creation of a periodic sector made possible to model one periodic sector rather than the entire wheel.

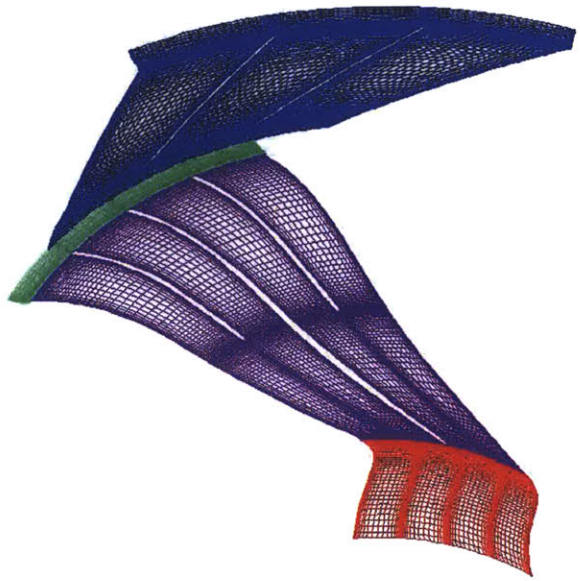

Figure 2.4 - ADPAC computational grids showing one periodic sector of two impeller passages and three diffuser passages.

2.2.1.3 Visualization

The software used for flow visualization and calculation of various parameters was FIELDVIEW®. TURBO outputs a solution file and a grid file for each block (these may be merged if desired) in PLOT3D format. The grid files contain information on the (x, y, z) co-ordinate system and the corresponding (i, j, k) node indexing system. The solution file contains five non-dimensionalized flow parameters: density (q1), x-momentum (q2), y-momentum (q3), z-momentum (q4), and stagnation energy (q5). Once the grid and solution files have been imported into FIELDVIEW®, FIELDVIEW® calculates such flow variables as static pressure and temperature, stagnation pressure and stagnation temperature, and the x, y, and z velocity. FIELDVIEW®'s function specification panel allows for calculation of parameters not automatically calculated by FIELDVIEW®, such as the velocity components in the cylindrical co-ordinate system. The integration control panel makes it possible to calculate area-averaged values of flow variables, and, indirectly, momentum-averaged and mass-averaged values of flow variables. The graphics window allows for 3-D visualization of the grid geometry and of the contours of a given parameter across a given surface.

2.2.2 ANSYS® - Structural Analysis

ANSYS® is a commercially available finite element analysis (FEA) code that can be used for a variety of applications. For each set of CFD results, the computed unsteady pressure distributions were used as the excitation source for the structural analysis performed using ANSYS®, using the method developed by Mansour and Kruse [25]. Damping levels had been previously approximated for the production and enhanced compressors as described in [25]. These levels were approximated using the half-power technique[1] on available strain gauge data for each geometry, and these estimates were then used in the structural analysis. The structural analyses using the MSU Turbo computed pressure distributions as excitations were performed by Josef Panovsky at Honeywell ES&S.

2.3 Code Validation

To validate TURBO both as a stand-alone CFD code for this application, and as part of the CFD/ FEA system, three different comparisons were performed. The first set of comparisons compares the normalized impeller work and the normalized impeller inlet corrected flow estimated using TURBO with those estimated using ADPAC and with measured test rig data. The second set of comparisons compares the maximum strain estimated using the TURBO/ ANSYS® system with the maximum strain estimated using ADPAC/ ANSYS® as well as with available test rig data. Lastly, the time-averaged change in performance between the production and enhanced compressors are compared with the trends documented in previous works.

[1] The half-power technique (also known as the half-power bandwidth method and the 3dB method) is a technique used to estimate damping for the single degree of freedom systems of viscoelastic materials. In this technique, the structural damping factor is estimated by finding the difference in the two frequencies on either side of resonance where the amplitude is $1/\sqrt{2}$ times the resonant amplitude, then dividing the difference by the resonant frequency [29].

2.3.1 Available Test Rig Data and Limitations

Both the aerodynamic and structural testing were performed several years before this project was initiated, thus there are limitations on the data availability. The only remaining aerodynamic test data available from the flow fields in the two geometries are:

- Mass flow and work at 102% corrected speed for the production stage
- Mass flow and work at 95% corrected speed for the enhanced stage
- Mass flow and work at 97.5% corrected speed for the enhanced stage

From the documentation available on the strain gauge tests, the splitter blades were instrumented with strain gauges as shown in Figure 2.5 and Figure 2.6. Strain gauge factors were estimated using the mode shape of concern for each geometry (the 4th mode for the production and the 5th mode for the enhanced). The maximum strains measured were then divided by the strain gauge factors to determine the maximum strain on the splitter blade. The maximum strains were recorded at the following corrected speeds:

- Production – 102% speed
- Enhanced – 96.2% speed

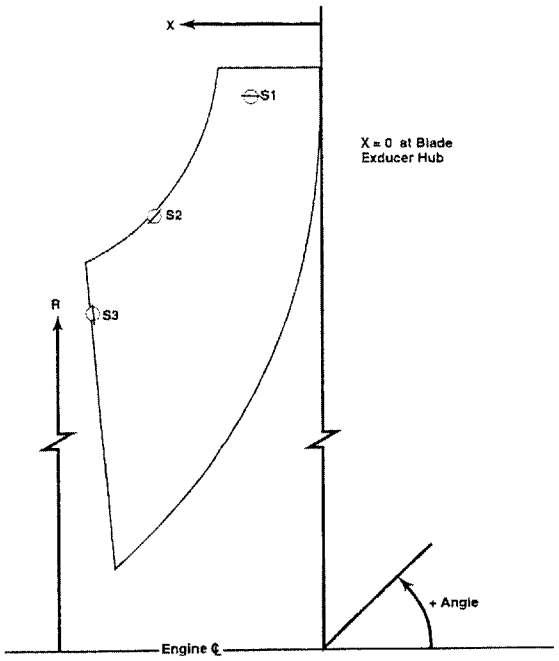

Figure 2.5 - Production compressor splitter blade suction surface strain gauge instrumentation, where s1, s2, and s3 correspond to strain gauge locations.

Only peak-hold data was available for this analysis. Fortunately, the damping previously calculated by Marlin Kruse [25] using the half-power technique is still available, and therefore more detailed data is not necessary. Unfortunately, an insufficient number of blades were instrumented to capture the required to account for blade-to-blade variations. However, overall trends and approximate values are still valuable for assessing the trends observed in the computational results.

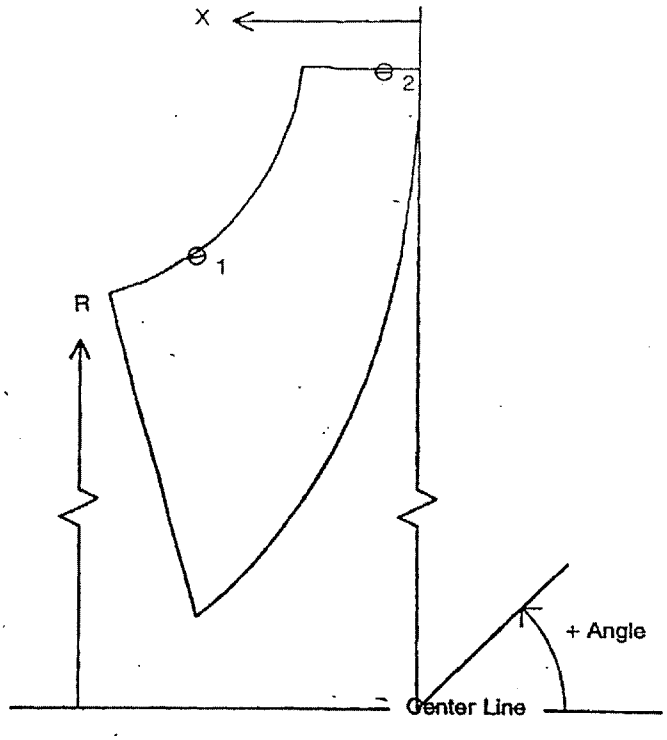

Figure 2.6 - Enhanced compressor splitter blade strain gauge instrumentation, where 1 and 2 are strain gauge locations

2.3.2 CFD Calculations for Code Assessment

For comparing the results from the TURBO calculations with the ADPAC results and the test data, the TURBO calculations were performed with inlet conditions, reference values, and back pressures corresponding to those used in the ADPAC calculations. As in the ADPAC calculations, the TURBO calculations were run at the following corrected speeds:

- Production stage – 102% speed
- Enhanced stage – 96.2% speed

In addition, TURBO calculations were run at the following corrected speed:

- Production stage – 96.2%

The corrected speeds using in both the ADPAC and TURBO analyses were initially chosen because they are the speeds at which the maximum strains occurred during testing of the production stage, and at which the HCF problems were encountered in the enhanced stage. Simulations for the production compressor were then performed at 96.2% so that a direct comparison of the time-averaged performance with the enhanced time-averaged performance could be made.

As stated at the beginning of Section 2.3, the first set of comparisons compares TURBO normalized impeller work and normalized impeller inlet corrected flow predictions with ADPAC predictions and with measured test rig data by plotting all estimates and measurements on the same compressor map. For the production case, the 102% data was recorded during testing, so the CFD estimates may be compared one-to-one with the aerodynamic data. For the enhanced case, the 96.2% speedline should lie between the 95% and 97.5% speedlines on the measured performance map; as there is no test data at the 96.2% corrected speed, a direct comparison between the computational data and the test data is not possible. In contrast, the TURBO and ADPAC calculations were performed at the same corrected speeds so that a direct comparison may be made between the TURBO estimate and the ADPAC estimate. These results will be presented in Section 3.2.1.

The second set of comparisons compares the TURBO/ ANSYS® maximum strain estimates with the maximum strains estimated using the ADPAC/ ANSYS® system and with the available test rig data (Section 3.2.2). All corrected speeds for a given geometry are the same (102% for production and 96.2% for enhanced) for the computational estimates and the strain gauge measurements, so comparisons can be made directly.

Lastly, the time-averaged performance of the production and enhanced compressors are compared at the same corrected speed and mass flow. Because mass flow rate is not a TURBO input, but rather a parameter that must be calculated from the TURBO outputs, iterations were required to find a point at which the mass flow rates in the two compressors are comparable. This mass flow rate was determined by obtaining converged solutions at the 96.2% corrected speed, then slowly increasing the back-pressure for each compressor, obtaining converged solutions at each back pressure, thus forming a 96.2% speedline for each compressor.

2.4 Flow Field Comparison

To determine the root cause of the vibrations leading to HCF problems, the flow fields of the production and enhanced compressors are compared. In order to compare the flow fields of the two different geometries, TURBO runs were performed at the same corrected speed (96.2%) and at the same corrected mass flow for the two geometries. In addition to the FIELDVIEW® visualization methods described in 2.2.1.3, FORTRAN and Matlab codes were used to view the static pressure (Ps), total Pressure (Pt), and entropy generation (Δs) distributions across the entire annulus at various points within the vaneless space, at several time steps within one period. Matlab was then used to obtain the static pressure power spectrum in the circumferential direction at a given instant in time, in order to determine the differences between the harmonic content of the production compressor and that of the enhanced compressor. The operation point analyzed is the same as that used for the third method of CFD code assessment described in Section 2.3.2, as well as at a point closer to stall.

2.5 Averaging of Flow Variables

As the TURBO simulation results are unsteady and the flow in the impeller-diffuser interaction region is highly non-uniform, averaging techniques were used to define variables at the impeller exit, across the vaneless space and at the diffuser inlet. The flow parameters used in the code assessment and in the flow field comparison, and the averaging techniques used upon each variable are described below.

The unsteady pressure loading (ΔPs) was calculated, including the maximum encountered during a period, the minimum encountered over a period, and time-averaged values. The pressure loading was non-dimensionalized in the following manner:

$$\Delta Ps = \frac{Pps - Pss}{\frac{1}{2}\rho_{in} u_{tip}^{\ 2}}$$

where Pps is the static pressure on the pressure surface of the blade, and Pss is the static pressure on the suction surface of the blade. The blade loading was determined at each time instant, and then the maximum, minimum, and time-averaged values were calculated.

The mass-averaged entropy generation was calculated, and then time averaged. The mass-averaged value was obtained using:

$$\Delta\hat{s} = \frac{\int \rho\vec{V} \bullet \hat{n} s dA - \int_{impeller\_inlet} \rho\vec{V} \bullet \hat{n} s dA}{\int \rho\vec{V} \bullet \hat{n} dA}$$

where $\hat{n}$ is the unit vector normal to the inlet or exit plane. The time-averaged value is then obtained using:

$$\Delta\bar{s} = \frac{\sum_{N} \Delta\hat{s}}{N}$$

where N is the number of time steps recorded over one period and $\Delta\hat{s}$ is calculated in equation 1. In addition, energy loss was calculated as:

$$\Delta E = \frac{T\Delta\hat{s}}{\frac{1}{2}u_{tip}^{\ 2}}$$

Time-averaged swirl angle was defined using the time-averaged velocities:

$$\dot{\alpha} = \tan^{-1}\left(\frac{\dot{v}_\theta}{\dot{v}_r}\right)$$

in which

$$\dot{v}_r = \frac{\sum_N v_r}{N} \text{ and } \dot{v}_\theta = \frac{\sum_N v_\theta}{N}.$$

Because only the Cartesian velocity components were readily available from TURBO outputs, the velocities at the diffuser inlet, in which the x-coordinate remains constant were calculated as:

$$v_r = \frac{(zw + yv)}{\sqrt{(z^2 + y^2)}}$$

$$v_\theta = \frac{(zv - yw)}{\sqrt{(y^2 + z^2)}}$$

In addition, the momentum- and time-averaged inlet swirl was defined based upon the momentum-averaged, time-averaged velocities as:

$$\overline{\alpha} = \tan^{-1}\left(\frac{\overline{v}_\theta}{\overline{v}_r}\right)$$

where the momentum-averaged velocities are defined as:

$$\hat{v}_r = \frac{\int \rho v_r \vec{V} \bullet \hat{n} dA}{\int \rho \vec{V} \bullet \hat{n} dA} \qquad \hat{v}_\theta = \frac{\int \rho v_\theta \vec{V} \bullet \hat{n} dA}{\int \rho \vec{V} \bullet \hat{n} dA}$$

and the momentum- time-averaged velocities are defines as:

$$\overline{v}_r = \frac{\sum_N \hat{v}_r}{N} \qquad \overline{v}_\theta = \frac{\sum_N \hat{v}_\theta}{N}$$

The diffuser pressure recovery (Cp) was calculated based upon area-averaged, time-averaged diffuser inlet and exit static pressure values and the momentum and time-averaged diffuser inlet total pressure:

$$Cp = \frac{Ps_{exit} - Ps_{inlet}}{\overline{Pt}_{inlet} - Ps_{inlet}}$$

and

$$\overline{Pt} = \frac{\sum_{N} \frac{\int \rho Pt \vec{V} \bullet \hat{n} dA}{\int \rho \vec{V} \bullet \hat{n} dA}}{N}$$

Finally, the average mass flow across the inlet and exit planes were calculated as:

$$\dot{m} = \frac{\sum_{N} \int \rho \vec{V} \bullet \hat{n} dA}{N}.$$

2.6 Chapter 2 Summary

This chapter first described the research articles and the computational tools used in the investigation into HCF. The production centrifugal compressor stage and its redesign, the enhanced compressor stage, were described; the most significant difference between the two geometries is that the impeller tip radius was increased in the enhanced design, leading to a smaller vaneless space. The CFD code MSU Turbo was described; the advantage of TURBO over ADPAC is that is does offer phase-lab boundary conditions, eliminating the need to modify blade counts. A predictive system using CFD and structural dynamics analysis codes for forced response analyses was then described briefly.

The second half of this chapter focused on the methodology used to assess the computational tools and to compare the unsteady flow fields of the production and

enhanced compressor designs. Three types of assessments for the computational tools were enumerated:

- Comparison of the normalized impeller work and the normalized impeller inlet corrected flow estimates using TURBO with ADPAC estimates and with measured test rig data;
- Comparison of the maximum strain estimated using the TURBO/ ANSYS® system with the maximum strain estimated using the ADPAC/ ANSYS® system as well as with available test rig data;
- Comparison of time-averaged change in performance between the production and enhanced compressors with the trends documented in previous publications.

Lastly, the methods used for the unsteady flow field comparison are described, and the expressions used to determine the time-averaged, area-averaged, and momentum-averaged flow variables and performance metrics are delineated.

Chapter 3

Assessment of Computational Tools

3.1 Introduction

Computational methods consisting of CFD and structural dynamics analysis codes can be useful tools for interrogating the aerodynamic and structural behavior of centrifugal compressor stages where experimental measurements are difficult, if not impossible, to acquire; however, it is necessary to anchor computational results to experimental data in order to insure that the computational tools are yielding the correct physical trends. In this chapter, time-averaged CFD results are presented in an evaluation of the MSU Turbo code (TURBO) and the CFD/ ANSYS® system as tools for analyzing flow in two similar high-speed centrifugal compressor stages (the production and enhanced compressor designs, a schematic view of which is shown in Figure 3.1) and for estimating the vibratory response of the impeller blades to the unsteady pressure field in each compressor.

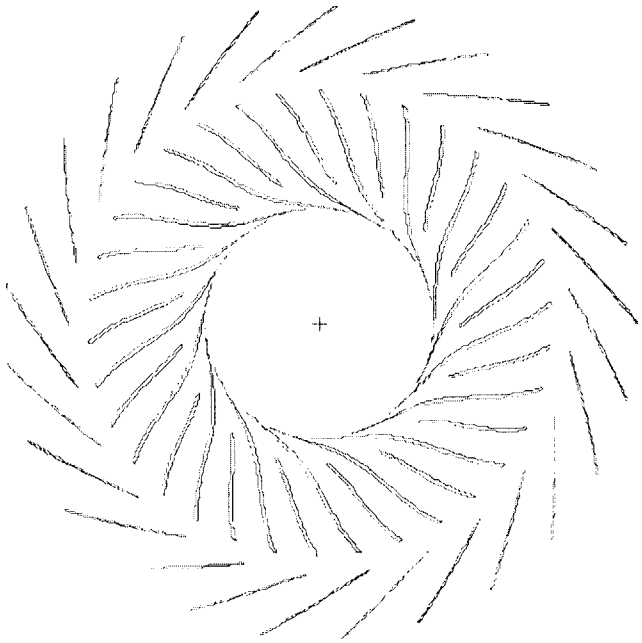

Figure 3.1 – Axial schematic view of the production/enhanced compressor.

This assessment consists of two types of comparisons. The first type of assessment entails comparing computed results from CFD and the CFD/ ANSYS® system with aerodynamic test rig data and with strain gauge data taken on the test rig. The second type of evaluation involves comparing the computed trends of the change in time-averaged flow parameters and performance metrics with variations in impeller-diffuser gap size to the trends reported by Phillips [17], Shum [18], Shum, Tan and Cumpsty [19], Murray [22] and Murray and Tan [23], as well as with test rig data.

In the ensuing sections, results are presented to show the potential of MSU Turbo and the CFD/ ANSYS® system as tools for calculating flow and for estimating strain due to impeller-diffuser interaction in centrifugal compressors. Estimated work characteristics and strain estimates based on MSU Turbo results agree with the trends shown in both test rig data and with estimates based on ADPAC results. In addition, the computed results from MSU Turbo show that the time-averaged performance of the production compressor was improved by growing the impeller tip radius (and thus decreasing the vaneless space) of the production compressor, to arrive at the enhanced compressor.

3.2 Assessing the Adequacy of Computational Tools

This section focuses on the assessment of the MSU Turbo code and of the CFD/ ANSYS® system for calculating the unsteady flow fields in centrifugal compressors of nearly identical design and for estimating the vibratory responses of impeller blades. To assess the adequacy of MSU Turbo for simulating the flow in both the production and the enhanced compressor stage designs, time-averaged flow results from both MSU Turbo and ADPAC are compared with each other and with available aerodynamic test rig data. In addition, the vibratory response estimations using MSU Turbo in conjunction with ANSYS® and from ADPAC in conjunction with ANSYS® are compared with strain gauge data for each compressor design. For both sets of comparisons, the production stage was run at 102% speed and the enhanced stage was run at 96.2% speed, the speeds at which the maximum strains were encountered during testing, as described in section 2.3.2.

Two CFD codes were used in these analyses. Some of the ANSYS-based results have previously been reported by Mansour and Kruse [25], showing that the CFD/ ANSYS® system has promise as a tool for estimating the forced response of impeller blades. The ADPAC simulations were performed with modified impeller and diffuser blade counts (see section 2.2.1.2) for both the production and the enhanced designs. The use of phase-lag boundary conditions in MSU Turbo (an option not available in ADPAC) yields a flow field corresponding to the actual blade counts. Thus, for the purpose of interrogation into the unsteady flow fields and for forced response estimation, the use of MSU Turbo constitutes an improvement over the use of ADPAC.

3.2.1 Assessment of CFD Codes

In order to assess the utility of MSU Turbo for capturing differences in the flow fields of two similar centrifugal compressor stages, CFD has been performed on two similar compressor stages (the production and enhanced designs). To perform this assessment, first the time-averaged work characteristics based on the TURBO data is compared to the work characteristics based on aerodynamic test rig measurements and to the single data point for each compressor based on ADPAC results (full work characteristic estimates are not available from ADPAC for each compressor design, as only one operating point for each design was simulated in ADPAC). The unsteady pressures along the impeller main and splitter blades based on TURBO results and on ADPAC results are then compared to each other, and the trends defined by each are noted.

3.2.1.1 Comparison of CFD Results With Aerodynamic Test Rig Data

The aerodynamic test data available for comparison with CFD simulation results consists of several operating points along the 102% speedline for the production compressor and along the 95% and 97.5% speedlines for the enhanced compressor. Work characteristics (speedlines) for the production and enhanced compressor stages are shown in Figure 3.2,

where the abscissa is the time-averaged, normalized impeller inlet corrected flow and the vertical coordinate is normalized work.

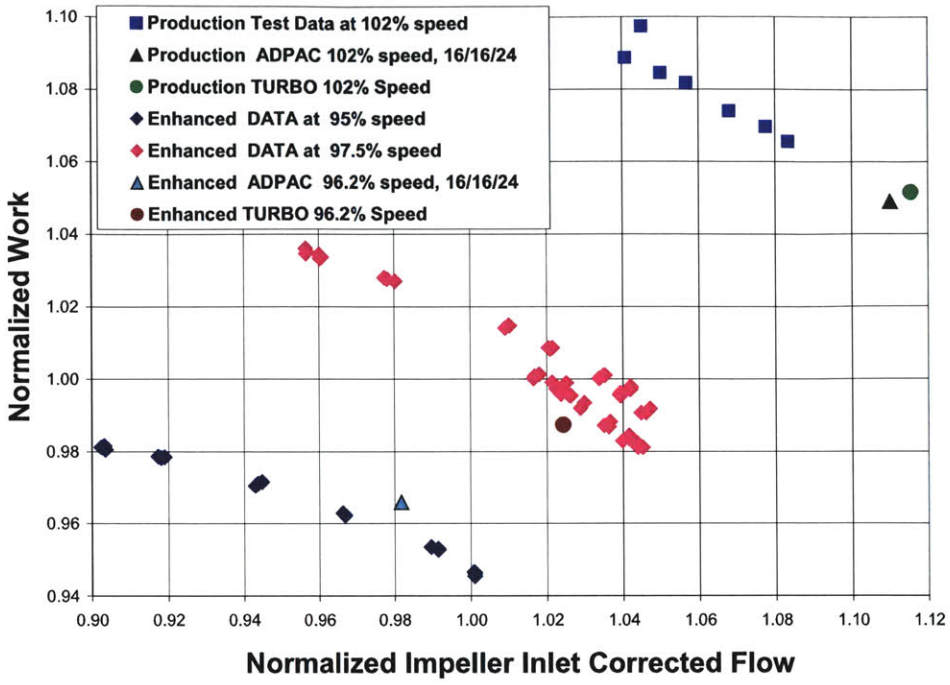

Figure 3.2 - Work characteristics for aerodynamic test data, ADPAC simulations and MSU Turbo simulations

Here, work is defined as the change in total temperature divided by the inlet total temperature. In addition, the total pressure ratio across the production and enhanced compressor stages are shown in Figure 3.3. Because information regarding the exact flow conditions for each point along the test data speedlines is not available, quantitative comparisons between the test data and the CFD simulations cannot be performed. Furthermore, the effects due to the deswirler vanes that are captured in the experimental measurements are not represented nor reflected in the CFD calculations. Because the main role of the CFD simulations in this project is to enable comparisons of the unsteady flow fields of the two compressors of similar design, a comparison in the quantitative trends for the production and enhanced compressors may be deemed adequate for code assessment and validation. Therefore, this assessment compares the trends captured by the CFD simulations and those measured during testing. The CFD tool would be deemed adequate if the computed 102% speedline and the 102% speedline from test data for the production stage are in accord. Likewise, if the computed 96.2% work characteristic for the enhanced stage is determined to lie between the test data 95% and

97.5% work characteristics, then it would be argued that the CFD tool is adequate for the objectives delineated in Section 1.3.

From Figure 3.2, it may be inferred that the MSU Turbo results for the production and enhanced compressors are physically consistent based on comparisons of TURBO-calculated impeller work and corrected mass flow estimates with ADPAC estimates and with test measurements. From Figure 3.2, it is apparent that the production simulation runs at a higher corrected flow than the test data, and the normalized work is slightly higher than would be expected based on the trend shown by the test data speedline. Though a quantitative comparison is not possible between computed data and test data, a quantitative comparison can be made against the ADPAC data, which was obtained at the same backpressure as the TURBO data. As presented in [25], the ADPAC simulation also yielded a higher corrected flow than the test data, though the calculated corrected work follows the trend of the test data speedline. The corrected mass flow and the work calculated from MSU Turbo simulations are 0.5% and 0.2% higher, respectively, than those calculated using the ADPAC results. Because a 96.2% test data speedline is not available for the enhanced geometry, all that can be said for the MSU Turbo simulation in comparison with test data is that corrected flow and work fall within the range bounded by the 95% and the 97.5% speedlines. The corrected flow calculated by MSU Turbo is 4% higher than that calculated by ADPAC, and the work is 2% higher than that calculated by ADPAC. As a result, the MSU Turbo simulation places the 96.2% speedline closer to the 97.5% speedline, while the ADPAC 96.2% data lies close to the 95% speedline.

It may be noted that the MSU Turbo- computed corrected flow is consistently higher than that computed using ADPAC, even though the backpressure and the corrected speed are the same for the two CFD codes for a given compressor design (production or enhanced). This discrepancy may be partially attributed to the fact that the blade count in the MSU Turbo simulation is the actual 17/17/25 count, rather than the 16/16/24 count of the ADPAC simulation. The decrease in the number of the impeller main and splitter blades would increase the blade loading on the impeller blades. Higher blade loading can result

in viscous layer growth and flow separation, which would increase blockage. This increase in blockage would, in turn, decrease the effective flow area, and hence the difference between the ADPAC- and TURBO- computed mass flows.

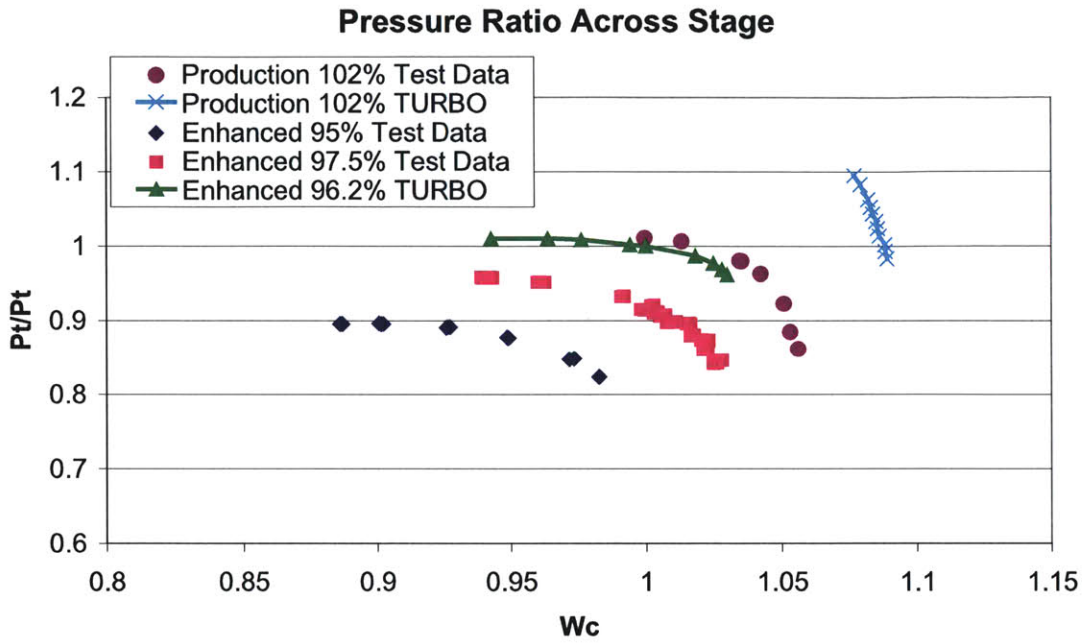

Figure 3.3 - Pressure ratio across the production and enhanced compressor stages. Test measurements are at operating points along the 102% speedlines for the production compressor and 95% and 97.5% speedlines for the enhanced compressor. TURBO simulation results are at operating points along the 102% speedline for the production compressor and along the 96.2% speedline of the enhanced compressor.

Shown in Figure 3.3 are: (i) The computed and measured total pressure vs. mass flow characteristics at 102% speed of the production stage; (ii) the computed total pressure ratio vs. mass flow characteristics at 96.2% speed and the measured characteristics at 95% speed and 97.5% speed for the enhanced stage. The enhanced 96.2% TURBO-generated speedline lies above both the 95% and the 97.5% lines from test measurements, where it was expected to lie between the two speedlines; the production 102% TURBO-generated operating line lies above the corresponding test measurements. For the production results, the highest mass flow estimated by TURBO is approximately 3% higher than the highest mass flow measured during testing, while the highest total pressure ratio estimated by TURBO is 8% higher than the highest total pressure ratio measured during testing. A similar comparison cannot be performed for on the enhanced

compressor design because a 96.2% speedline from test measurements is not available; however, the fact that the total pressure ratios for the TURBO-generated speedline are 8% to 14% higher than those measured for the enhanced 97.5% test data clearly indicates that the TURBO total pressure ratio estimates are higher than what would have been found during testing at 96.2% speed. The fact that the TURBO simulations produce consistently higher results than the test measurements can be attributed to the fact that the TURBO data does not include the effects of the deswirler vanes at the diffuser exit, the effects of which are reflected in the test data. Despite these differences in pressure ratio, Figure 3.3 shows that there are no significant differences in the trends of the TURBO-generated speedlines with those obtained from test measurements. The observations that the trends generated by TURBO are similar to the actual trends found in test measurements, and that the pressure ratios are consistently higher for the TURBO measurements for both the production and the enhanced compressor indicate that the MSU Turbo CFD code is an adequate tool for comparing the flow fields of the two compressors of nearly identical designs (see further assessments below).

3.2.1.2 Comparison of Two Codes – Unsteady Pressures

The computed static pressure distributions across the impeller main and splitter blades, shown in Figures 3.4 and 3.5, indicate that though there are differences in the flow fields computed using the two different CFD codes, both codes produce similar trends. These two figures are plots of normalized static pressure (local static pressure minus the inlet static pressure, normalized by the dynamic pressure head based on the density at the impeller inlet and the impeller tip speed) along the blade surfaces for both the impeller main blade (Figure 3.4) and the impeller splitter blade (Figure 3.5). Both figures are arranged such that the left column contains the production 102% ADPAC and TURBO results from near the hub (10% span) to near the tip (90% span), and the right column contains the enhanced 96.2% ADPAC and TURBO results from near the hub (10% span) to near the tip (90% span).

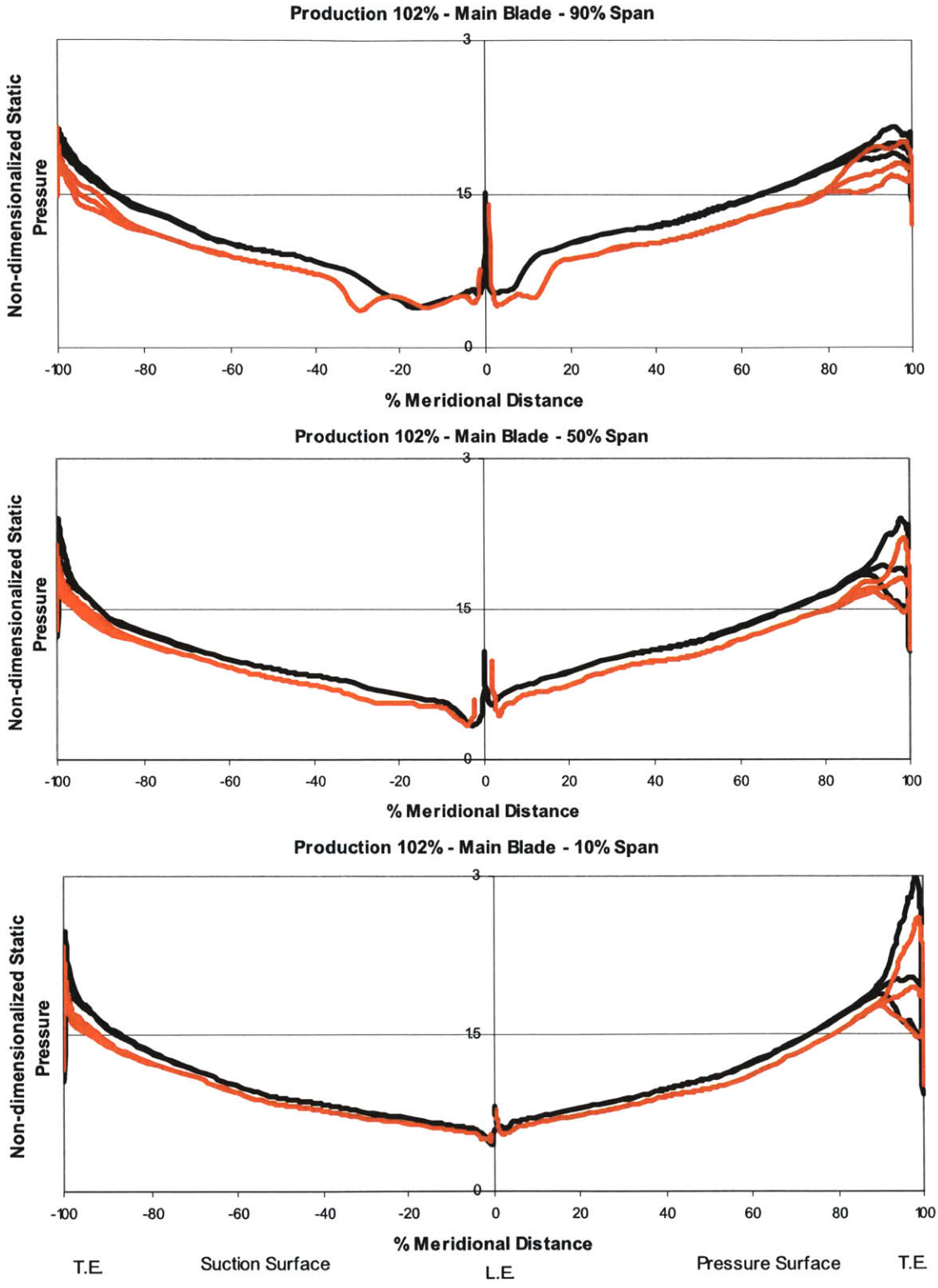

Figure 3.4a - Unsteady static pressures on the main blade surfaces for the production compressor at 102% corrected speed.

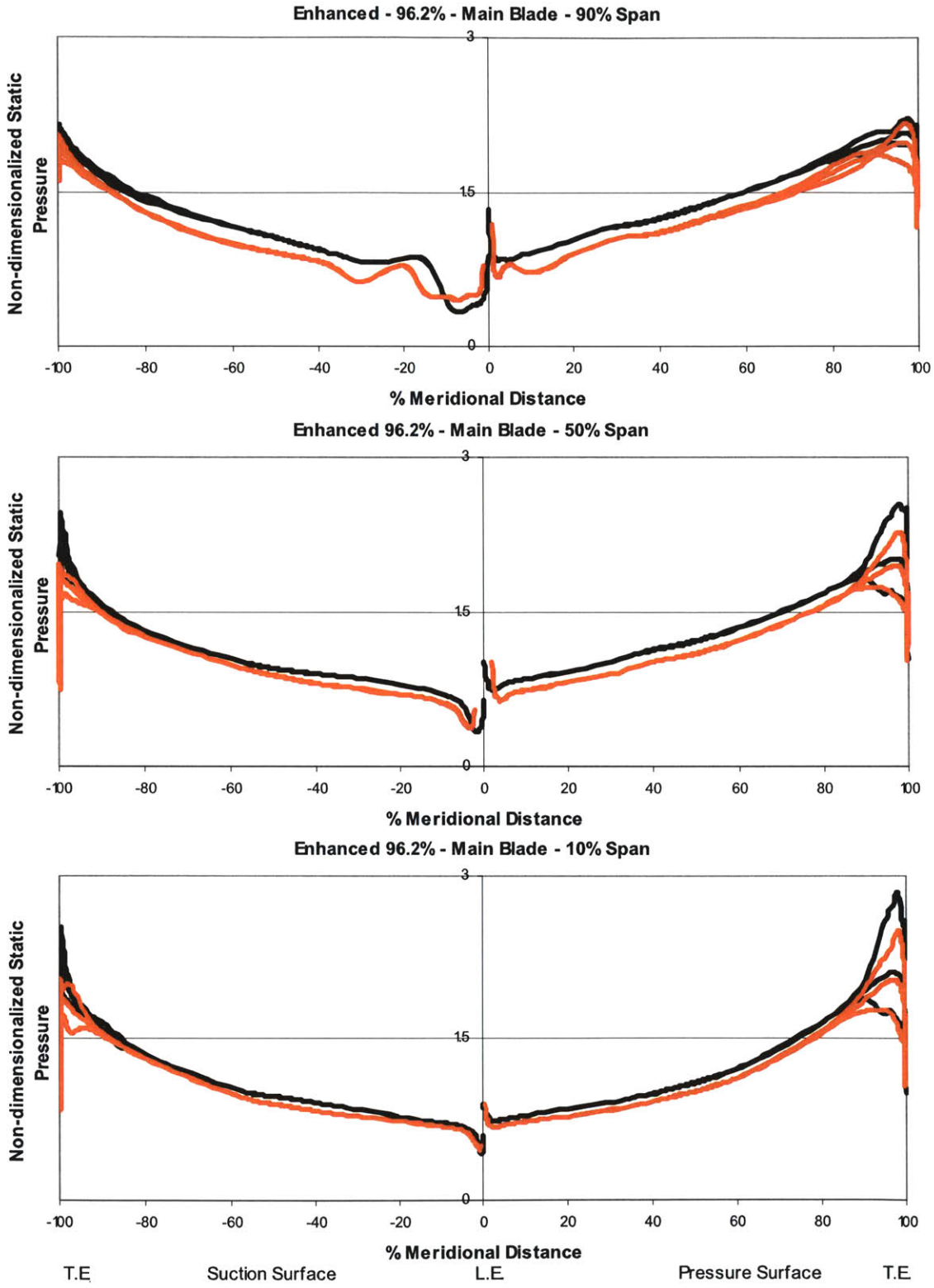

Figure 3.4b - Unsteady static pressures on the main blade surfaces of the enhanced compressor at 96.2% corrected speed.

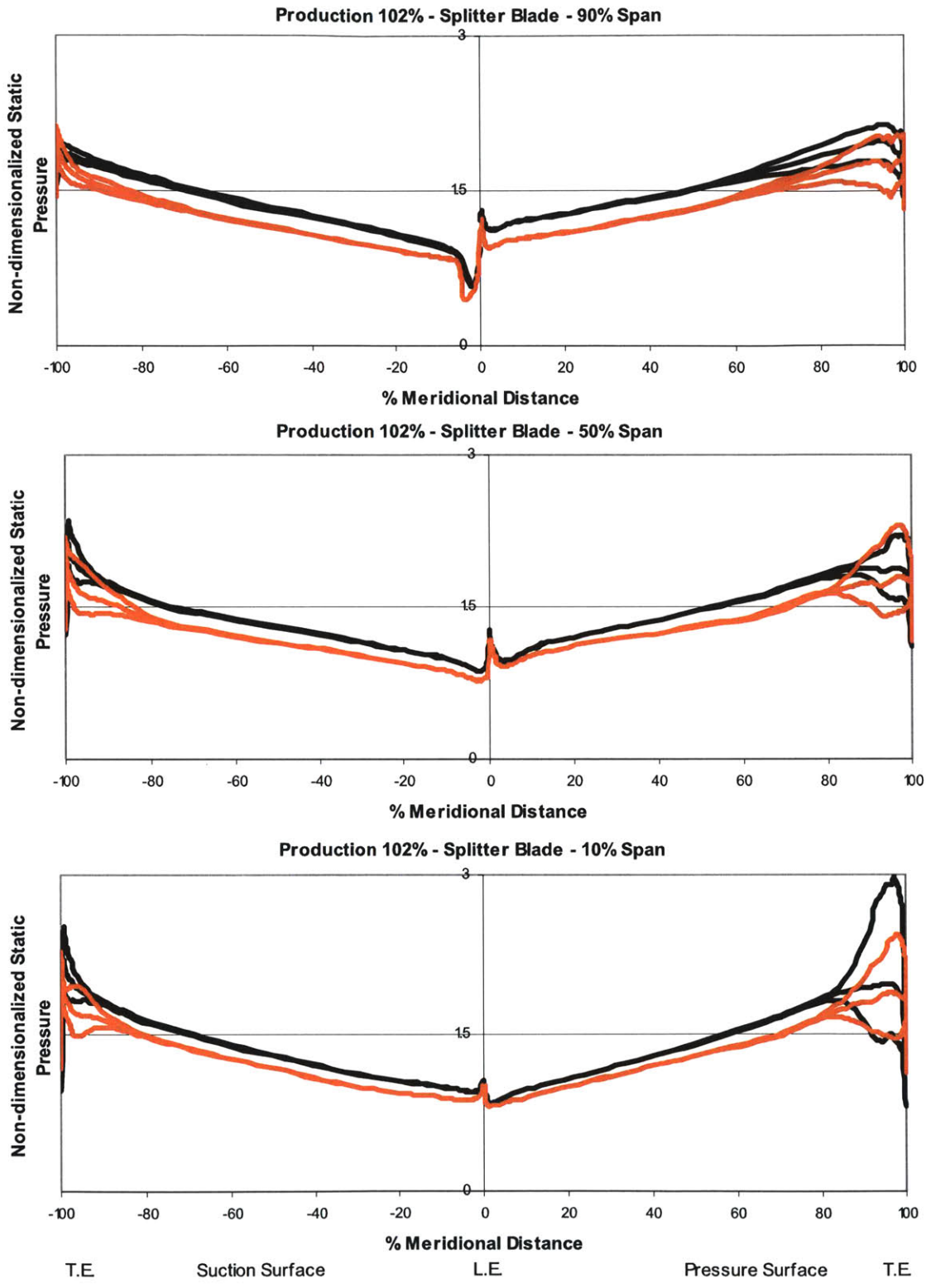

Figure 3.5a - Unsteady static pressures on the splitter blade surfaces of the production compressor at 102% corrected speed.

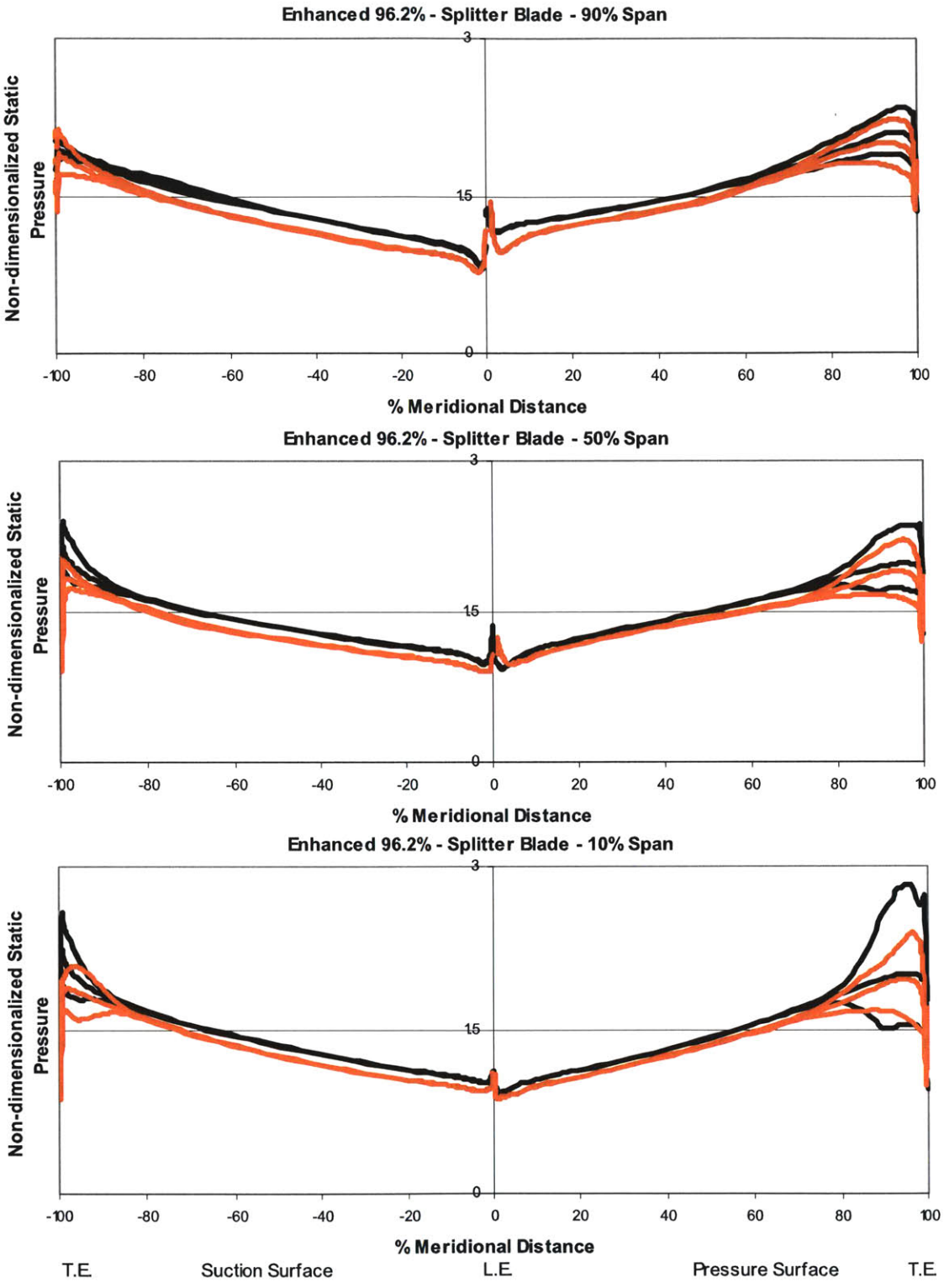

Figure 3.5b - Unsteady static pressures on the splitter blade surfaces of the enhanced compressor at 96.2% corrected speed.

The negative portion of the horizontal axis for all figures corresponds to the suction surface of the blade and the positive portion of the horizontal axis corresponds to the pressure surface, with the leading edge of the blade at 0, and the trailing edge at 100 and −100. The black lines correspond to the ADPAC predictions, and the orange lines correspond to the MSU Turbo predictions. For a given plot, on a given surface, the top black line is the maximum pressure encountered over one period in ADPAC, the middle line is the time-averaged pressure in ADPAC, and the bottom black line is the minimum pressure encountered over a period in ADPAC. The same pattern is found in the orange lines for the MSU Turbo results. The maximum, average, and minimum pressures presented here are the result of taking unsteady pressure results at 20 equally spaced time instants within one period, and finding the maximum, average, and minimum values at each point.

Though there are differences in the ADPAC and MSU Turbo results, there are trends that are similar for the unsteady pressures on the blade surfaces for both sets of CFD results: the unsteadiness (the envelope formed by the maximum and minimum pressure over time) increases from tip to hub, occurs mainly on the pressure surface of each blade, and is confined to the last 10-15% meridional distance of each blade. The one feature that is common to the main and splitter blades in both production and enhanced designs, for both sets of CFD results, is that the unsteadiness is largest at the hub, and decreases along the span towards the tip. Furthermore, it is noted that the unsteadiness is always greater on the pressure surface than on the suction surface; however, the amount of unsteadiness on the suction surface appears to vary with each CFD code (i.e. MSU Turbo, with a 17/17/25 blade count, and ADPAC, with a 16/16/24 blade count) and blade type (main or splitter). On the main blade surfaces, the ADPAC calculations indicate that the unsteadiness is confined almost solely to the pressure surface of the blade, while the TURBO results indicate that although the unsteadiness is confined mainly to the pressure surface as indicated by the ADPAC calculations, there is also appreciable unsteadiness on the suction surface of the main blade. On the splitter blade surfaces, it can be inferred from both the ADPAC and TURBO calculations that though the unsteadiness occurs mostly on the pressure surface of each blade, there is appreciable unsteadiness on the

suction surface as well. The last feature that is common to the static pressure distribution on all blade surfaces is that the peak unsteadiness (maximum difference between the maximum and minimum pressures) occurs within the last 10-15% of each blade for all blades for both CFD codes. This result is in accord with the findings of Shum [18] and Shum, Tan and Cumpsty [19]. Near the hub and at mid-span, the unsteadiness has been completely attenuated within 20% of the trailing edge on the main blade, and within 20-25% of the trailing edge of the splitter blade. Near the tip, the unsteadiness extends further upstream into the impeller passage. This increase in the extent of the unsteadiness may possibly be due to tip clearance effects.

As mentioned in the previous paragraph, there are notable differences between the ADPAC and the MSU Turbo results, which could lead to differences in forced response estimates. One difference between the ADPAC and the MSU Turbo results is that the ADPAC-computed static pressure is always higher than the Turbo-computed pressure from the leading edge of each blade until approximately 20% upstream of the impeller blade trailing edge plane, with the exception of the tip region of the production and enhanced main blades. In spite of this difference, the pattern of pressure variation with meridional distance in the first 80% of the blades are similar for the results of the two flow codes, with the one exception noted above. Therefore, the estimation of the steady flow behavior by the two CFD codes is similar. By contrast, the unsteady behavior of the static pressure flow field, as shown in Figure 3.4 and Figure 3.5 differs between the ADPAC and the MSU Turbo- computed results. This difference in the unsteady flow field pattern predictions could lead to a difference in the prediction of the unsteady loading patterns on the blade surfaces, affecting vibratory strain estimates.

3.2.2 Assessment of CFD/ ANSYS® System

As discussed in Chapter 2, only limited strain gauge data was available for comparison with CFD/ ANSYS® estimates. The results from strain gauge testing are tabulated in Table 3.1. Again, it can be noted that the highest strain encountered for each compressor occurred on the splitter blade at the 25th engine order (excitation order), but that the

maximum strain encountered by the production occurred at the fourth vibration mode and was only half that of the enhanced, which occurred at the fifth vibration mode.

	Normalized Peak Strain	Peak Strain Location	Mode	Excitation Order
Production	100	Splitter Blade	4^{th}	25E
Enhanced	200	Splitter Blade	5^{th}	25E

Table 3.1 - Strain gauge test data.

Both the ADPAC/ ANSYS® and MSU Turbo/ ANSYS® systems predicted the correct vibration mode, excitation order, and peak strain location for the production and enhanced designs, but the peak values estimated by the CFD/ structural dynamics analysis system varies with the CFD code used in the analysis. Tabulated below (Table 3.2) is a comparison of the normalized peak strains estimated by MSU Turbo/ ANSYS® with both ADPAC/ ANSYS® estimates and with test rig data. The MSU Turbo/ ANSYS® analyses were implemented at the same corrected speeds and the same backpressures as the ADPAC/ ANSYS® analyses to allow for a comparison of the two CFD codes. These predictions are tabulated in the row labeled Production 102%, and in the first row labeled Enhanced 96.18%. As noted by Mansour and Kruse [25], the ADPAC/ ANSYS® system underestimates the peak strain for the production stage by nearly two-thirds, and that for the enhanced stage by approximately one-third. As a result, the ADPAC system has predicted that the vibratory response of the enhanced compressor is four times that of the production compressor, as opposed to the doubling of strains actually encountered during testing. By contrast, the MSU Turbo/ ANSYS® system estimate for the production compressor is within two percent of the experimental data, while the MSU Turbo/ ANSYS® system underestimates the experimental value of peak strain in the enhanced compressor by nearly 45%. Thus, the estimate based on the MSU Turbo/ ANSYS® system results indicate a 9% increase in strain from the

production to the enhanced compressor designs, far underestimating the 100% increase encountered during testing.

	Percent Speed	Normalized Maximum Strain (Test)	Normalized Maximum Strain (ADPAC)	Normalized Maximum Strain (TURBO)
Production	102%	100	30	102
Enhanced	96.2%	200	126	111
Enhanced	96.2%	200	N/A	128

Table 3.2 - Comparison of peak strain measurements and predictions

Several factors may contribute to the discrepancies between the measured and estimated peak strain values. Mansour and Kruse [25] enumerated three factors in order to account for the discrepancies between the ADPAC/ ANSYS® estimates and the test data: the effect of changing the blade counts on the characteristic shape of blade surface pressures, lack of information on blade-to-blade variations in the test data, and lack of knowledge of the precise operating point at which the strain measurements were made. Of these three factors, only two are relevant to the estimates based on the TURBO/ ANSYS® results; the first of these three factors is no longer applicable as the blade counts used in the MSU Turbo simulations match those of the experimental test articles. The lack of blade-to-blade variation information in the experimental data remains a problem for comparison with the MSU Turbo/ ANSYS® estimates; however, this alone cannot explain the large discrepancy between the enhanced peak strain measurement and the corresponding computational estimates. The effect of the remaining factor, the lack of knowledge of the exact operating point at which the strain measurements were obtained, on the agreement of the CFD/ ANSYS® strain estimate with test measurements requires further examination. The enhanced 96.18% entry in the final row of Table 3.2 is the result of examining an operating point at a higher backpressure (and therefore closer to stall than the initial operating point examined) for the enhanced compressor geometry. At this operating point, the MSU Turbo/ ANSYS® estimate has increased from just over one-half of the experimental value to two-thirds of the experimental value. Therefore, if

the test were performed at an operating point closer to stall than the initial CFD/ ANSYS® calculations, the CFD/ ANSYS® strain estimate would be expected to be lower than the measured peak strain value. While this uncertainty in the test data may not explain the discrepancy between the peak strain measurements and estimates for the enhanced compressor in its entirety [28], it could be a substantial contributor to this discrepancy.

In addition to the factors listed above, one last source of error should be considered. Because the strain estimates for the enhanced stage using both ADPAC and TURBO as the CFD portion of the CFD/ ANSYS® system are lower than the experimental data, it is possible that a systematic error may be found in the implementation of ANSYS® for the enhanced geometry. The most likely source of this error is in the aerodynamic damping estimate. While the damping factors for both the production and the enhanced stages were estimated using the half-power technique[2], it is possible that the estimate for the enhanced stage was inaccurate enough to cause discrepancies between the experimental measurements and the estimates based on the computational analyses.

The MSU Turbo/ ANSYS® system shows promise as a useful tool for estimating the response of impeller blades to unsteady aerodynamic loads. Though there are discrepancies between experimental peak strain measurements and the MSU Turbo/ ANSYS® peak strain predictions, reasonable explanations for these discrepancies have been put forth. Additional assessments of this system should be performed. Such a project would need to meet the following requirements to eliminate, or at least mitigate, the aforementioned sources of error:

- Capture blade-to-blade variations during testing, using advanced measurement techniques rather than strain gauges.

[2] As described in Section 2.2.2, the half-power technique (also known as the half-power bandwidth method and the 3dB method) is a technique used to estimate damping for the single degree of freedom systems of viscoelastic materials. In this technique, the structural damping factor is estimated by finding the difference in the two frequencies on either side of resonance where the amplitude is $1/\sqrt{2}$ times the resonant amplitude, then dividing the difference by the resonant frequency [29].

- Obtain precise information about the operating point(s) at which the strain measurements are taken, particularly the corrected mass flow rates.
- Explore various techniques for estimating aerodynamic damping.

3.3 Time-Averaged Performance

In the preceding section, it was shown that the MSU Turbo code and the CFD/ ANSYS® system provided adequate estimates of time-averaged flow results for a given geometry, and for estimating the vibratory responses of impeller blades to unsteady aerodynamic loading. The focus of the computational tool assessment now shifts to the ability of MSU Turbo to capture the changes in time-averaged compressor performance between the production and the enhanced geometries associated with effect of the change in vaneless space (i.e. impeller-diffuser gap) on impeller performance.

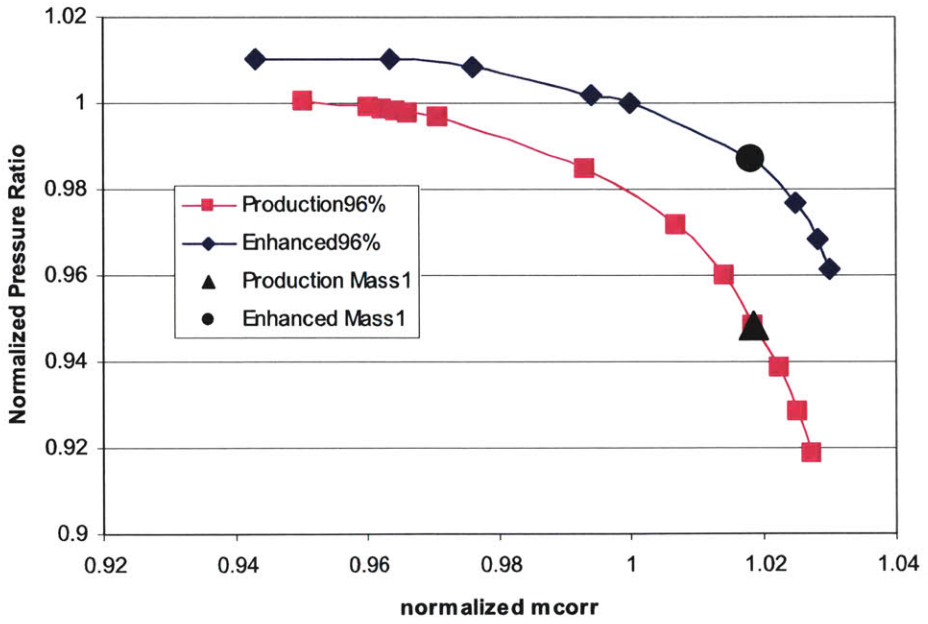

Figure 3.6 - 96% speedlines for the production and enhanced compressors generated by MSU Turbo

To perform this assessment, the production and the enhanced compressor time-averaged performance metrics are compared at the same corrected speed (96.2%) and the same

corrected flow. To locate operating points at the same corrected flow for the production and the enhanced compressors, several iterations were required, since mass flow is an output from MSU Turbo, rather than an input. To this end, speedlines were computed for both the production and enhanced compressors using MSU Turbo (Figure 3.6) by slowly increasing the backpressure for each compressor design to find points closer to stall and decreasing the backpressure to find points closer to choke. For the speedlines presented in Figure 3.6, each point represents one set of 3-D, unsteady stage calculations, where a stage consists of a single impeller followed by a diffuser. The points used for the assessment presented in this section are labeled Production Mass1 and Enhanced Mass1 in Figure 3.6.

Though there is no test data available for direct comparison, it is known that aerodynamic rig tests, performed at Honeywell ES&S during the redesign process, showed that the redesign did improve the performance of the compressor as intended. This improvement is reflected in the fact that the speedline for the enhanced compressor is higher than that of the production at a given mass flow in Figure 3.6. Instead of looking to test rig data for an in-depth assessment of the adequacy of MSU Turbo for estimating changes in performance, the TURBO estimates are instead compared with trends previously reported by Phillips [17], Shum [18], Shum, Tan and Cumpsty [19], Murray [22] and Murray and Tan [23]. While the two data points are not sufficient to determine the existence of optima, it is shown that the TURBO estimates are in agreement with previously documented trends.

3.3.1 Impeller and Stage Performance.

3.3.1.1 Pressure Ratio

The effect of the change in vaneless space (impeller-diffuser gap) on the normalized time-averaged total pressure rise through various stage components is tabulated below in Table 3.3. From this table, it is shown that decreasing the vaneless space (impeller-diffuser gap) has increased the stage total pressure ratio by 4%. This increase in pressure ratio is consistent with the speedline in Figure 3.6 and with the redesign intent.

Furthermore, Table 3.3 shows that the pressure ratio is due to both an increase in the impeller performance, and an increase in the diffuser performance.

	Production	Enhanced
Π_t impeller (normalized)	1.04	1.06
Π_t vaneless space (normalized)	0.21	0.21
Π_t diffuser (normalized)	0.20	0.21
Π_t stage (normalized)	0.95	0.99

Table 3.3 - Pressure rise across stage components and across the stage at Mass 1.

3.3.1.2 Impeller Performance: Gap-to-pitch ratio

The effect of a change in the size of the impeller-diffuser gap on centrifugal compressor performance was previously explored by Shum [18,19]. Murray [22] then postulated, based upon his research into the effect of diffuser blade count on impeller performance and upon Shum's results, that impeller performance is characterized by the ratio of the impeller-diffuser gap and the diffuser vane pitch, or the 'gap-to-pitch' ratio. To compare the trends estimated by TURBO with the trends elucidated by Murray (Figures 3.7 and 3.8), the impeller total pressure rise and isentropic efficiency have been tabulated along with the gap-to-pitch ratio for the production and enhanced geometries (Table 3.4).

	Production	Enhanced
Gap-to-pitch ratio	0.314	0.295
Π_t impeller (normalized)	1.04	1.06
Impeller efficiency (normalized)	1.0	1.02
Impeller entropy generation (normalized)	1.0	0.80

Table 3.4 - Effect of gap-to-pitch ratio on impeller performance.

Murray examined two different sets of compressors that cannot be compared directly; however, using a normalization scheme developed by Thomas Bartsch [30], it is possible

to collapse the data from the two different compressors examined by Murray onto a single correlative curve, shown in Figures 3.7 and 3.8. It is not possible to place the results for the production and enhanced compressor on these curves, because the normalization scheme requires information on the impeller efficiency and total pressure ratio at a gap-to-pitch ratio of unity, which is unavailable for this set of compressors.

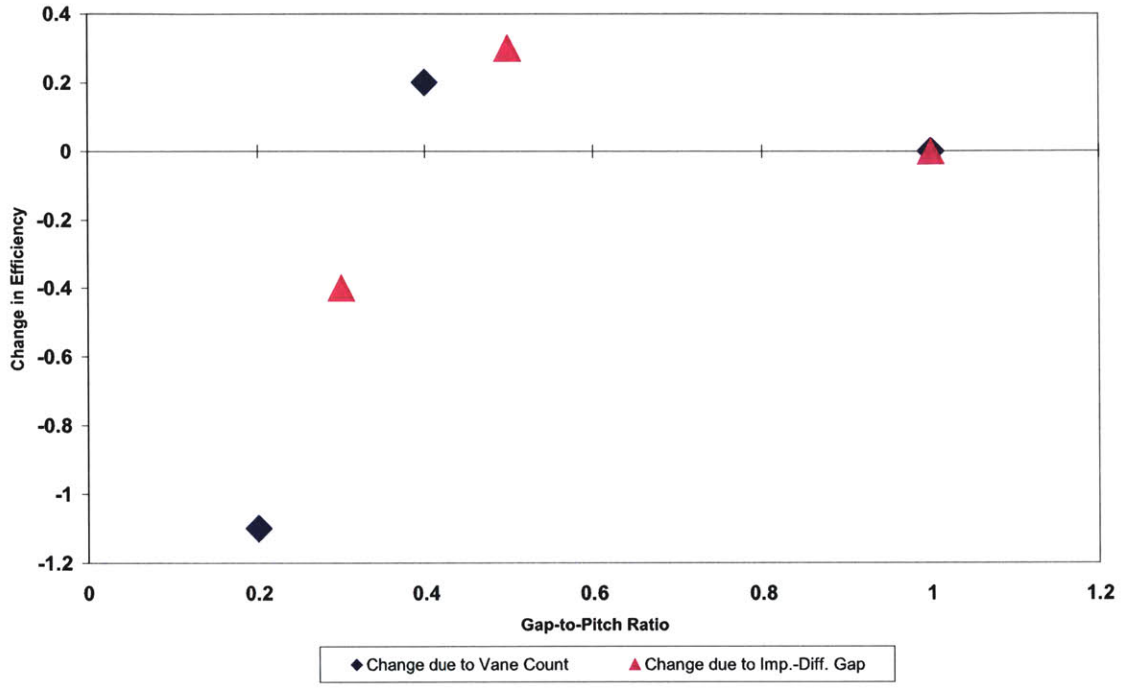

Figure 3.7 - Change in impeller efficiency with gap-to-pitch ratio for two centrifugal compressors of different designs [30].

Furthermore, to determine the existence of a gap-to-pitch ratio at which the production/ enhanced set of compressors has an optimum performance, computations for at least one more compressor (similar to the production and the enhanced compressor, but with a smaller gap-to-pitch ratio) is required. However, these two caveats do not preclude a comparison of the trends calculated by MSU Turbo for the production and the enhanced designs with the trends previously reported by Murray. Figures 3.7 and 3.8 show that in the region where total pressure ratio is increasing with increasing gap-to-pitch ratio, efficiency is increasing as well, and when total pressure ratio is decreasing with gap-to-pitch ratio, so is the efficiency. The fact that the impeller performance improved with the redesign of the production compressor (performance improved with decreasing gap-to-

pitch ratio) implies that the performance trends estimated by TURBO for the production and enhanced compressors should correspond to the negatively sloped portion of Murray's performance curves. An examination of the computed data in Table 3.4 reveals that both the normalized total pressure ratio and the normalized efficiency are increasing with decreasing gap-to-pitch ratio, which corresponds to the negatively sloped portion of the performance vs. gap-to-pitch ratio curve.

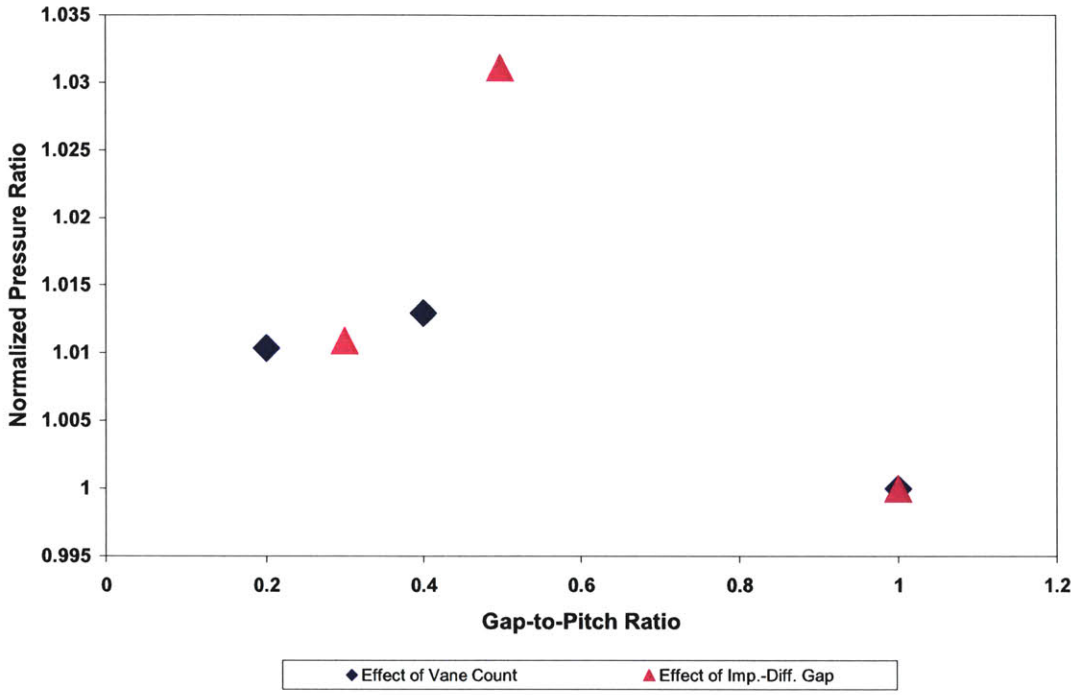

Figure 3.8 - The change in total pressure ratio across the impeller with gap-to-pitch ratio for two compressors of different design [30].

3.3.2 Diffuser Pressure Recovery

The last performance metric to be compared with previous works is the diffuser pressure recovery coefficient (Cp). It has been determined [12,16-18,21-22] that the alignment of the diffuser inlet flow with the diffuser vane angle is the dominant factor in determining the diffuser pressure recovery behavior. Therefore, if the TURBO- computed results show a change in flow alignment with the diffuser, a corresponding change in Cp is expected.

	Momentum-averaged incidence angle	Normalized Cp
Production	-20°	1.00
Enhanced	-19°	1.08

Table 3.5 - Change in Cp with momentum-averaged incidence angle

Table 3.5 tabulates the momentum-averaged diffuser inlet incidence angle and mass-averaged Cp. Incidence angle is the difference between the inlet flow angle (swirl) and the blade angle; a less negative flow angle implies better alignment of the flow with blade angle. From Table 3.5, it may be deduced that decreasing the vaneless space (going from the production to the enhanced design) improved the inlet flow alignment by 1°, resulting in an 8% increase in Cp.

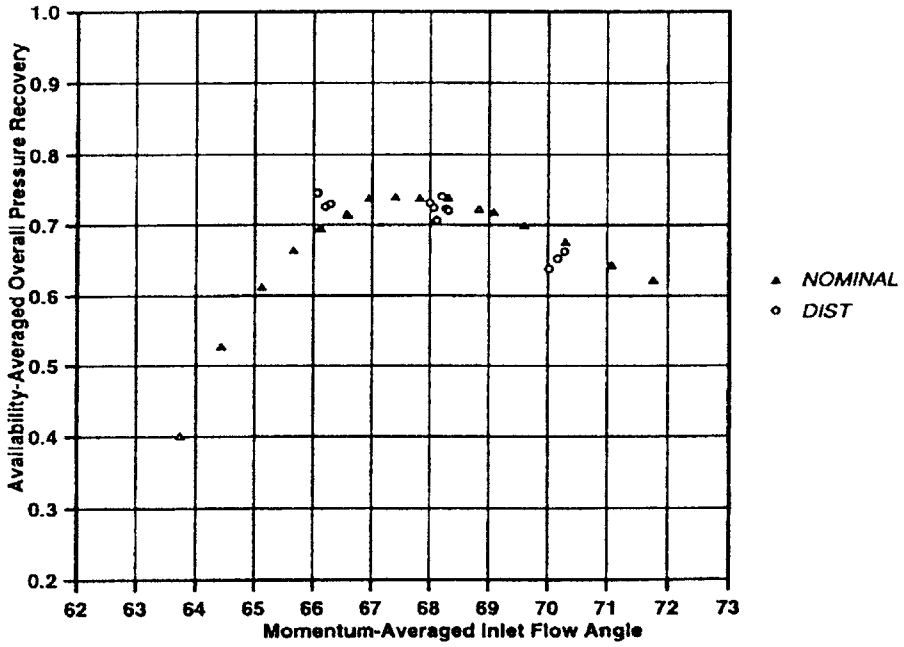

Figure 3.9 - Change in availability-averaged diffuser pressure recovery with momentum-averaged diffuser inlet flow angle from Phillips [17].

Now that it has been shown that Cp is increasing with inlet flow alignment, as expected, the remaining issue to be addressed is whether the degree of increase estimated by

TURBO is reasonable. The variation of availability-averaged Cp with momentum-averaged inlet flow angle calculated by Phillips [17] is illustrated in Figure 3.9. Depending on the location, it is possible for Cp to increase by as much as 25-30%, or as little as 0%, with a 1° change in inlet flow angle (which is equivalent to a 1° change in inlet incidence angle. Using this metric, the estimated 8% increase in Cp between the production and the enhanced geometries is deemed to be well-within reasonable bounds. Thus, it is found that MSU Turbo adequately estimates the trends of the change in Cp due to the change in vaneless space.

3.4 Chapter Summary

This chapter assessed the adequacy of the MSU Turbo CFD code and the MSU Turbo/ ANSYS® system as tools for capturing changes in the flow field due to a change in the vaneless space and for estimating the vibratory responses of impeller blades to unsteady aerodynamic loads.

In the various assessments of MSU Turbo as a stand-alone CFD code, it was found that TURBO results were reasonable compared with test results, with ADPAC simulation results, and with trends reported by Phillips [17], Shum [18], Shum, Tan and Cumpsty [19], Murray [22] and Murray and Tan [23]. Three types of trends led to this conclusion. The first is that the TURBO-computed work characteristics for the production and enhanced geometries were similar to the test data and to the ADPAC-computed results. Secondly, the unsteady pressure patterns on the blade surfaces show that the unsteadiness occurs mainly on the pressure surface of the impeller main and splitter blades, is confined to the last 10-15% of the meridional extent of each blade, and increases from tip to hub. These findings are consistent with ADPAC-computed results. In addition, the confinement of unsteadiness to the last 10-15% of the meridional extent of each blade agrees with the findings by Shum [18,19]. Lastly, time-averaged performance metrics are consistent with the performance improvement experienced during testing and with the trends reported by Phillips [17], Shum [18], Shum, Tan and Cumpsty [19], Murray [22]

and Murray and Tan [23]; stage pressure ratio and efficiency increase with decreasing gap-to-pitch ratio, and Cp is increased with an improvement in diffuser inlet flow alignment with the diffuser blades. Based on the results described above, it can be argued that the MSU Turbo CFD code would be adequate for the task of distinguishing the unsteady flow fields of the two similar centrifugal compressor stages of nearly identical design: the production and enhanced stages.

The assessment of the use of the MSU Turbo/ ANSYS® system for estimating forced response of the impeller blades is implemented via comparing the strain estimates from MSU Turbo/ ANSYS® with those from using the ADPAC/ ANSYS® system and with strain gauge test data. It was found that the TURBO/ ANSYS® estimate for the production compressor matches the strain gauge data, an improvement over the ADPAC/ANSYS® estimate, which was only one-third of the peak strain encountered during testing. In contrast, the TURBO/ANSYS® estimate for the enhanced compressor is approximately two-thirds of the strain gauge data (similar to the estimate produced by the ADPAC/ ANSYS® system); however, several factors affecting these results have been identified (including uncertainty as to the operating conditions under which the strain gauge tests were performed), giving possible explanations for this discrepancy. These results lead to the inference that the MSU Turbo/ ANSYS® system has the potential of serving as a predictive tool for forced response behavior in centrifugal compressors.

Chapter 4

The Unsteady Flow Field

4.1 Introduction

Although the flow in centrifugal compressors is inherently unsteady in nature, time-averaged flow variables and performance metrics can provide valuable insight into the overall performance of a compressor. However, these time-averaged values cannot provide insight into the mechanisms in the flow field most responsible for causing the unsteady blade loading that leads to HCF. To investigate these mechanisms, the unsteady flow fields must be interrogated. In this chapter the unsteady flow fields of two similar centrifugal compressor designs (the production design, which encountered no aeromechanical difficulty, and the enhanced design, which encountered aeromechanical difficulty) are compared.

To allow for a direct comparison between the flow fields of the production and enhanced compressors, the two compressors must be analyzed at the same corrected flow and corrected speed. To this end, CFD calculations were performed at a corrected speed of 96.2% using MSU Turbo for each of the two designs. These calculations were performed iteratively at several different backpressures to locate operating points along the 96.2% speedlines at which the corrected flow into the production and enhanced compressors are the same. Once these points have been identified, the unsteady flow fields of the production and enhanced compressors are compared at two separate operating points. The first corrected flow at which the compressors are compared (Mass 1) is near what was assumed to be the design point for the ADPAC/ ANSYS® and MSU Turbo/ ANSYS® peak strain estimate calculations for the enhanced compressor at 96.2%; this point is shown as Production Mass1 and Enhanced Mass1 in Figure 4.1. The Mass 1 operating points are the points at which the time-averaged performance for the production

design and the enhanced design were compared in Section 3.3. The peak strain for a given compressor increases as the operating point is moved towards stall from a point near design [31]; therefore a comparison of the compressors at a corrected flow closer to stall than Mass 1 could provide further insight into the flow mechanisms leading to HCF difficulty. To this end, the production and enhanced compressors are compared at Mass 2, the second corrected flow value compared, which is closer to stall for both the production and the enhanced compressors (as shown in Figure 4.1, labeled as Production Mass2 and Enhanced Mass2).

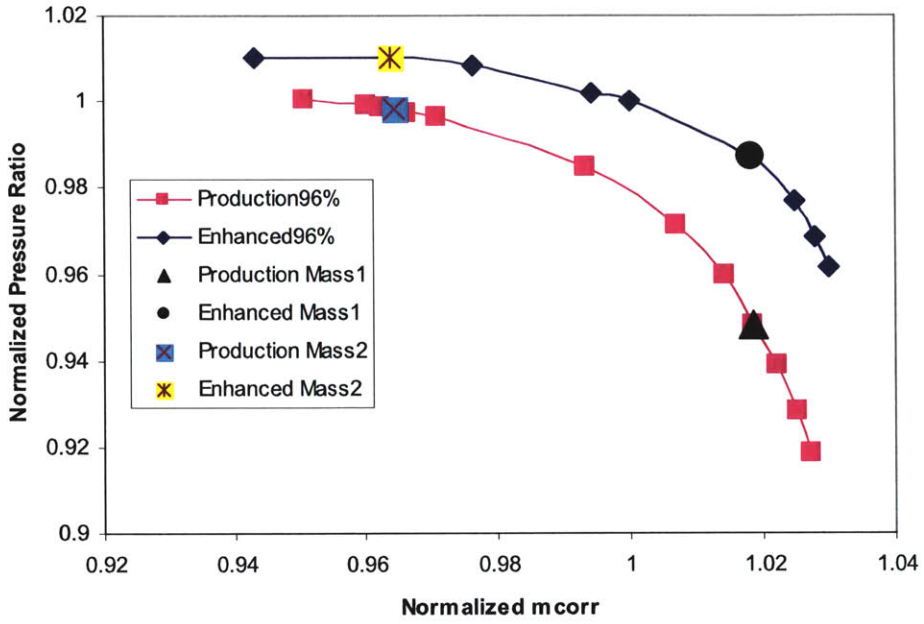

Figure 4.1 - 96.2% speedlines for the production and enhanced compressors generated by MSU Turbo.

In the ensuing sections, results are presented to show the differences between the unsteady flow fields of the production compressor (where the peak strains on the impeller blades remained within acceptable levels during testing) and the enhanced compressor (where strains exceeded acceptable levels during testing). At a given corrected flow (Mass 1 or Mass 2), the Mach number distribution, entropy generation distribution, inlet flow angle distribution, unsteady static pressure distribution and impeller blade loading in the unsteady flow fields of the production and enhanced compressors are compared. These comparisons show that there are definite differences in the unsteady flow fields of

the two geometries. Based on these findings, a hypothesis on the source of the unsteadiness leading to HCF is put forth; differences in the diffuser inlet incidence angle affect the unsteady pressure patterns in the impeller-diffuser gap, thus leading to differences in the unsteady blade loading, to cause a difference in the forced response behavior of the production and enhanced geometries.

4.2. The Impeller

4.2.1 The Impeller Passage – Unsteady Blade Loading

As stated in Section 1.1.2, forced response vibrations are the vibratory response of a system to external excitations. In the case of forced response in the impellers of centrifugal compressors, the external excitations are in the form of unsteady blade loading (in which blade loading is defined as the difference between the static pressure on the pressure surface (Pps) and the static pressure on the suction surface (Pss) of the impeller blades). Figures 4.2, 4.4, 4.6 and 4.8 show comparisons of the unsteady blade loading on the impeller main and splitter blades for the production and enhanced compressors at Mass 1 and Mass 2. In these plots, the blade loading is normalized by the dynamic pressure head based on the density at the impeller inlet and by the impeller tip speed. Each figure consists of three plots of normalized blade loading vs. percent meridional distance along the blade, which are arranged such that the plot corresponding to the blade loading near the hub (10% span) of the production and the enhanced designs is on the bottom and the plot containing information regarding the blade loading near the tip (90% span) is on top. In each plot, the solid lines indicate results for the enhanced design, and the dashed lines indicate results for the production design. For each type of line (solid or dashed), the top line (magenta) indicates the maximum loading encountered over one period, the middle line (green) is the time-averaged loading and the bottom line (blue) is the minimum loading encountered over one period. To estimate the maximum, minimum, and average values, the blade loading was calculated at 20 equally spaced time steps within one period, and the maximum, average, and minimum values at each

meridional location were calculated from these 20 values. Because the difference in the magnitude of the unsteadiness (as defined by the pressure envelope bounded by the maximum and minimum pressure loading) in the two compressor designs can be difficult to determine based upon these plots, Figures 4.3, 4.5, 4.7 and 4.9 show the results of plotting the difference between the maximum blade loading and the minimum blade loading vs. percent meridional distance. In comparing the blade loading of the production and enhanced compressors, the differences in the spatial variation of the blade loading and the degree of unsteadiness of the blade loading are examined below.

4.2.1.1 Impeller Main Blade

The blade loading on the impeller main blade for the production and enhanced compressors at Mass 1 is shown in Figure 4.2 and 4.3. Steady blade loading is the blade loading in which the minimum and maximum loading over time are equal; for these two compressor designs, the steady loading begins at the leading edge of the impeller and extends upstream to approximately 80% of the meridional distance of the impeller passage. From Figure 4.2, it is apparent that the spatial patterns of the steady blade loading of the production and enhanced compressors are similar near the hub, but dissimilarities begin to appear at mid-span; near the tip, the spatial loading patterns also show significant differences. Though it is difficult to determine which of the two compressors, the production or the enhanced, are more unsteady from Figure 4.2, Figure 4.3 indicates that near the trailing edge of the impeller main blades, near the hub and at mid-span, the unsteadiness (the difference between the maximum and minimum pressure loading over time) is greater in the enhanced compressor than in the production compressor. Near the tip, this relationship is not as clear; however, it may be stated that the maximum unsteadiness on the main blade in the enhanced compressor at Mass 1 is greater than or equal to that in the production compressor at Mass 1.

The trends describing the blade loading on the main blade for the production and enhanced compressors at Mass 1 can also be used to describe the trends in the blade loading on the main blades at Mass 2, shown in Figures 4.4 and 4.5. As in Figure 4.2,

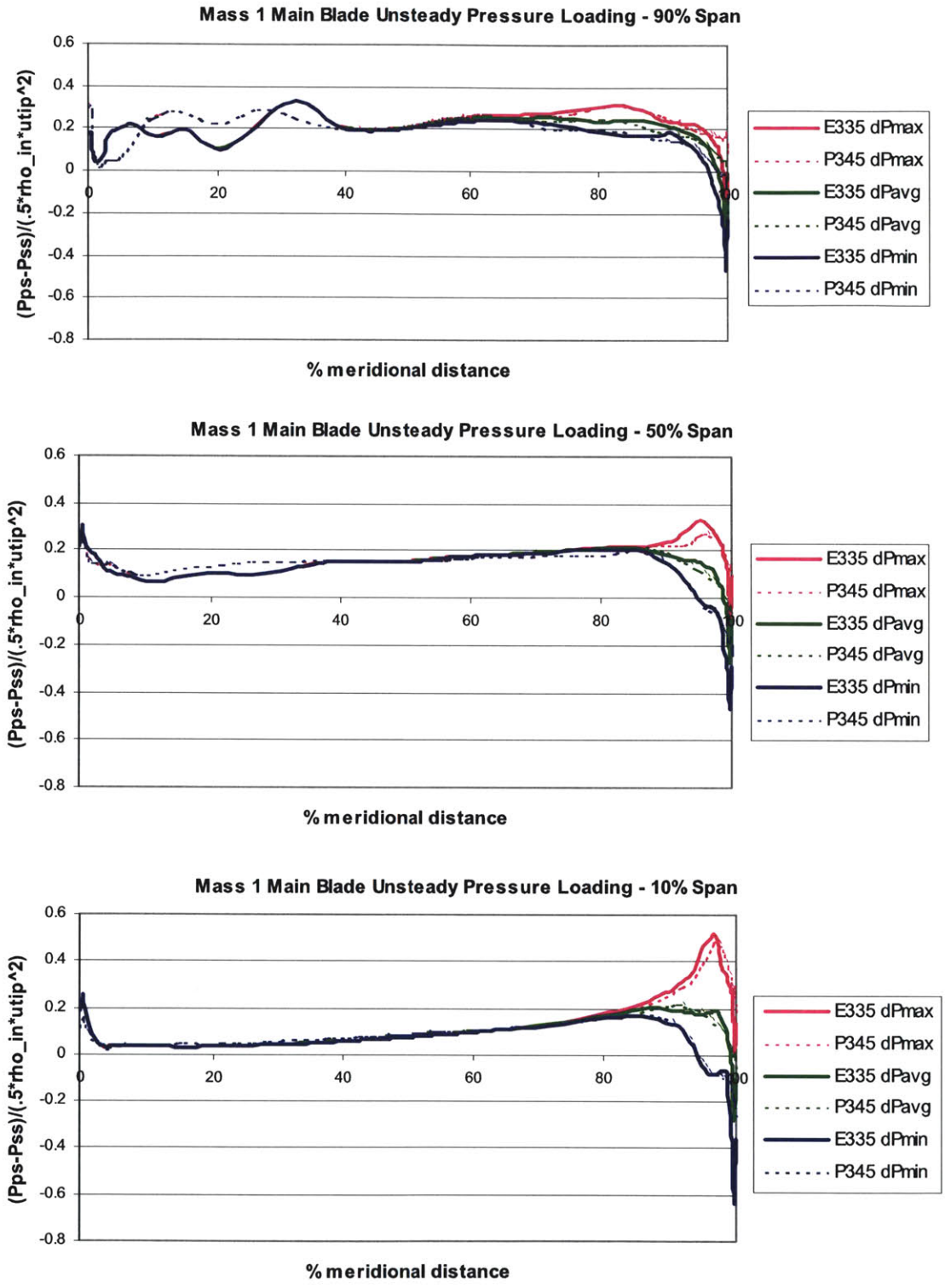

Figure 4.2 - Unsteady blade loading (normalized) on the main blade at Mass 1.

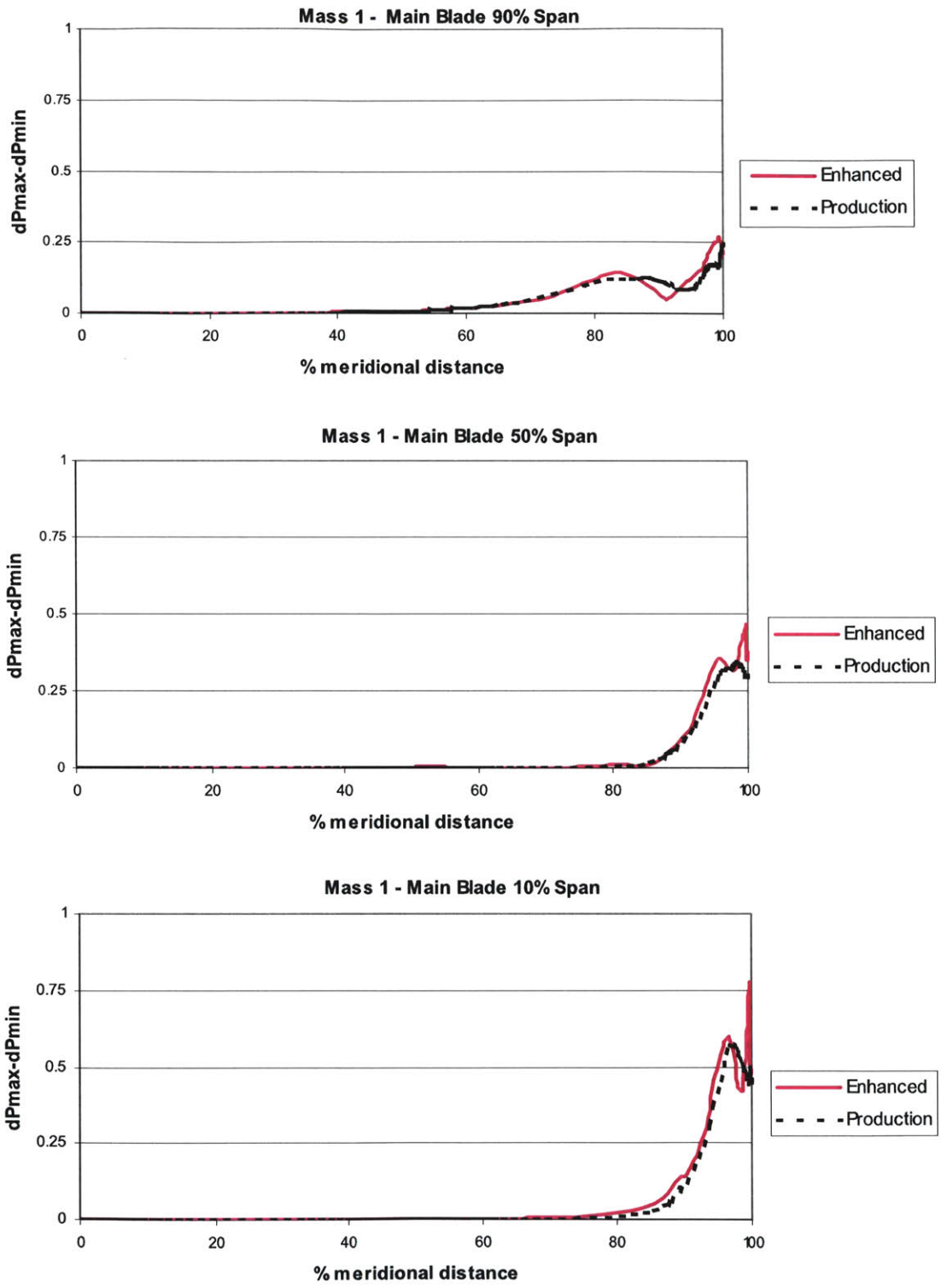

Figure 4.3 - Difference between the maximum blade loading over time $(Pps-Pss)_{max}$ and the minimum blade loading over time $(Pps-Pss)_{min}$ normalized by the dynamic pressure head $(.5*\rho_{in}*u_{tip}^2)$ along the main blade at Mass 1.

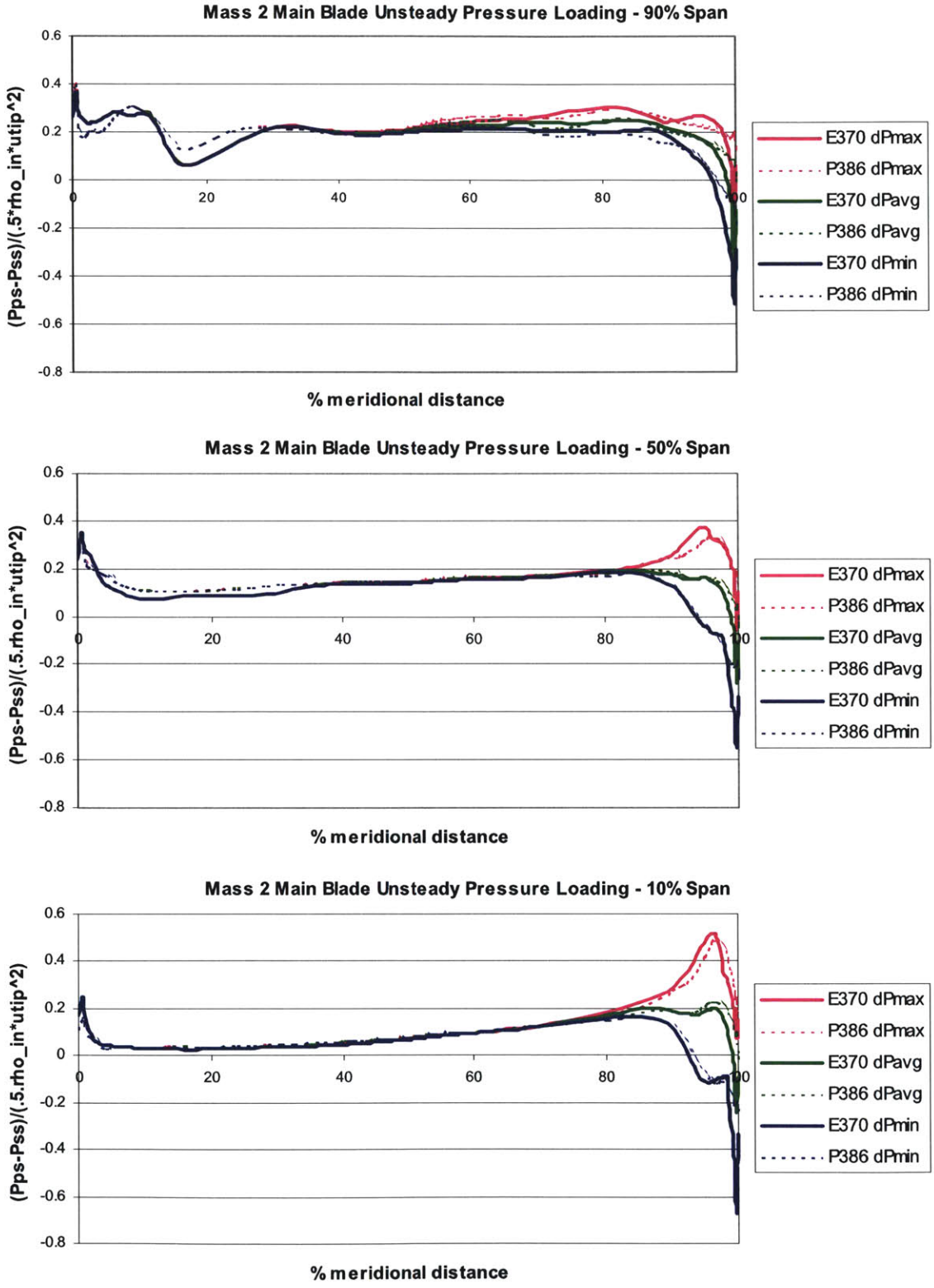

Figure 4.4 - Unsteady blade loading (normalized) on the main blade at Mass 2.

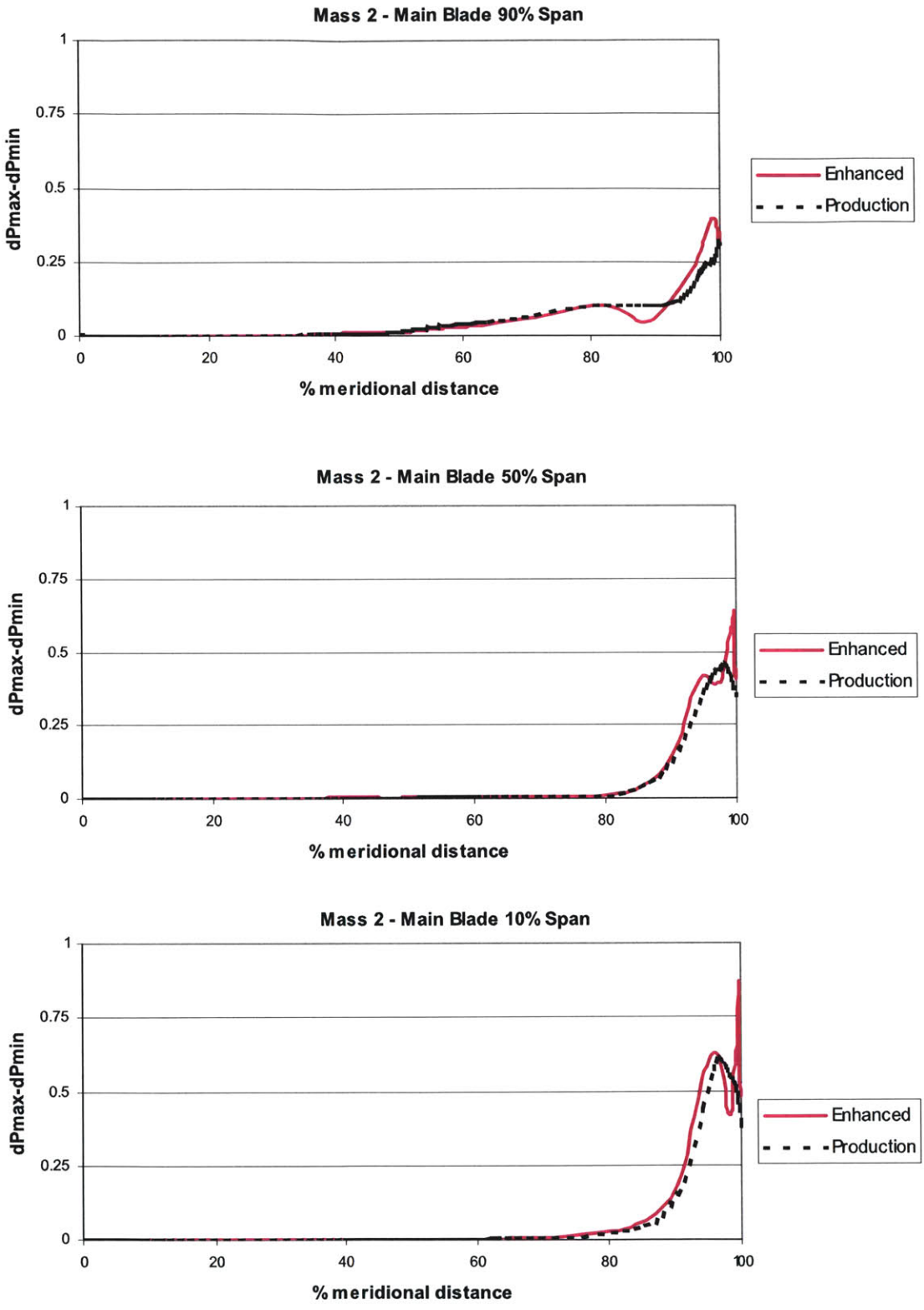

Figure 4.5 - Difference between the maximum blade loading over time $(Pps-Pss)_{max}$ and the minimum blade loading over time $(Pps-Pss)_{min}$ normalized by the dynamic pressure head $(.5*\rho_{in}*u_{tip}^2)$ along the main blade at Mass 2.

Figure 4.4 shows that the spatial patterns of the steady portion of the blade loading are similar at 10% span, but differ at mid-span and near the tip. Unlike Figure 4.2, Figure 4.4 shows a marked difference in the amount of unsteadiness in the production and enhanced compressors. From Figure 4.4, it can be discerned that at 10% and 50% span the unsteadiness is greater in the enhanced compressor than in the production compressor at Mass2. Near the tip, this relationship is not clear from Figure 4.4; however, Figure 4.5 clarifies the relationship, and it may be stated that at Mass 2, the unsteadiness is always greater in the enhanced compressor than in the production compressor. Furthermore, by comparing Figures 4.3 and 4.5, it can be inferred that the unsteadiness of the blade loading of the enhanced compressor impeller main blades at Mass 2 is greater than that for the enhanced compressor main blades at Mass 1; the same can be inferred for the production compressor. Thus, for a given compressor design, as the operating point moves from design towards stall, the unsteadiness in impeller main blade loading increases.

4.2.1.2 Impeller Splitter Blade

Comparisons of the blade loading on the impeller splitter blade for the production and enhanced compressors at Mass 1 are shown in Figures 4.6 and 4.7. As in the comparison of the impeller main blades at Mass 1, Figure 4.6 shows that there are spatial differences between the steady blade loading patterns on the impeller splitter blades of the production and enhanced compressors. However, in the splitter blade, these differences occur mainly at 90% span rather than at both 50% and 90% span (where they occur on the main blade). Figure 4.6 also clearly indicates that the unsteady blade loading envelope at 10% span of the enhanced compressor splitter blade at Mass 1 is larger near the trailing edge than that of the production compressor at Mass 1 near the trailing edge. An inspection of Figure 4.7 reveals that the unsteadiness of the blade loading is greater on the enhanced splitter blade than on the production splitter blade at both 10% and 90% span; at 50% span, the unsteadiness is approximately the same for both the production and the enhanced compressors. Thus it can be stated that the unsteadiness on the enhanced splitter blade at Mass 1 is always greater than or equal to the unsteadiness on the

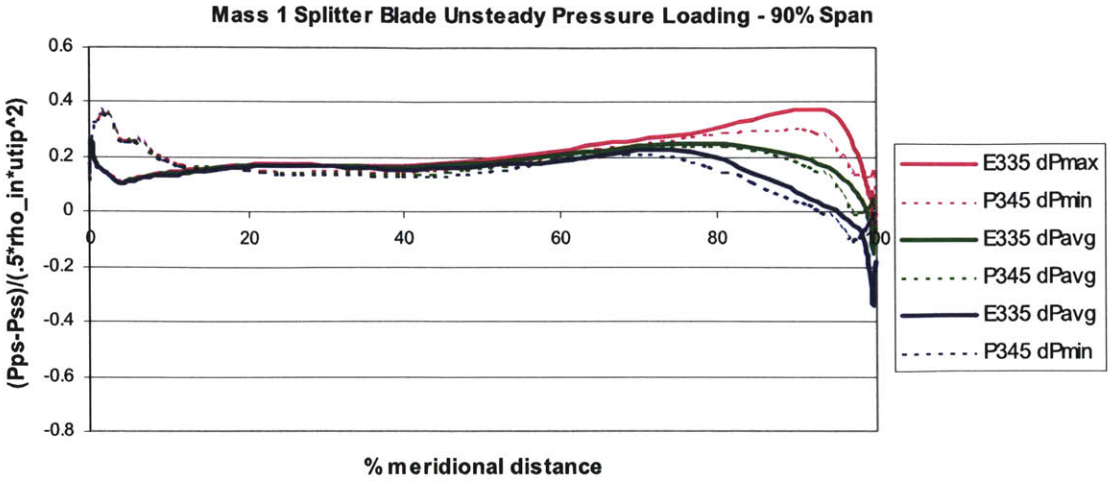

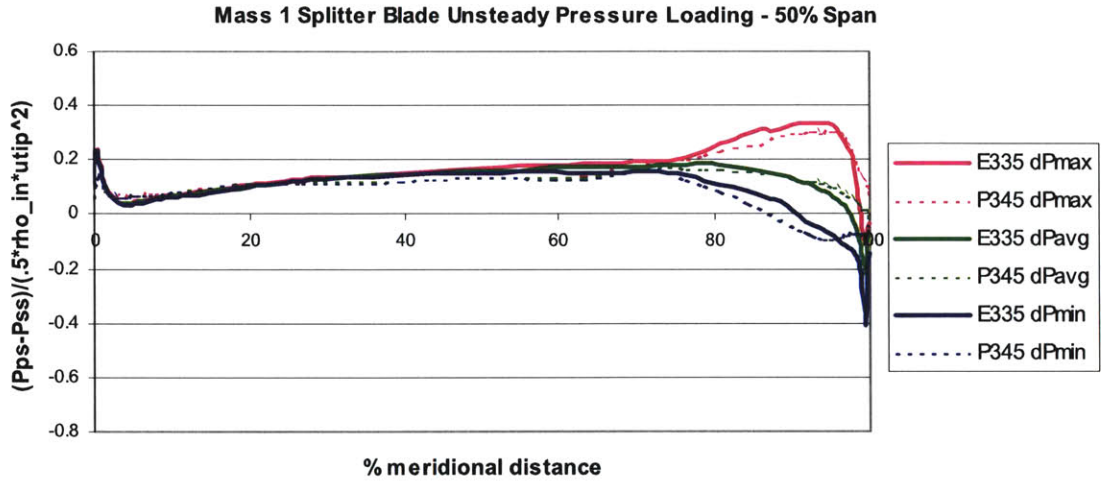

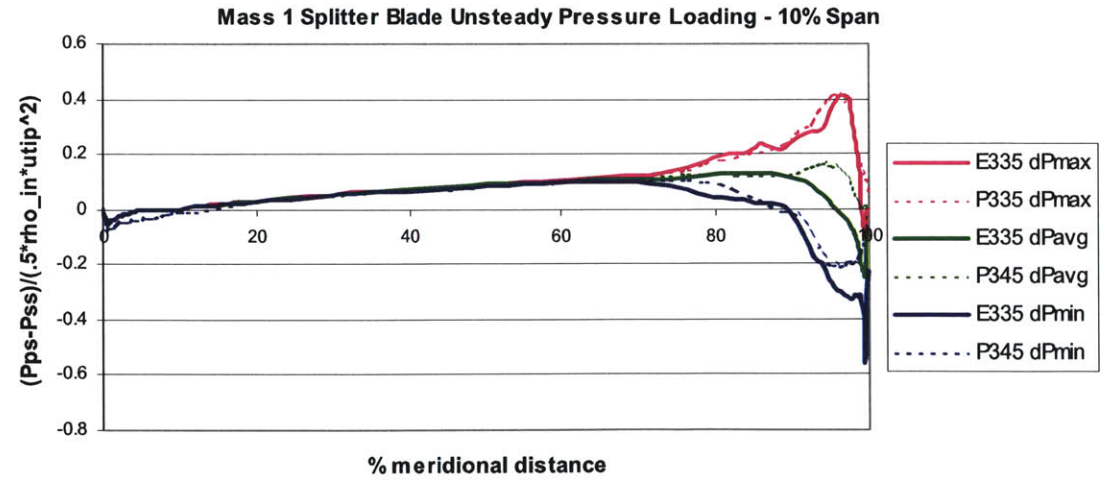

Figure 4.6 - Unsteady blade loading (normalized) on the splitter blade at Mass 1.

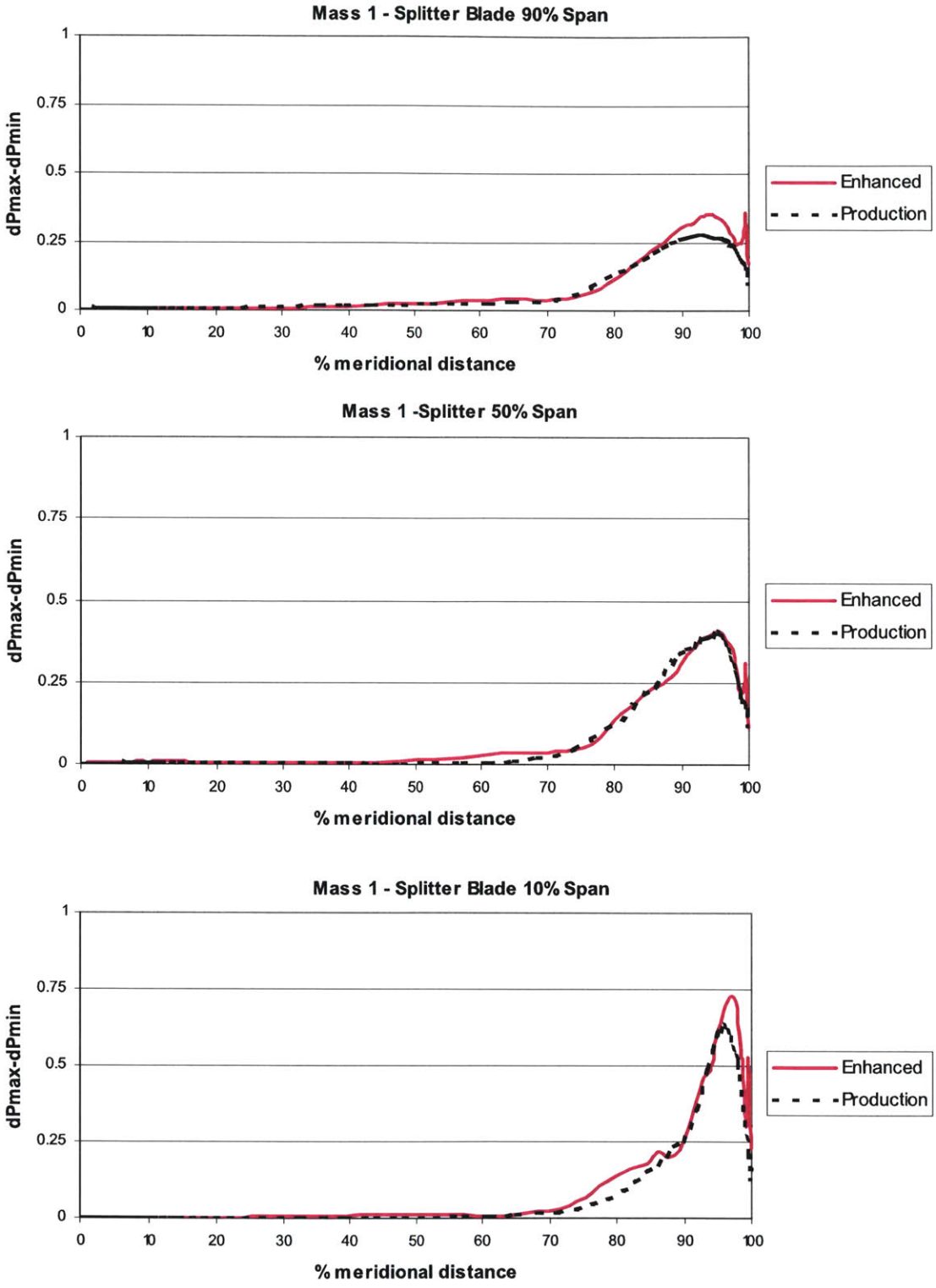

Figure 4.7 - Difference between the maximum blade loading over time $(Pps\text{-}Pss)_{max}$ and the minimum blade loading over time $(Pps\text{-}Pss)_{min}$ normalized by the dynamic pressure head $(.5*\rho_{in}*u_{tip}^2)$ along the splitter blade at Mass 1.

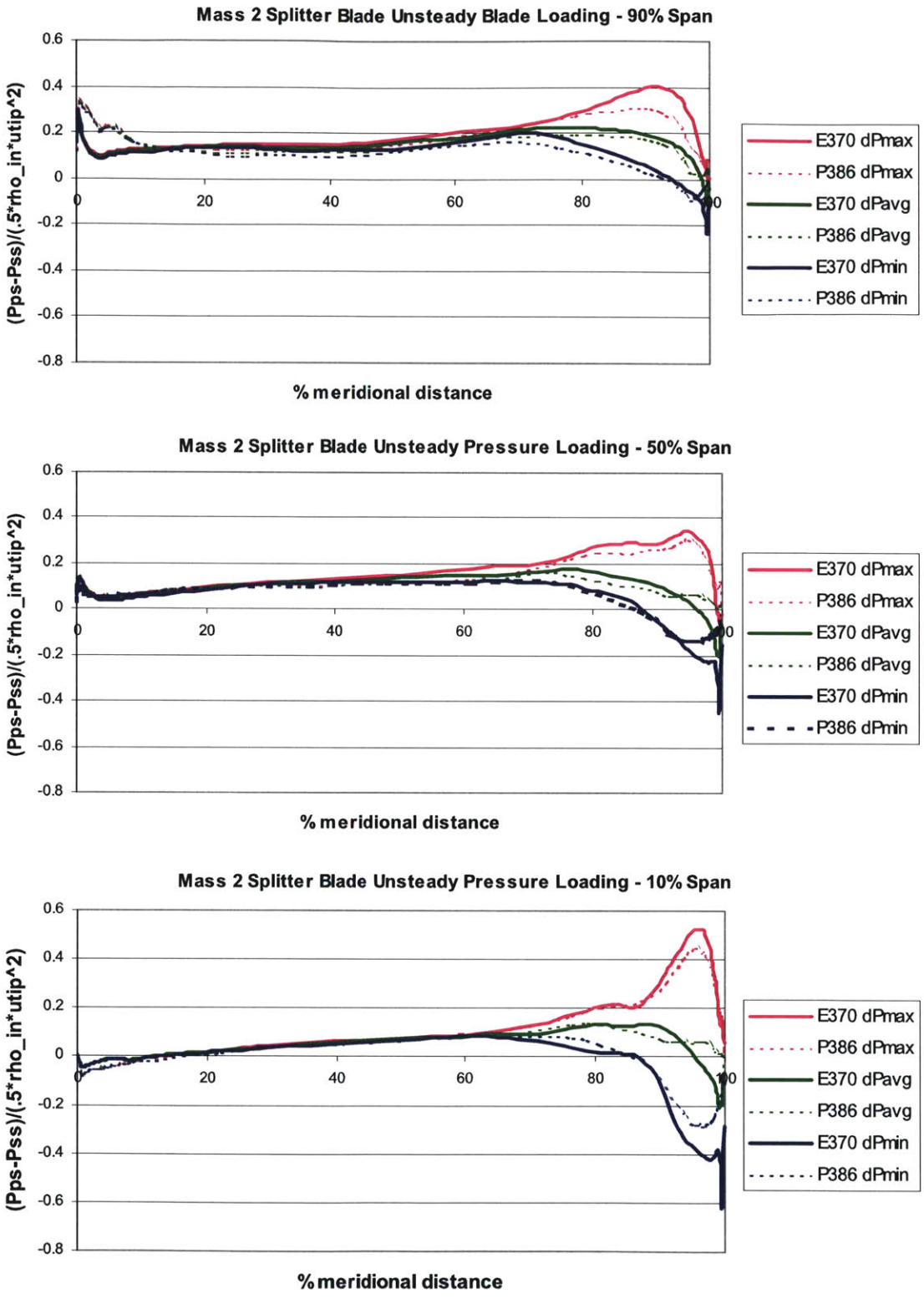

Figure 4.8 - Unsteady blade loading (normalized) on the splitter blade at Mass 2.

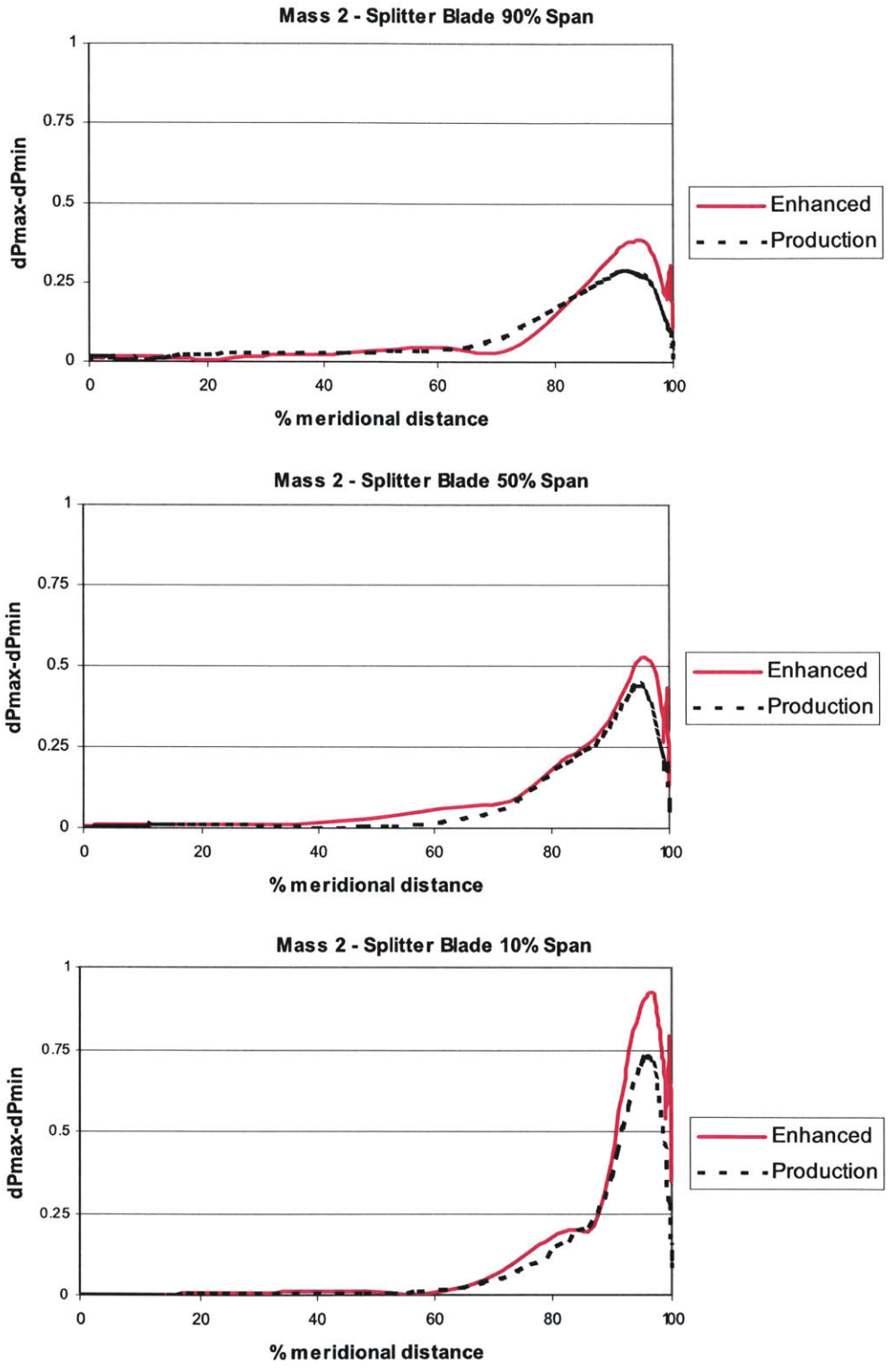

Figure 4.9 - Difference between the maximum blade loading over time $(Pps\text{-}Pss)_{max}$ and the minimum blade loading over time $(Pps\text{-}Pss)_{min}$ normalized by the dynamic pressure head $(.5*\rho_{in}*u_{tip}^2)$ along the splitter blade at Mass 2.

production splitter blade at Mass 1; this trend is the same as the trend of the unsteadiness on the impeller main blades at Mass 1.

As is the case for the main blades, the trends describing the blade loading on the splitter blade for the production and enhanced compressors at Mass 1 can also be used to describe the trends in the blade loading on the splitter blades at Mass 2, shown in Figures 4.8 and 4.9. At the operating points at Mass 2, the spatial pattern of the steady pressure loading on the splitter blades (shown in Figure 4.8) differs between the two compressors at 90% only; this is similar to the trend in the spatial pattern found for the splitter blades operating points at Mass 1. It is possible to discern the relative unsteadiness of the blade loading on the production and enhanced compressor splitter blades from Figure 8 alone: the enhanced splitter blade loading is more unsteady than the production splitter blade throughout the entire span of the splitter blade at the Mass 2 operating points. The plots in Figure 4.9 corroborate this observation. Furthermore, by comparing Figures 4.7 and 4.9, it can be inferred that the unsteadiness in the blade loading on the enhanced compressor splitter blades at Mass 2 is greater than that the enhanced compressor splitter blades at Mass 1; the same can be inferred for the production compressor. Thus, for a given compressor design, as the operating point moves from design towards stall, unsteadiness in impeller splitter blade loading increases.

4.2.1.3 Summary of Blade Loading Observations

In comparing the results for blade loading on impeller main and splitter blades at Mass 1 and Mass 2, several trends are apparent. The first trend is that for the impeller main and splitter blades at a given corrected flow, the unsteadiness in the blade loading in the enhanced impeller is always greater than or equal to the unsteadiness in the blade loading in the production impeller. At Mass 2 (close to stall), this trend can be simplified even further: the unsteadiness in the blade loading is always greater in the enhanced impeller than in the production impeller. The second trend is that for a given compressor (production or enhanced) on a given blade (main or splitter), the unsteadiness increases as the corrected flow is moved from design towards stall (as it is moved from Mass 1 to

Mass 2). Lastly, the steady blade loading has different spatial patterns in the production and enhanced compressors near the tip for both the impeller main and splitter blades at Mass 1 and Mass 2; the spatial differences extend further along the blade span to 50% span for the main blades.

Now that the differences in the excitation source (the unsteady blade loading) for the forced response of the impeller blades of the compressors of similar design have been examined, the rest of this chapter will focus on determining the sources of these differences, beginning with an examination of the unsteady Mach number distribution and the entropy generation distribution at the impeller exit.

4.2.2 The Impeller Exit

Figures 4.10 – 4.13 show unsteady Mach contours at the impeller exit taken at time t=to (where to is the time at the beginning of the period), t=0.4 times the vane passing period (t=0.4T), and t=0.8T. These contours show that the differences between the Mach number distribution at the impeller exit of the production compressor and of the enhanced compressor are similar for both the corrected flows examined (Mass 1 and Mass 2). The first difference is that for both corrected flows (irrespective of time step), the jet Mach number is higher at the enhanced impeller exit than at the production impeller exit. The higher jet Mach number at the enhanced impeller exit is consistent with the expected increase in Mach number due to the increase impeller tip radius (and thus the increase in tangential velocity). Another difference between the impeller exit flows of the two geometries is that there is a smaller gradient in Mach number both along the blade trailing edge and across the blade trailing edge for the production compressor, as compared to the gradients in the enhanced compressor. One last difference in Mach number distribution of note is that there is a region of transonic flow at the exit plane where the splitter blade trailing edge meets the hub during some time instants for the enhanced compressor; such is not the case for the production compressor. This observation is accompanied by a caveat: only three time instants within one period are shown in Figures 4.10-4.13; it is possible that this difference is due to phase differences.

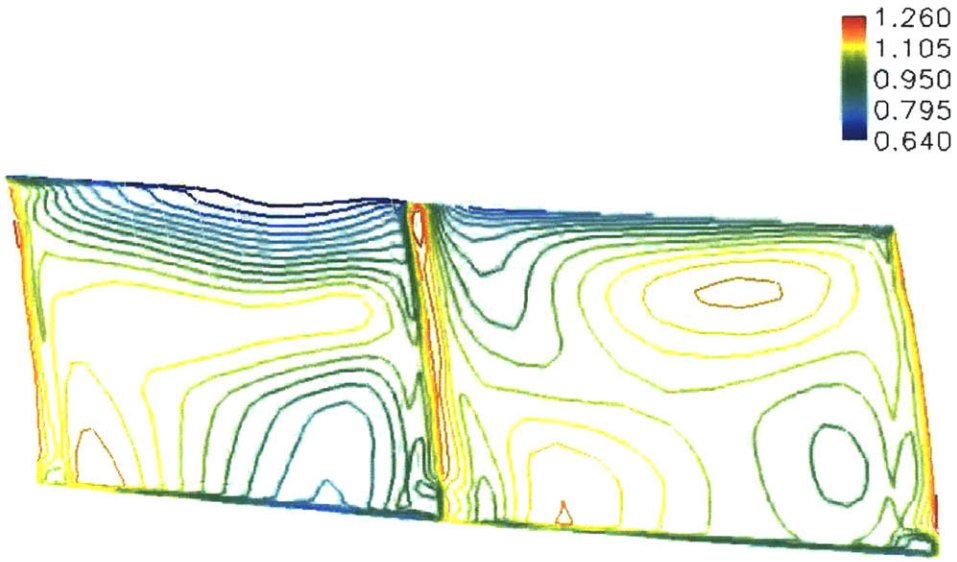

Figure 4.10a – Mass 1 - Mach contours at production impeller exit - t=to

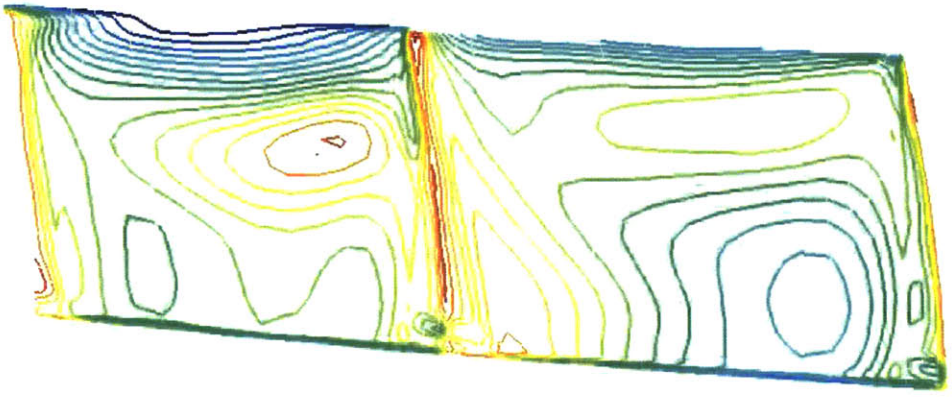

Figure 4.10b – Mass 1 - Mach contours at production impeller exit – t=0.4T

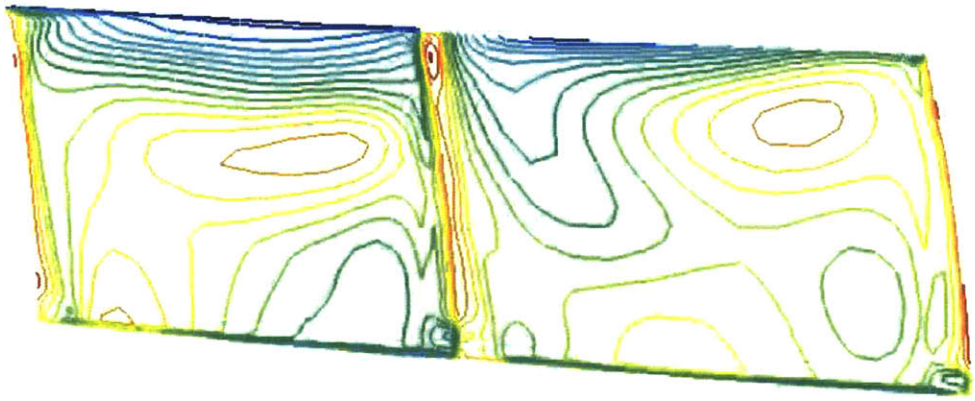

Figure 4.10c - Mass 1 - Mach contours at production impeller exit – t=0.8T

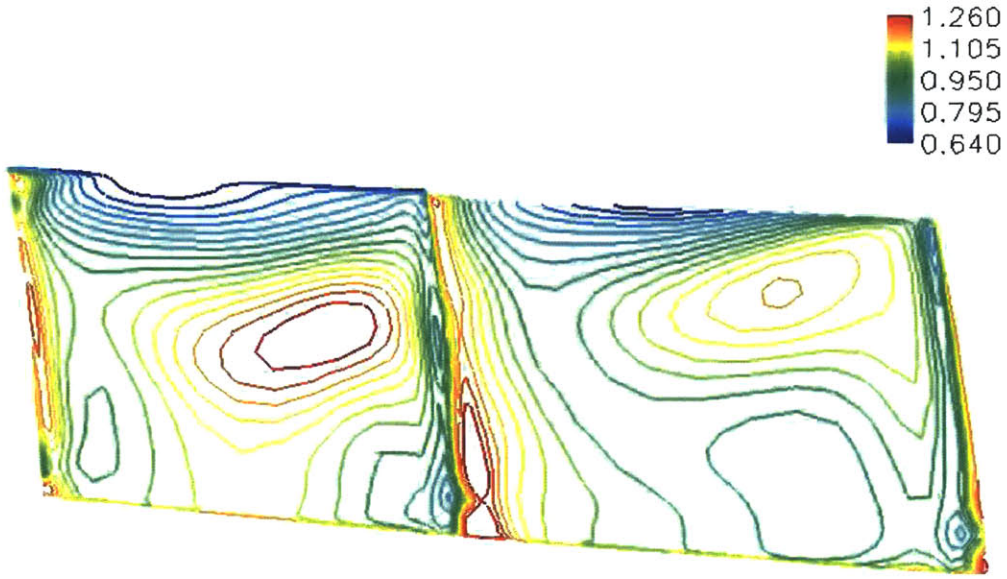

Figure 4.11a – Mass 1 - Mach contours at enhanced impeller exit - t=to

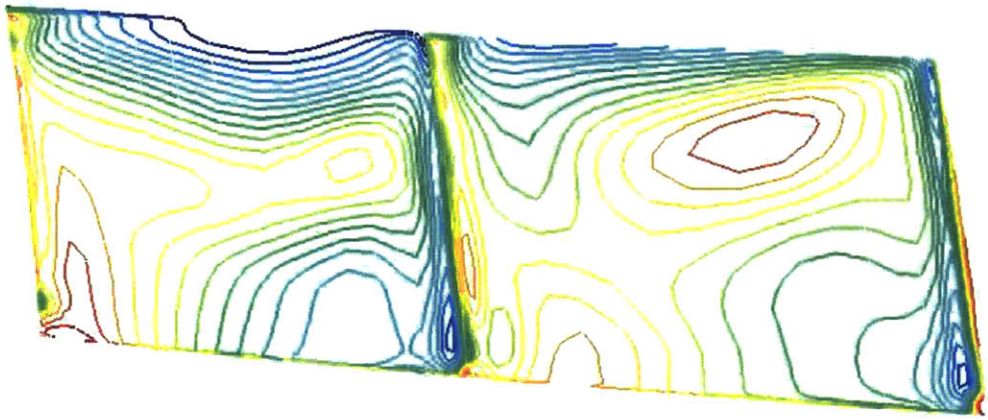

Figure 4.11b – Mass 1 - Mach contours at enhanced impeller exit – t=0.4T

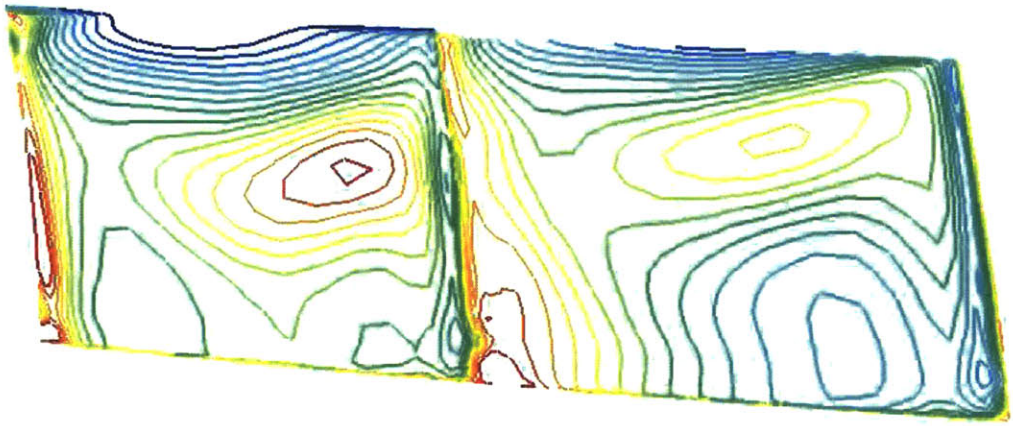

Figure 4.11c – Mass 1 - Mach contours at enhanced impeller exit – t=0.8T

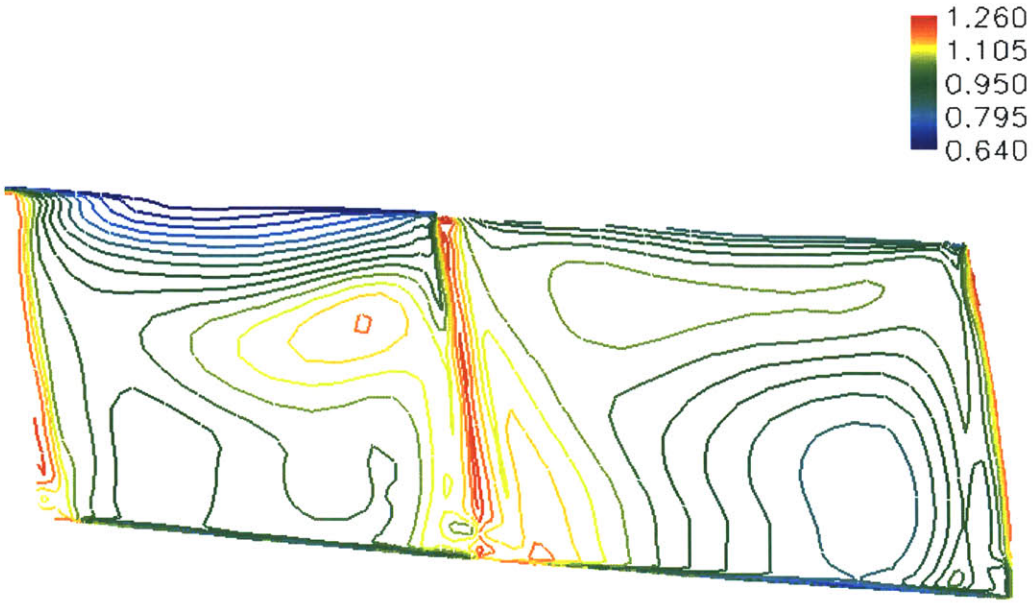

Figure 4.12a - Mass 2 - Mach contours at production impeller exit - t=to

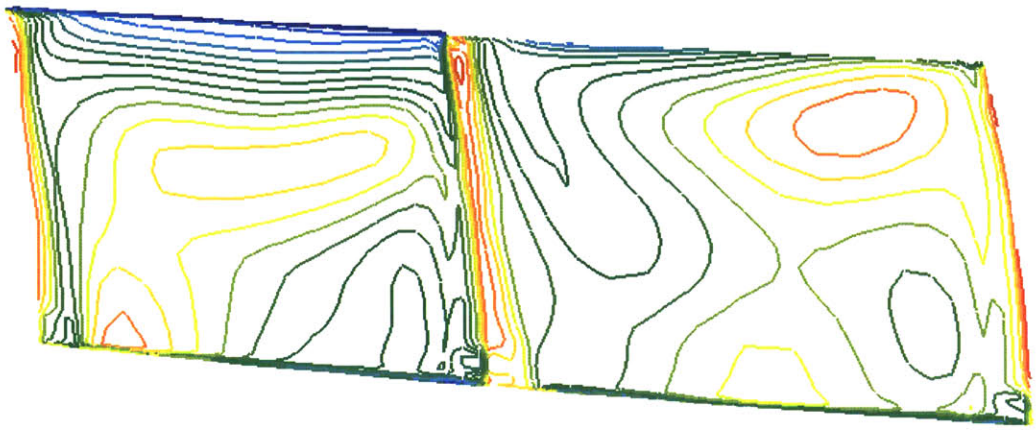

Figure 4.12b - Mass 2 - Mach contours at production impeller exit - t=0.4T

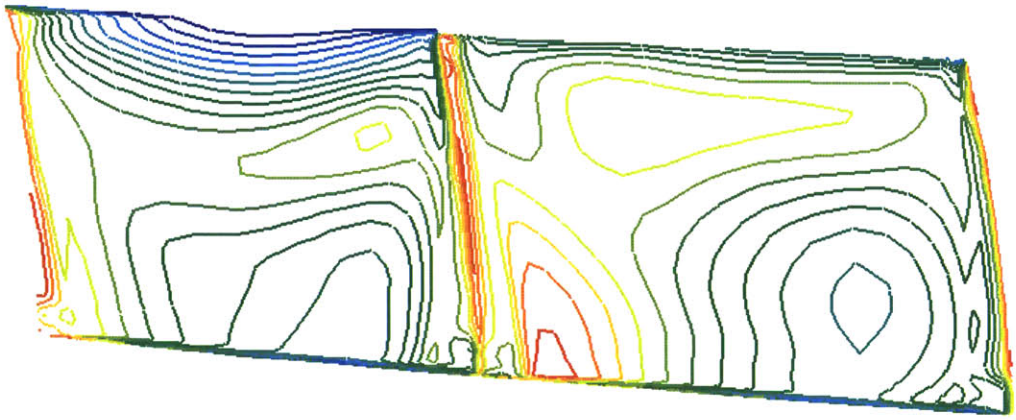

Figure 4.12c - Mass 2 - Mach contours at production impeller exit - t=0.8T

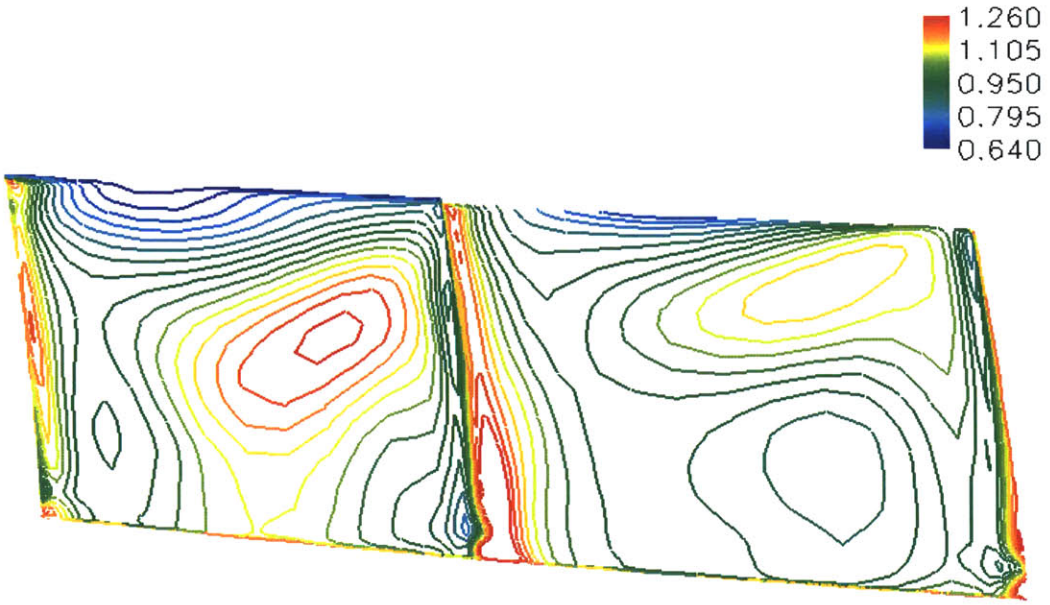

Figure 4.13a - Mass 2 - Mach contours at enhanced impeller exit - t=to

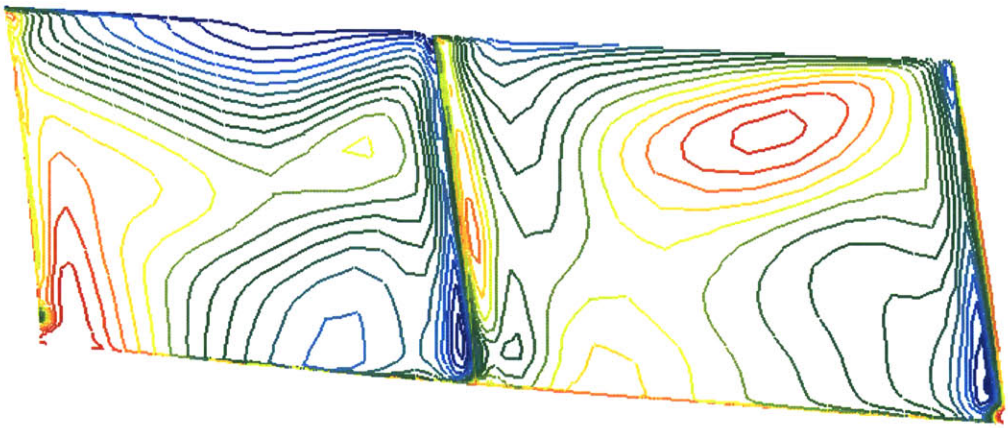

Figure 4.13b - Mass 2 - Mach contours at enhanced impeller exit - t=0.4T

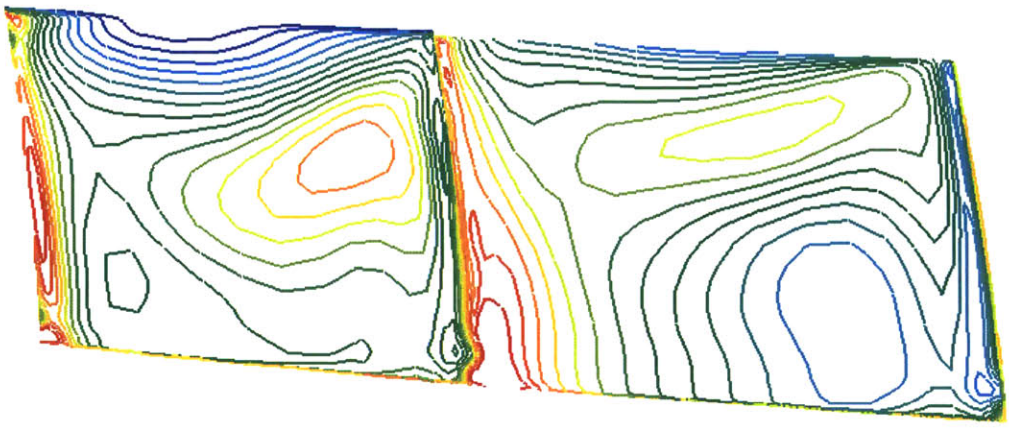

Figure 4.13c - Mass 2 - Mach contours at enhanced impeller exit - t=0.8T

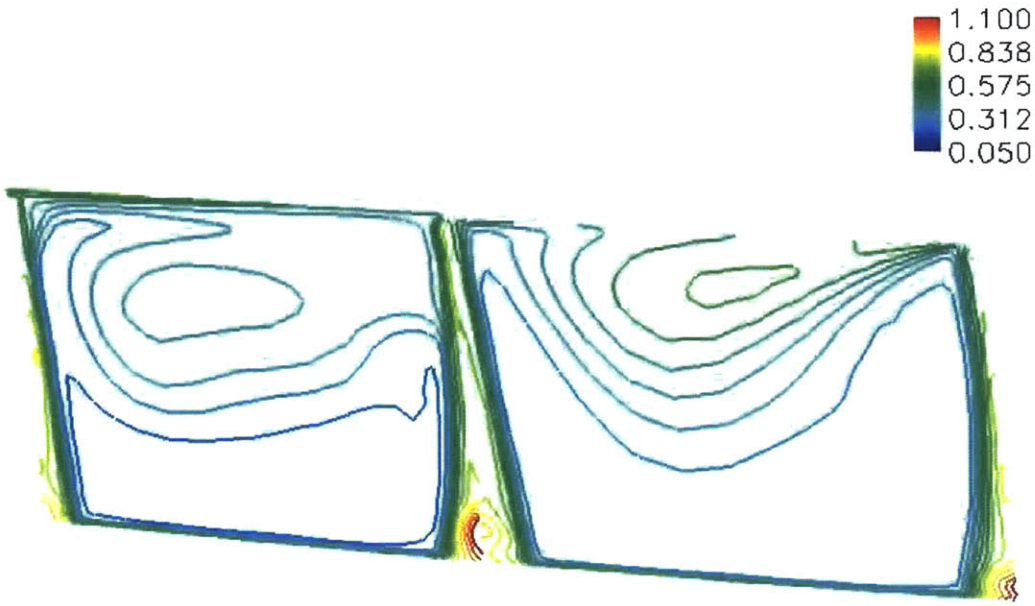

Figure 4.14a – Mass 1 - Entropy generation contour at production impeller exit – t=to

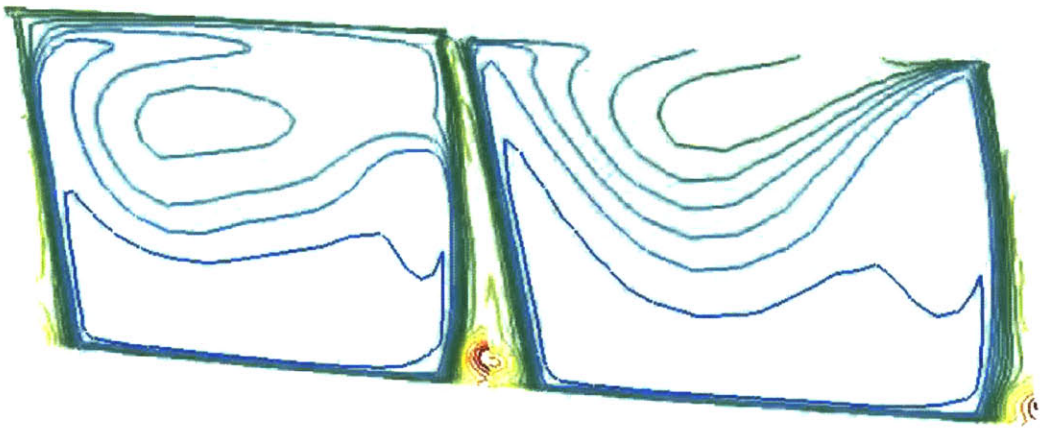

Figure 4.14b – Mass 1 Entropy generation contour at production impeller exit –t=0.4T

Figure 4.14c – Mass 1 - Entropy generation contour at production impeller exit – t=0.8T

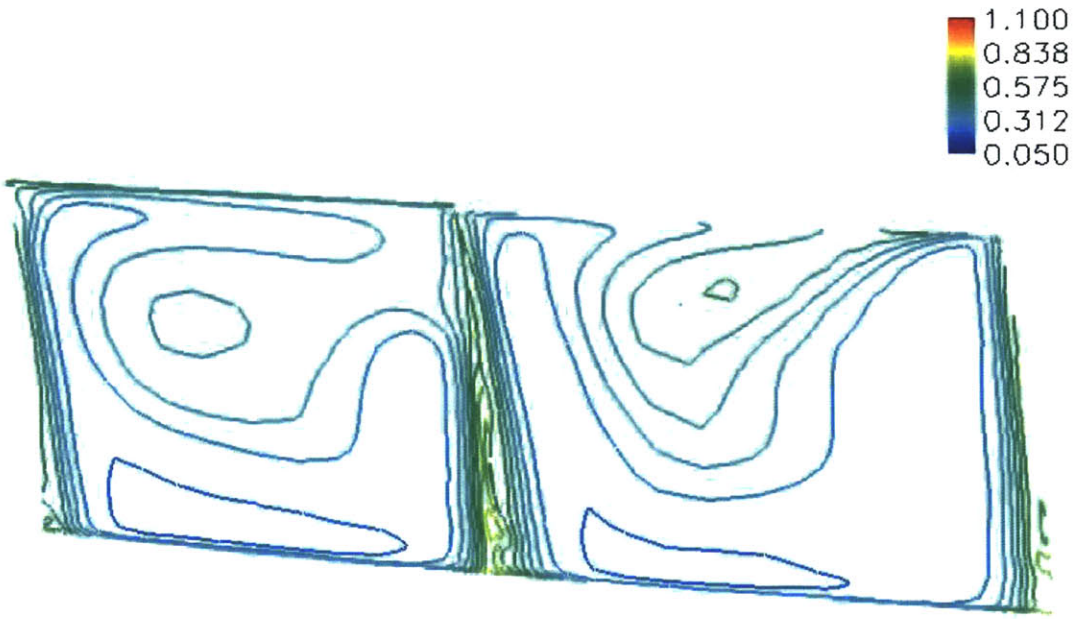

Figure 4.15a – Mass 1 - Entropy generation contour at enhanced impeller exit – t=to

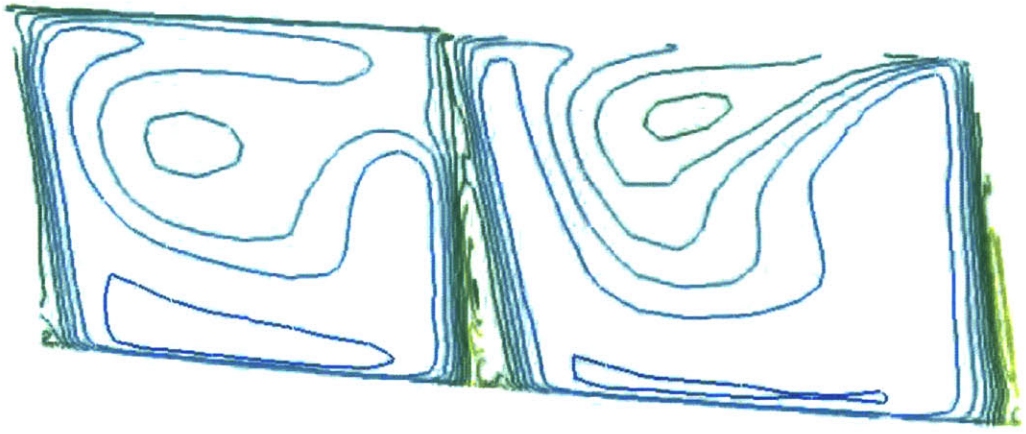

Figure 4.15b – Mass 1 - Entropy generation contour at enhanced impeller exit – t=0.4T

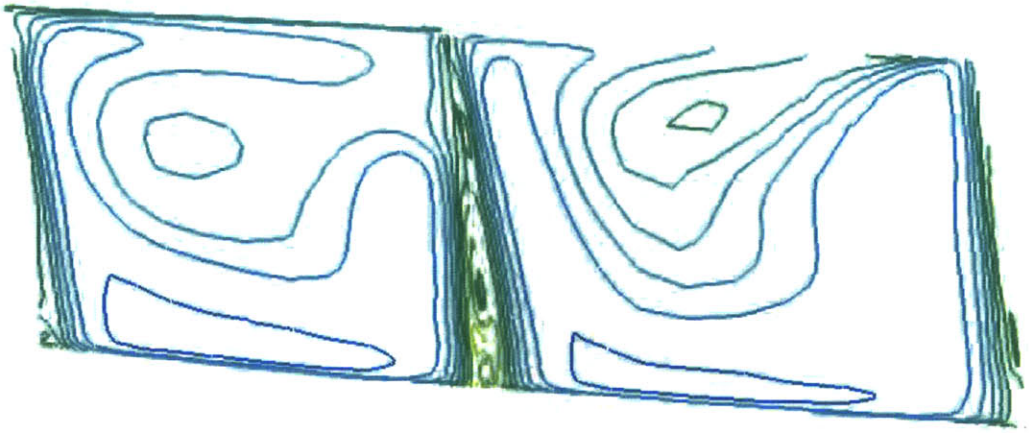

Figure 4.15c – Mass 1- Entropy generation contour at enhanced impeller exit – t=0.8T

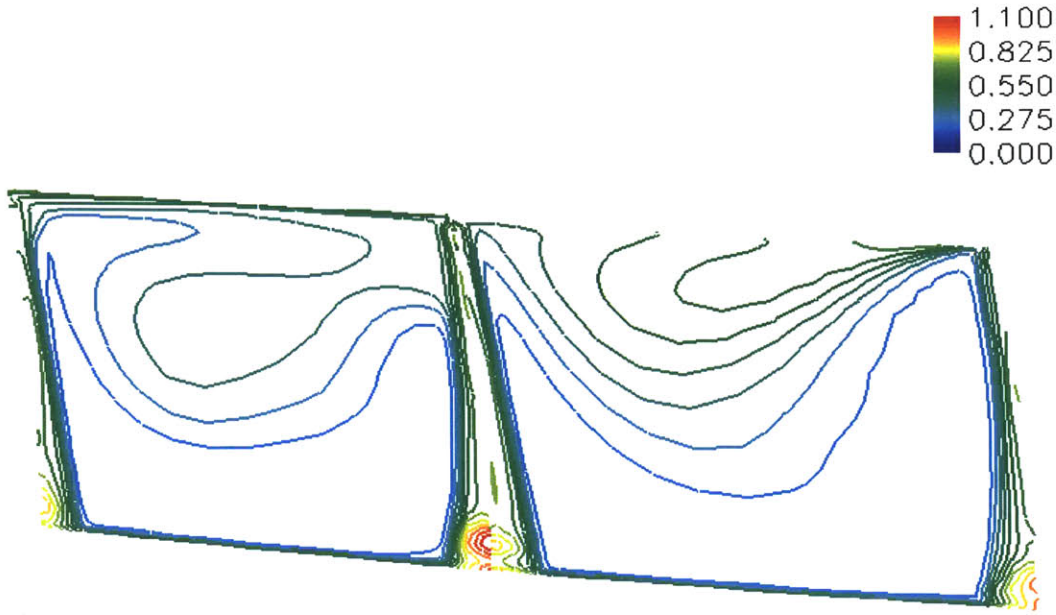

Figure 4.16a - Mass 2 - Entropy generation contour at production impeller exit – t=to

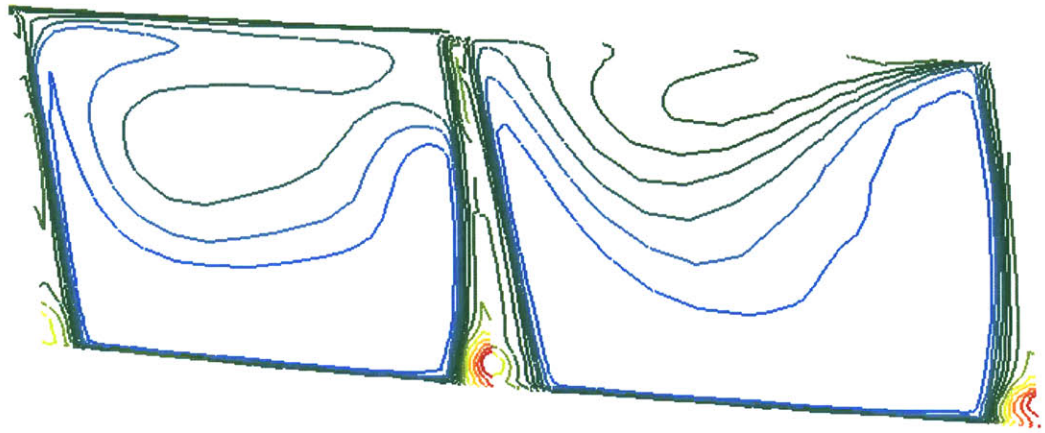

Figure 4.16b - Mass 2 - Entropy generation contour at production impeller exit – t=0.4T

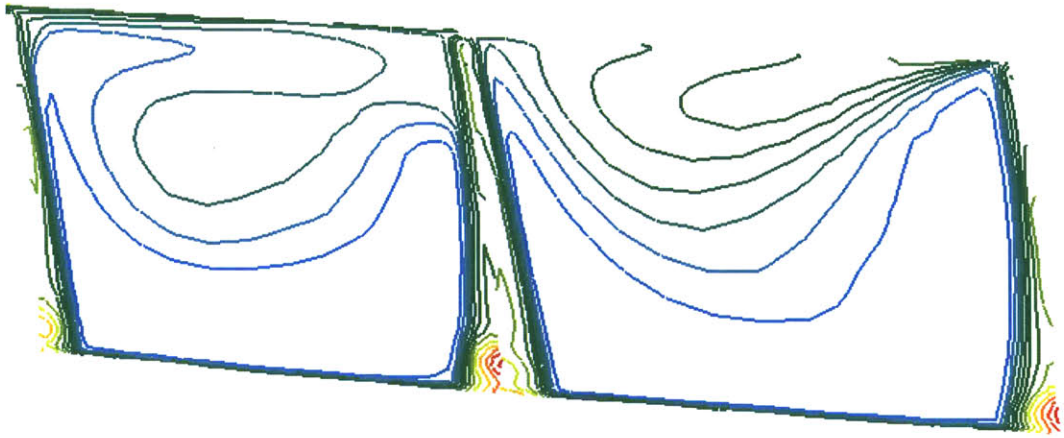

Figure 4.16c - Mass 2 - Entropy generation contour at production impeller exit – t=0.8T

Figure 4.17a - Mass 2 - Entropy generation contour at enhanced impeller exit – t=to

Figure 4.17b - Mass 2 - Entropy generation contour at enhanced impeller exit – t=0.4T

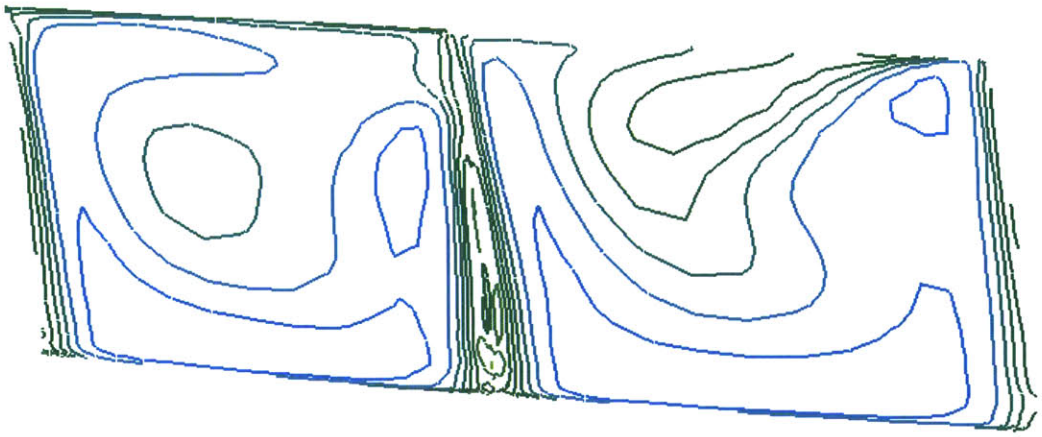

Figure 4.17c - Mass 2 - Entropy generation contour at enhanced impeller exit – t=0.8T

It has been established that the enhanced impeller has a lower mass-averaged entropy production than the production impeller. Figures 4.14 - 4.17 show the time-unsteady entropy production distribution at the impeller exit for the production and enhanced compressors at Mass 1 and Mass 2. It can be inferred from the impeller exit entropy distributions that the production design (at both Mass 1 and Mass 2) has a higher level of entropy generation than the enhanced design. This difference in entropy production is most apparent near the hub of the main and splitter blade pressure surface, where there is a region of high entropy generation in the production compressor and no such region in the enhanced compressor. This is consistent with the findings in Chapter 3 that the enhanced compressor has a lower mass-averaged entropy production and higher efficiency than the production compressor.

The entropy and Mach number distributions at the impeller exit are consistent with results from chapter 3 and with expected changes due to an increase in the impeller tip radius. These results show that there is a difference in the unsteady flow field of the two compressors at near the hub of the blade surfaces, particularly the splitter blades surfaces; a notable observation since the vibratory difficulty occurred on the enhanced splitter blade during testing.

4.3 The Impeller-Diffuser Gap (Vaneless Space)

4.3.1 Static Pressure Distribution

An interrogation of the unsteady blade loading on the impeller blades (Section 4.2.1) showed the differences between the production and enhanced impeller blade loading. This section interrogates the static pressure field in the impeller-diffuser gap of the production and enhanced compressors at Mass 1 and Mass 2. The purpose of this interrogation is to determine whether there are differences in the static pressure fields of the production and enhanced compressors throughout the entire impeller-diffuser gap. If differences exist throughout the entire gap, it could imply that the differences in the unsteady pressure field at the diffuser inlet propagate upstream to the impeller. These

propagated differences in the flow fields could in turn lead to the differences in the unsteady blade loading, and thus the observed difference in the forced response behavior of the two compressors.

To investigate the static pressure flow fields in the impeller-diffuser gap, the normalized static pressure distributions were computed for the entire annulus at 0%, 5%, 15%, 45%, 80%, 95%, and 100% of the vaneless space (where 0% corresponds to the impeller exit plane and 100% corresponds to the diffuser leading edge plane) for the production and enhanced compressors at Mass 1, and at 0%, 45%, and 100% span for the production and enhanced compressors at Mass 2. The static pressure distribution across the annulus at 5% vaneless space and 15% span, at one time instant, is shown in Figure 4.18 for the production and enhanced compressors at Mass 1 and in Figure 4.19 for the production and enhanced compressors at Mass 2. For these plots, the difference between the local static pressure and the inlet static pressure was normalized by the dynamic pressure head (based on the density at the impeller inlet and the impeller tip velocity). The ordinate of these plots is the normalized static pressure described above, minus the average normalized static pressure around the annulus. From these plots, it appears that there are spatial differences, but these differences are difficult to quantify. For a more quantitative comparison, the difference between the maximum and minimum normalized static pressures encountered around the annulus for each annular location is listed in Table 4.1, and the annulus-averaged normalized static pressure for each annular location is tabulated in Table 4.2.

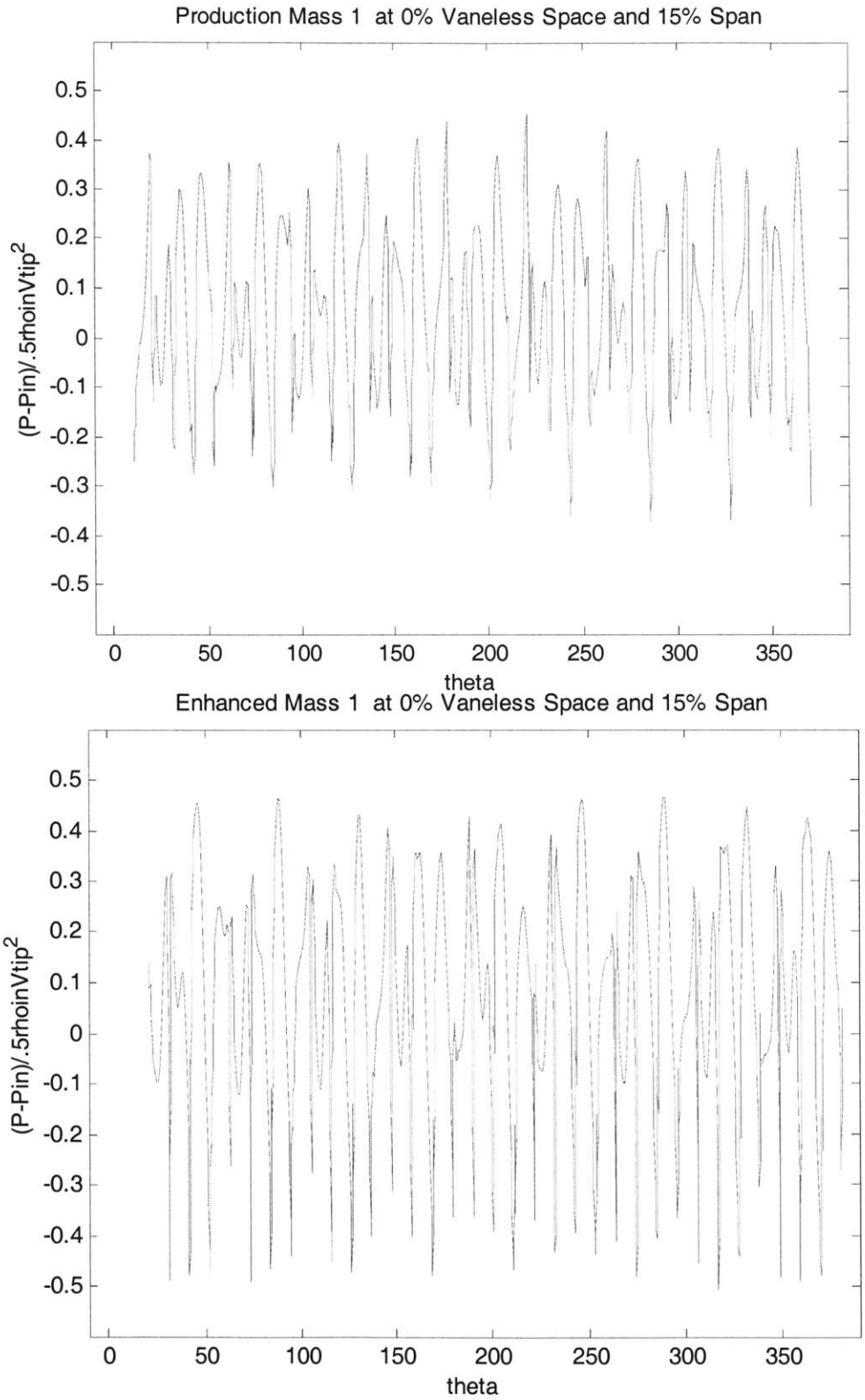

Figure 4.18 - Sample plots of the normalized static pressure distribution (minus the annulus-averaged value) around the annulus of the impeller-diffuser gap at Mass 1.

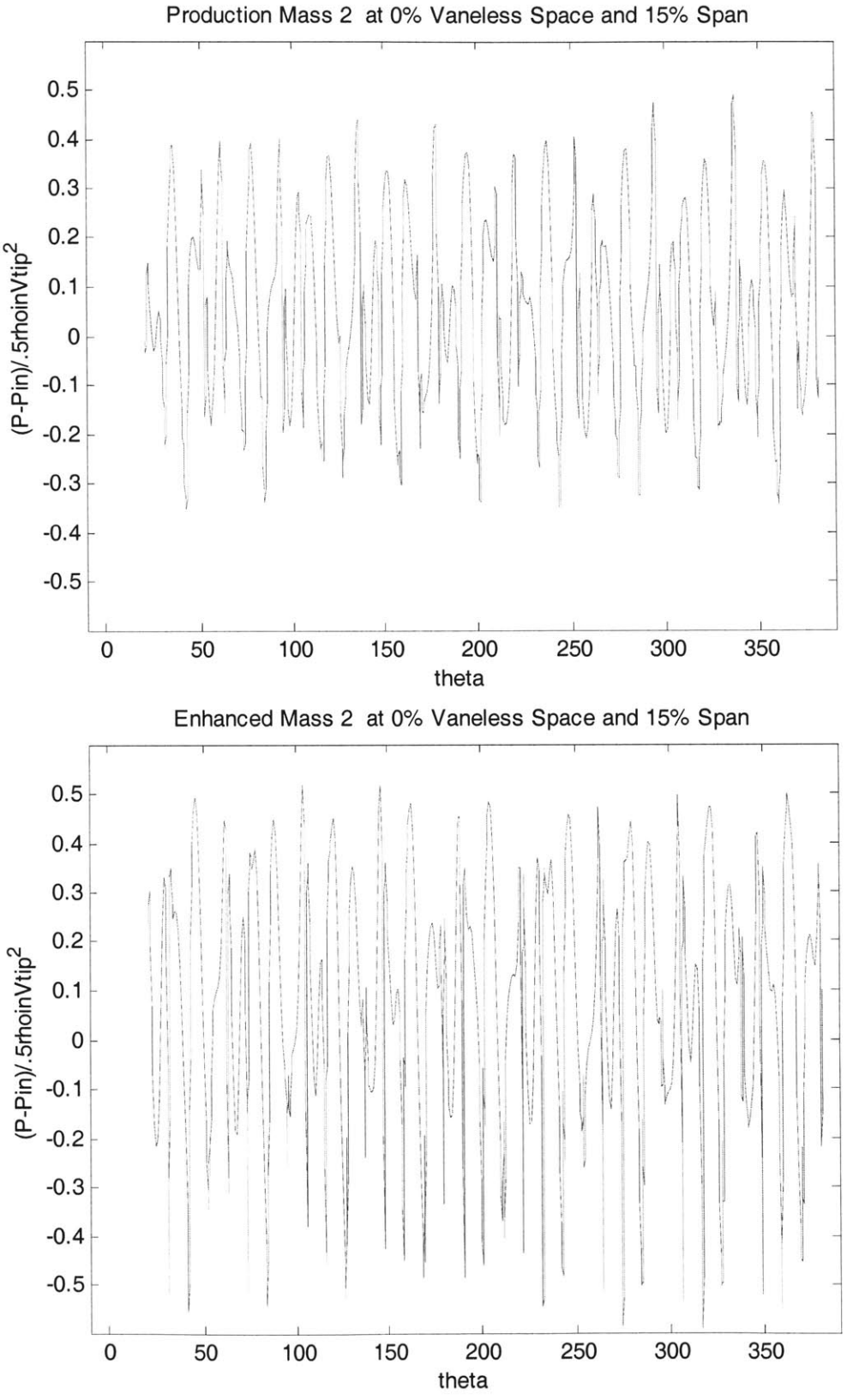

Figure 4.19 - Sample plots of the normalized static pressure distribution (minus the annulus-averaged value) around the annulus of the impeller-diffuser gap at Mass 2.

		Mass 1		Mass 2	
% Vaneless Space	% Span	Production	Enhanced	Production	Enhanced
0	15	.832	.974	.842	1.111
0	70	.572	.774	.624	.787
0	90	.553	.683	.529	.689
5	15	.721	.867		
5	70	.542	.672		
5	90	.550	.610		
15	15	.743	.835		
15	70	.524	.572		
15	90	.538	.593		
45	15	.754	.817	0.772	.887
45	70	.471	.513	0.500	.618
45	90	.494	.556	0.473	.556
80	15	.955	1.143		
80	70	.723	.893		
80	90	.605	.763		
95	15	1.322	1.524		
95	70	.995	1.210		
95	90	.813	1.014		
100	15	2.416	2.532	2.367	2.592
100	70	2.079	2.314	2.051	2.253
100	90	1.590	1.798	1.839	1.940

Table 4.1 – The difference of the maximum (P-Pin)/(.5*ρ_{in} *u_{tip}^2) across the annulus and the minimum (P-Pin)/(.5*ρ_{in} *u_{tip}^2) across the annulus.

		Mass 1		Mass 2	
% Vaneless Space	% Span	Production	Enhanced	Production	Enhanced
0	15	1.164	1.193	1.208	1.198
0	70	1.164	1.232	1.206	1.233
0	90	1.185	1.269	1.232	1.283
5	15	1.192	1.286		
5	70	1.202	1.305		
5	90	1.222	1.328		
15	15	1.220	1.340		
15	70	1.235	1.333		
15	90	1.250	1.352		
45	15	1.297	1.379	1.378	1.442
45	70	1.249	1.312	1.325	1.371
45	90	1.253	1.327	1.325	1.375
80	15	1.609	1.654		
80	70	1.512	1.565		
80	90	1.484	1.546		
95	15	1.734	1.777		
95	70	1.600	1.660		
95	90	1.530	1.594		
100	15	1.787	1.841	1.750	1.768
100	70	1.650	1.705	1.630	1.660
100	90	1.542	1.591	1.530	1.553

Table 4.2 - The annulus-averaged normalized static pressure at various spanwise and meridional locations within the impeller-diffuser gap.

There are three trends that can be deduced from Table 4.1. The first trend is that the difference between the maximum and minimum normalized static pressures (Pmax-Pmin) is greater in the enhanced compressor than the production compressor at each spanwise

and meridional location for a given corrected flow (Mass 1 or Mass 2). The second trend is that the pressure variations are highest at the diffuser inlet, they decrease towards upstream locations, then increase again as the location nears the impeller exit plane. Such a variation is to be expected. The last trend is that the pressure variations are highest near the hub.

In addition to the differences in Pmax-Pmin, there are differences in the average annulus-averaged normalized static pressure (Table 4.2). The first trend to be garnered from Table 4.2 is that for a given corrected flow, the enhanced compressor has a higher average static pressure than the production compressor at each spanwise, meridional location within the vaneless space, with the single exception of the impeller exit at 15% span at the Mass 2 corrected flow. For each compressor, for a given spanwise location, at each mass flow, the average normalized static pressure is lowest at the impeller inlet, and increases towards the diffuser inlet, where the average normalized static pressure is highest (as to be expected). Lastly, for each compressor, at a given mass flow, the normalized static pressure is highest near the hub from 45% of the vaneless space to the diffuser inlet; from 0% to 45% of the vaneless space, the normalized static pressure is highest near the shroud.

4.3.2 Spatial Harmonic Content

Taking the fast Fourier Transform (FFT) of the normalized static pressure distribution around the annulus at 0%, 45%, and 90% vaneless space yields the spatial harmonic content of the unsteady pressure patterns (shown in Figures 4.20 - 4.25). The harmonics that are excited are consistent with fact that the pressure pattern is caused by the interaction between the impeller and diffuser blades, because each harmonic excited is a multiple (or multiples of the sum or difference) of the impeller and diffuser blade counts as follows:

- 25 – the number of diffuser vanes
- 34 – the number of impeller main + impeller splitter blades
- 17 – the number of impeller passages (the number of main or splitter blades)

- 9 = 34-25
- 18 = 2*(34-25)
- 8 = 25-17
- 7= (17+25)/6

From the results presented in Figures 4.20 - 4.25, trends in the basic spatial pattern may be discerned that are consistent for the production and the enhanced compressors at Mass 1 and Mass 2. Each figure contains three plots, arranged such that the harmonic distribution plot at 15% span is at the top, and the harmonic distribution plot at 90% span is at the bottom. This organization shows the variations in the amplitudes of the harmonics with spanwise location. Figures 4.20 – 4.23 show that the trends in the basic spatial pattern that may be discerned are consistent for the production and the enhanced compressors at Mass 1 and Mass 2. The variation of the harmonics with radial distance along the impeller-diffuser gap can be inferred from a comparison of Figures 4.23 - 4.25. At the impeller exit (Figures 4.20-4.23), the spatial harmonic content is dominated by the 34^{th} and 25^{th} harmonic, and to a lesser extent, the 9^{th} harmonic. At 45% meridional distance (Figure 4.24) of the vaneless space, the influence of the 34^{th} harmonic has decayed, and the harmonic content is now dominated by the 25^{th} harmonic, with other contributions coming from the 18^{th}, 34^{th}, 9^{th}, 8^{th}, and 7^{th} harmonics. By the diffuser inlet (Figure 4.25), the 25^{th} harmonic has more than 6 times the influence of any other harmonic (note that the scale at 100% meridional distance of the vaneless space is different than at the other meridional locations, because the 25^{th} harmonic is so much more dominant). At each meridional location, the influence of the dominant frequency (or, in the case of the impeller exit, the influence of the two dominant frequencies) decreases from hub to shroud. This is consistent with the findings that Pmax-Pmin decreases from hub to shroud.

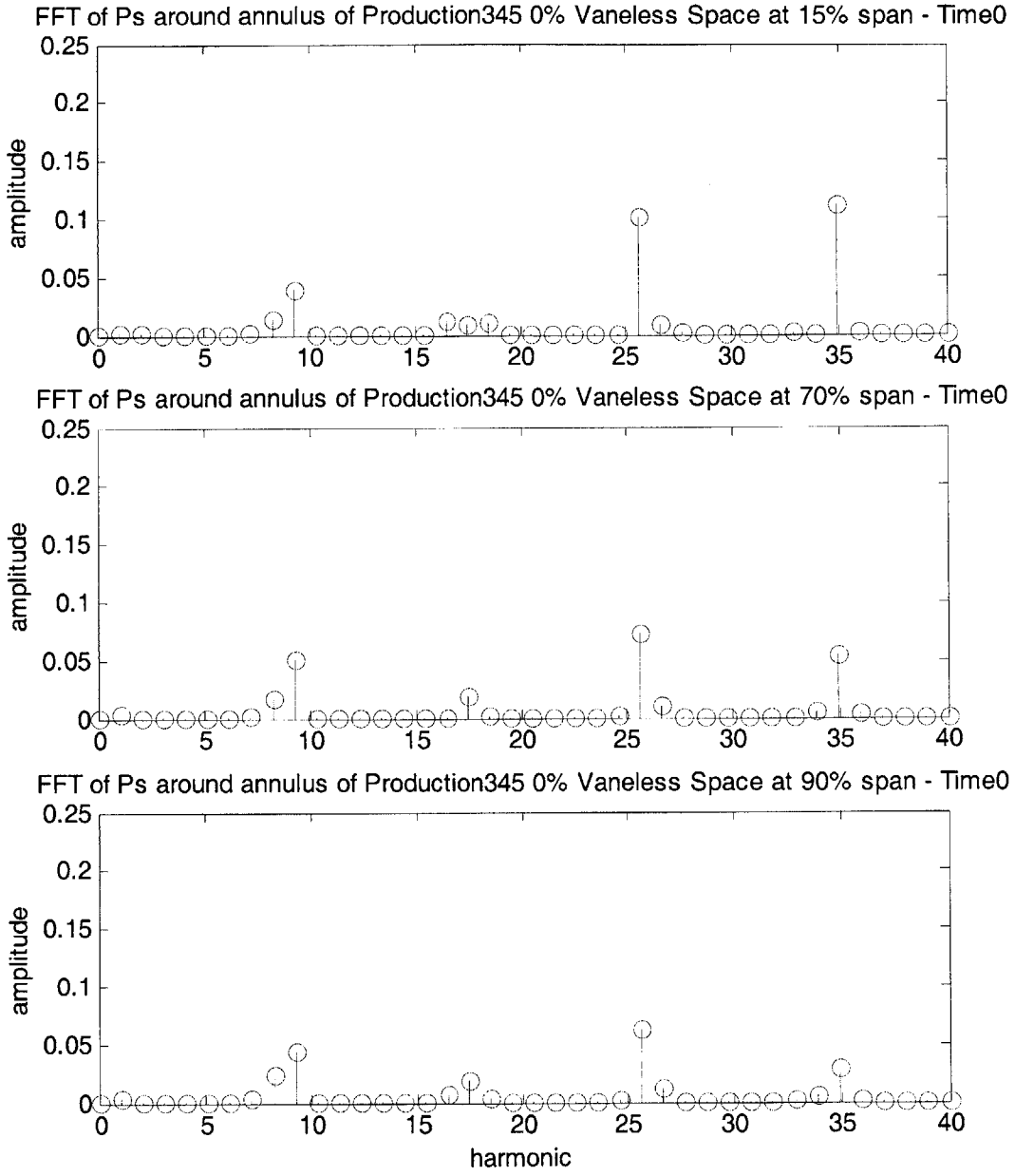

Figure 4.20 - Spatial harmonic content of static pressure at 0% meridional distance of the impeller-diffuser gap for the production compressor at Mass 1.

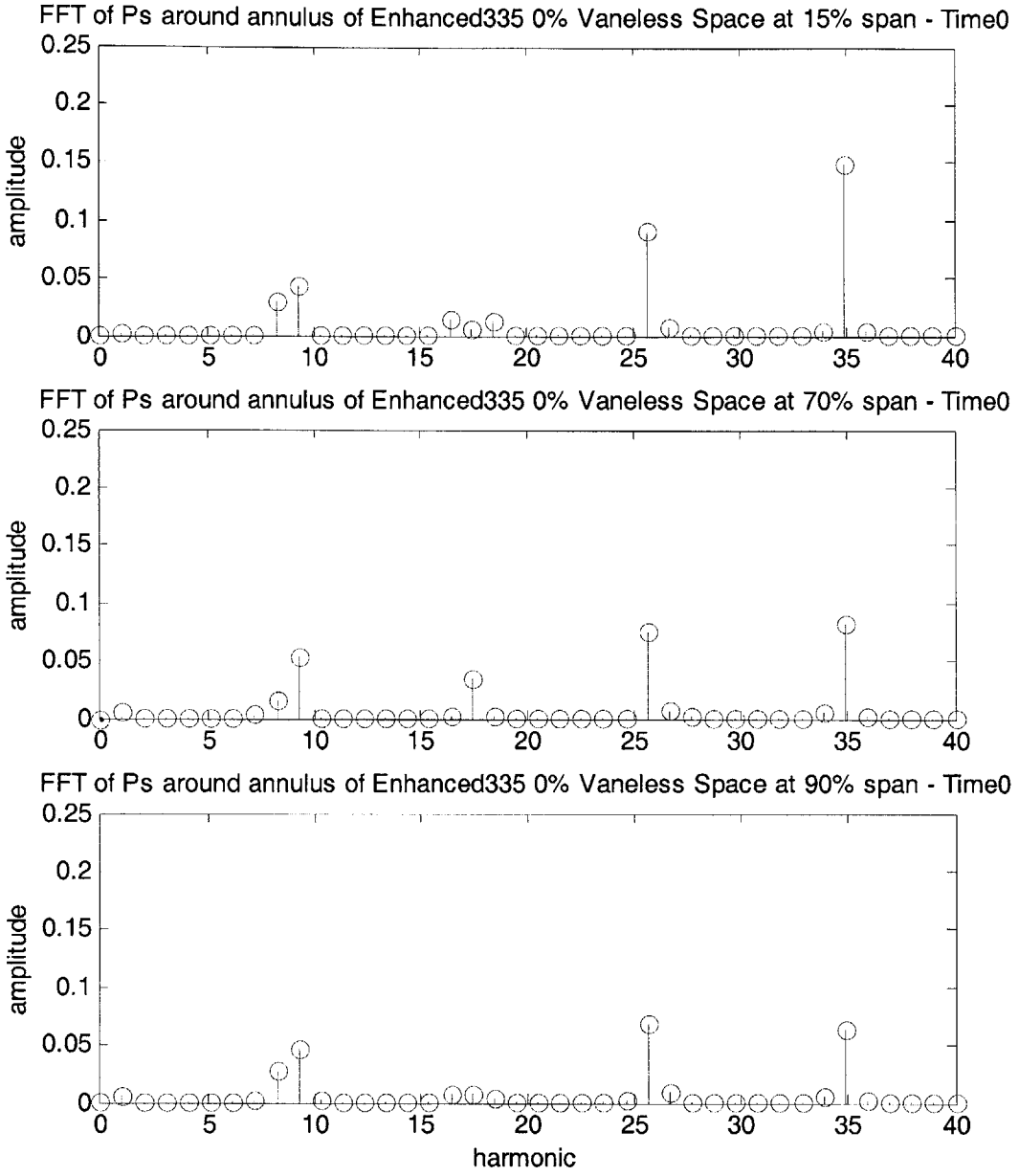

Figure 4.21 - Spatial harmonic content of static pressure at 0% meridional distance of the impeller-diffuser gap for the enhanced compressor at Mass 1.

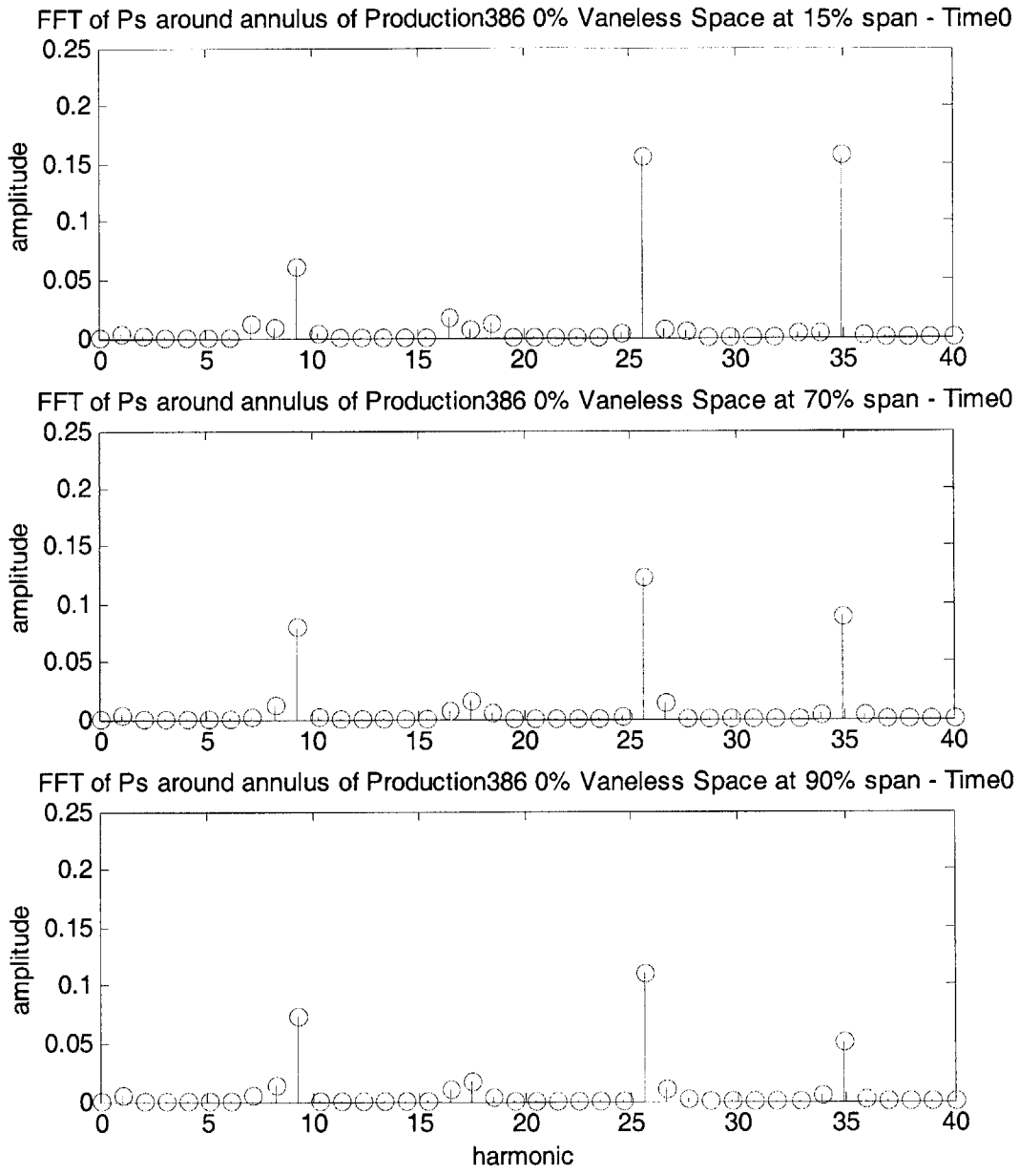

Figure 4.22 - Spatial harmonic content of static pressure at 0% meridional distance of the impeller-diffuser gap for the production compressor at Mass 2.

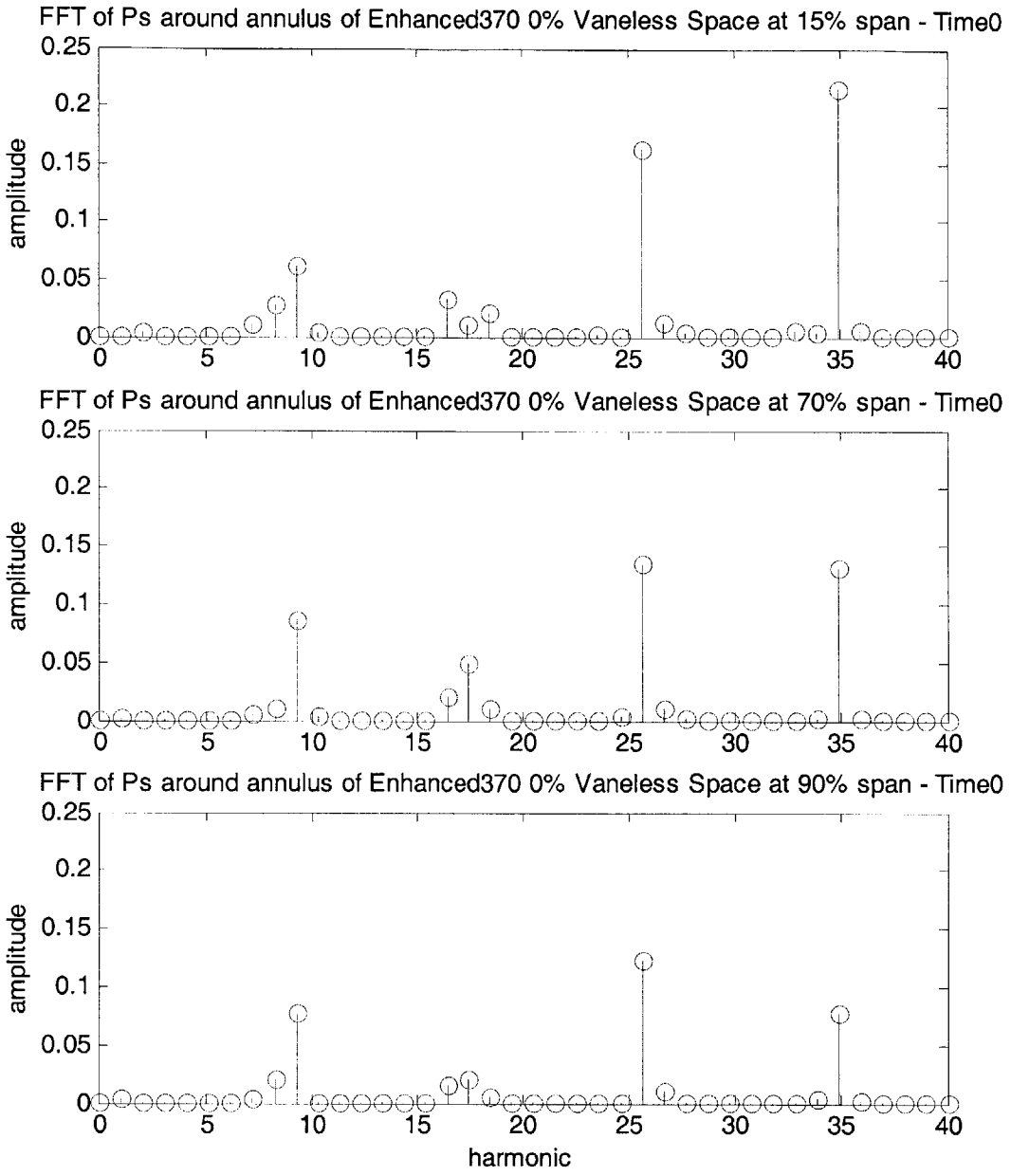

Figure 4.23 - Spatial harmonic content of static pressure at 0% meridional distance of the impeller-diffuser gap for the enhanced compressor at Mass 2.

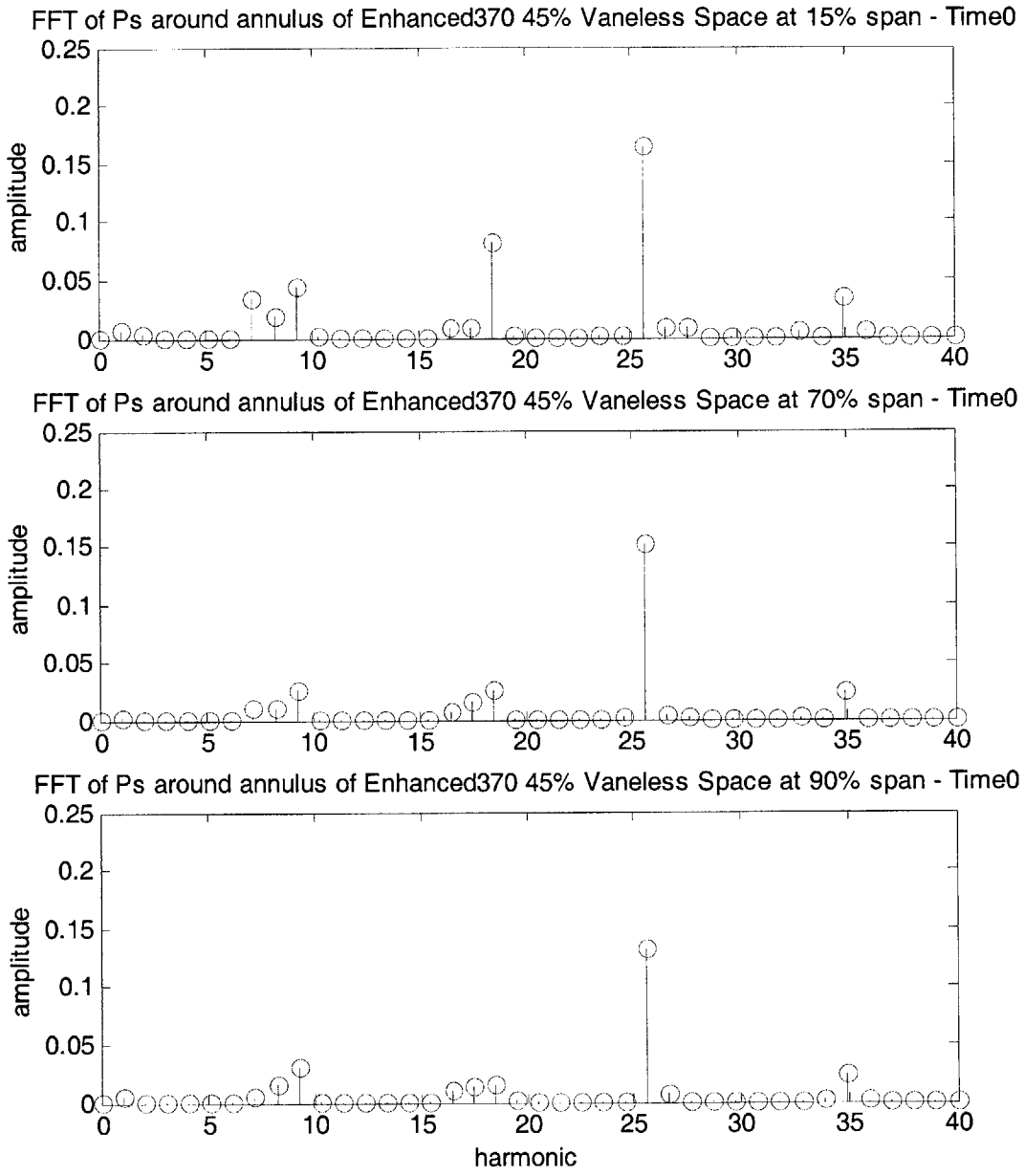

Figure 4.24 - Spatial harmonic content of static pressure at 45% meridional distance of the impeller-diffuser gap for the enhanced compressor at Mass 2.

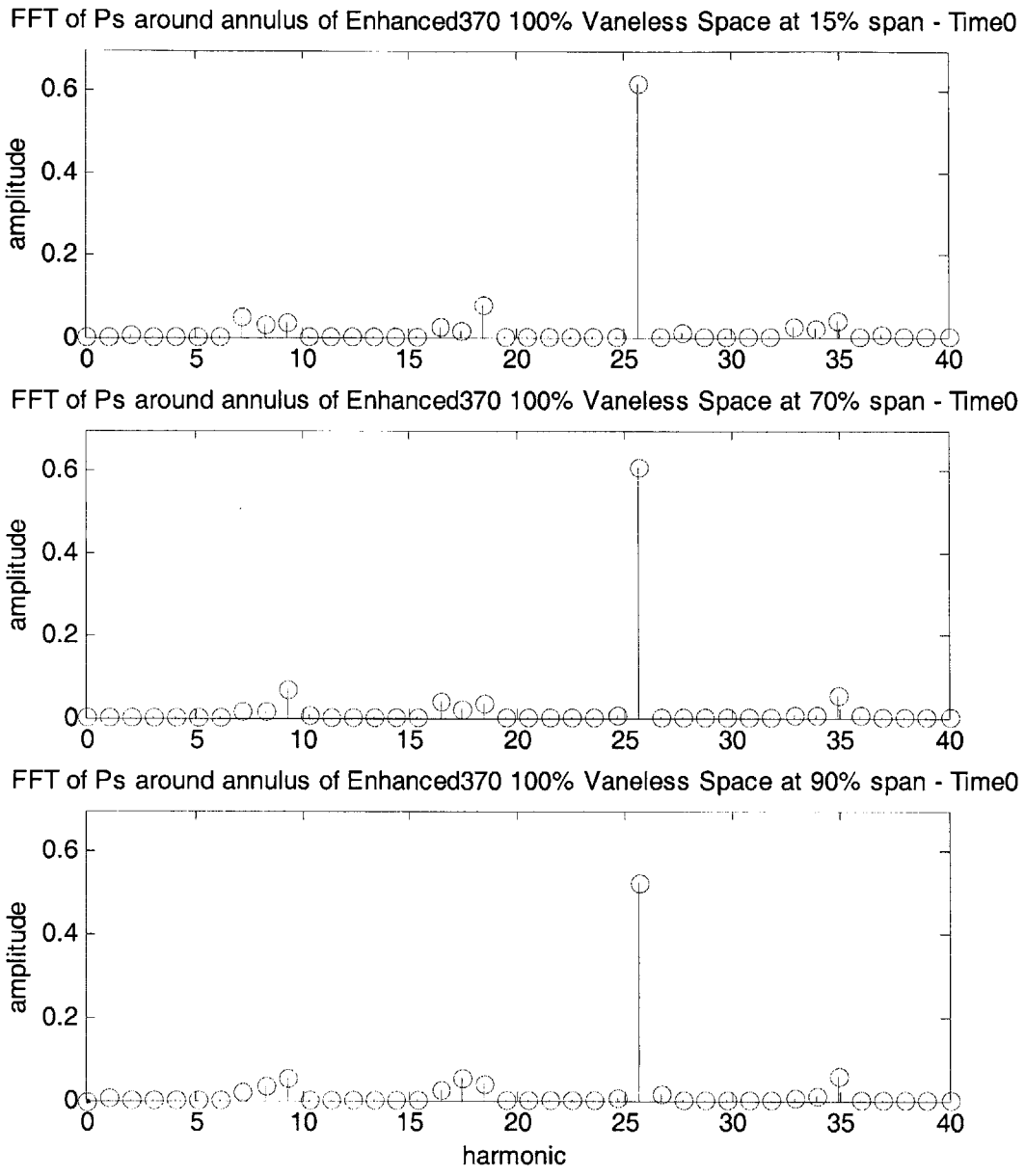

Figure 4.25 - Spatial harmonic content of static pressure at 100% meridional distance of the impeller-diffuser gap for enhanced compressor at Mass 2.

Despite these similarities in trends, there are some differences in the spatial harmonic content of the production and enhanced compressors; there are differences in the relative influence of the top 6 harmonics. For example, at the impeller exit, near the hub, the relative influence of the 25^{th} and 34^{th} harmonics is different between the two geometries.

At Mass 2, the 25th harmonic and the 34th harmonic have approximately the same influence in the production compressor (Figure 4.22), while in the enhanced compressor (Figure 4.23) the amplitude of the 25th harmonic is 75% of the amplitude of the 34th harmonic. The same trend is found at Mass 1, where in the production compressor (Figure 4.20) the amplitude of the 25th harmonic is 88% of the amplitude of the 34th harmonic, compared to a 25th to 34th harmonic amplitude ratio of 64% for the enhanced compressor (Figure 4.21). At 70% and 90% span, the 25th to 34th harmonic amplitude ratio is larger for the production compressor than the enhanced compressor at both Mass 1 and Mass 2. At 45%, the ratio of the 25th and 18th harmonic amplitudes is larger for the production compressor than for the enhanced compressor. These differences indicate a difference in spatial harmonic content in spite of the similarities described in the paragraph above.

4.4 The Diffuser Inlet Incidence Angle

In the previous section, it was noted that there are differences in the static pressure distribution in the impeller-diffuser gap of the two similar compressor designs (production and enhanced), from the impeller exit to the diffuser inlet, and in Section 3.3.2, it was noted that there is a difference in the momentum-averaged diffuser inlet incidence angle between the two compressors. The incidence angles for the production and enhanced geometries are tabulated in Table 4.3 for reference[3].

	Mass flow	Momentum-averaged incidence angle
Production	**Mass 1**	-20°
Enhanced	**Mass 1**	-19°
Production	**Mass 2**	-18°
Enhanced	**Mass 2**	-17°

Table 4.3 - Momentum-averaged diffuser inlet incidence angle

[3] The incidence angle is defined as the difference between the flow angle and the blade angle. In this analysis, the blade angle was estimated, introducing a possible source of error in the estimated incidence angle; however, this error is the same for both compressors. Because the error is the same for both compressors, the trends in this analysis still hold.

These differences in momentum-averaged incidence angle raise the question of whether or not the change in momentum-averaged incidence angle is indicative of a difference in the incidence angle distribution. The differences between the time-averaged incidence angle distribution of the production and enhanced compressors at Mass 1 and Mass 2 are shown in Figures 4.26 and 4.27 respectively.

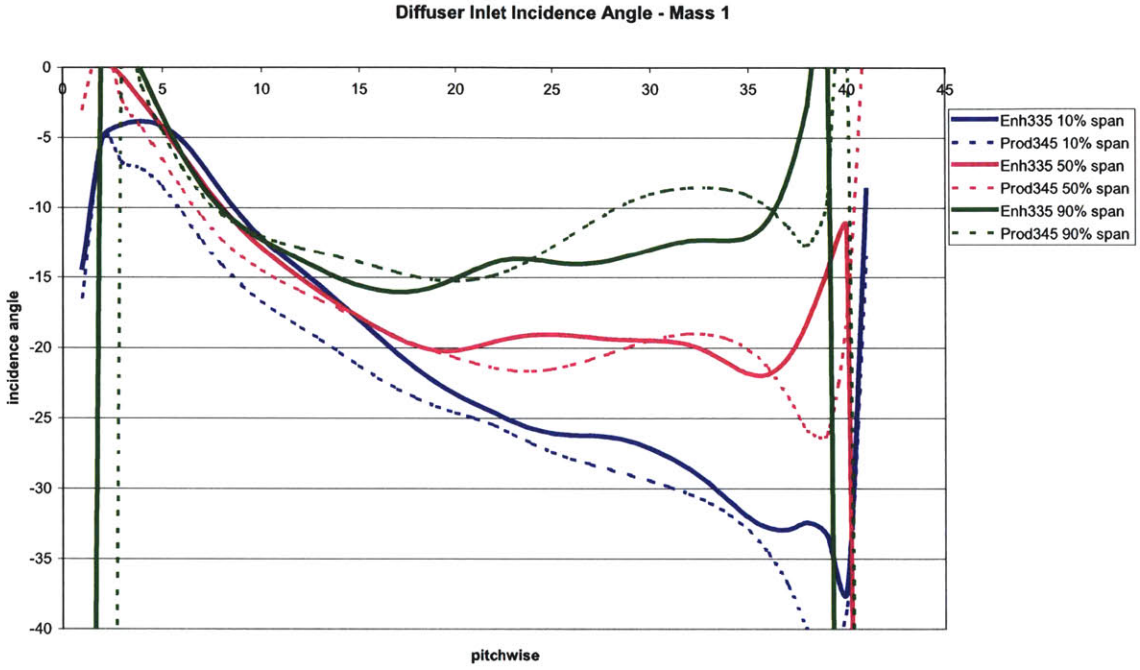

Figure 4.26 - Mass 1 diffuser inlet incidence angle.

In these figures, the solid lines correspond to the incidence angle distribution in the enhanced compressor, and the dashed lines correspond to the incidence angle distribution in the production compressor. For both compressors, the incidence angles at 90% span (near the shroud) are the least negative (green), the incidence angles near the hub are the most negative (blue), and the mid-span incidence angles (magenta) are in between. The general trends in the incidence angle distribution are similar for the production and enhanced compressors at Mass 1 and Mass 2. In general: the time-averaged incidence angle increases from hub to tip at a given pitchwise location, the incidence angles are approximately the same at all spanwise locations near the suction surface (SS) of the diffuser vanes (where SS is the same as the minimum pitchwise coordinate), and the

incidence angle decreases as the pitchwise location is moved from the suction surface into the diffuser passage then increases again as the pitchwise location nears the pressure surface. However, there are also differences in the diffuser inlet incidence angle distribution for the two similar compressor designs. One notable difference is that for both Mass 1 and Mass 2, the pitchwise location at which the incidence angles at 10% and 50% span diverge is further towards the center of the diffuser inlet plane for the enhanced compressor than for the production compressor. In other words, the incidence angle distribution for the diffuser of the enhanced compressor is more uniform in the spanwise direction from the suction surface to mid-pitch than the incidence angle distribution of the production compressor. The other notable difference is that the incidence angle distribution for the production and enhanced compressors differ once the incidence angles begin to diverge at approximately mid-span. The differences in the diverging portion of the incidence angle distributions are not the same for Mass 1 and Mass 2, but there are differences between the incidence angles of the production and the enhanced compressors at both corrected flows.

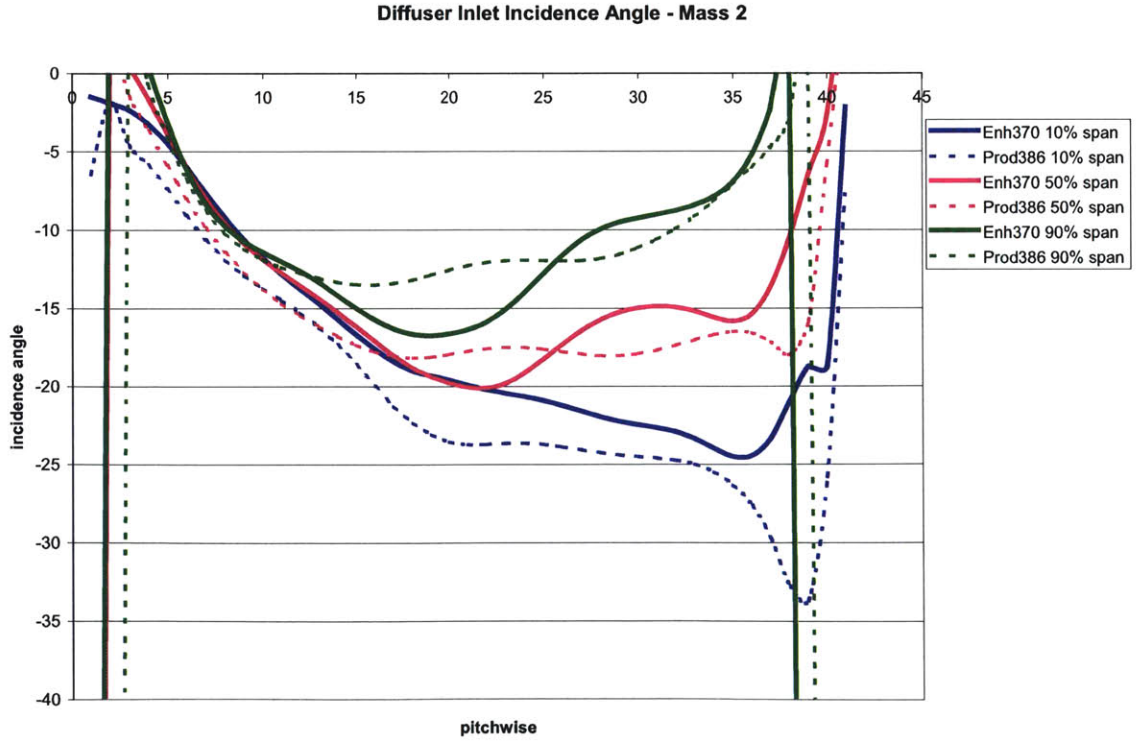

Figure 4.27 - Mass 2 diffuser inlet incidence angle.

For a quantitative comparison of the diffuser inlet incidence angles, the time-averaged, pitch-averaged incidence angles are tabulated in Table 4.4.

% span	Production Mass 1	Enhanced Mass 1	Production Mass 2	Enhanced Mass 2
10	-24°	-21°	-19°	-16°
20	-22°	-19°	-18°	-14°
30	-21°	-18°	-17°	-14°
50	-19°	-18°	-16°	-14°
70	-16°	-19°	-14°	-16°
80	-18°	-21°	-20°	-19°
90	-22°	-22°	-34°	-38°

Table 4.4 - Time-averaged, pitch-averaged (or gap-averaged) diffuser inlet incidence angle

From this table emerges a trend: for a given corrected flow, the time-averaged, gap-averaged diffuser inlet incidence angle is greater in the enhanced design than in the production design from the hub until somewhere around mid-span, at which point (the location of switch differs between the Mass 1 and Mass 2 results) the trend reverses, and the diffuser incidence angle is greater than the enhanced incidence angle. From the time-averaged and the time-averaged, pitch-averaged diffuser inlet incidence angle comparisons, it may be inferred that there are differences between the enhanced and production diffuser inlet incidence angle distributions.

4.5 Summary and Hypothesis

4.5.1 Summary

This chapter interrogated the unsteady flow fields in the impeller and in the impeller-diffuser diffuser gap (from the impeller exit to the diffuser inlet), in an effort to determine the root cause of the vibrations leading to HCF problems. These interrogations were performed by comparing the unsteady flow fields of two compressors of nearly identical

design (the production and enhanced designs) at two corrected flows: Mass 1 and Mass 2. It was found that there are differences in the unsteady flow fields of the production and enhanced compressors in the impeller passage, at the impeller exit, throughout the impeller-diffuser gap and at the diffuser inlet.

In the impeller passage, the blade loading on the impeller main and splitter blades of the two compressors were compared, yielding several trends. The first trend is that for the impeller main and splitter blades at a given corrected flow, the unsteadiness in the blade loading in the enhanced impeller is always greater than or equal to the unsteadiness in the blade loading in the production impeller. Secondly, it was found that the unsteadiness in a given compressor increases as the operating point is moved from design towards stall. Lastly, the steady blade loading (the portion of the blade loading that is independent of time) has different spatial patterns near the tip of the impeller blades of the production and enhanced compressors. At the impeller exit, differences were found in the entropy production distribution and the Mach number distribution. Although the average Mach number at the impeller exit is subsonic for the production and transonic for the enhanced, both compressors have regions of transonic flow. Despite this similarity, it was found that the jet Mach number at the enhanced impeller exit is higher than the jet Mach number at the production impeller exit. The production compressor was found to have regions of high entropy generation near the hub at the splitter blade trailing edge; no such region was found in the enhanced compressor.

Some similarities exist in both the static pressure distribution and the spatial harmonic content of the static pressure waves on the vaneless space of the production and enhanced compressors; however, differences were found as well. For a given corrected flow, the enhanced compressor has a both a larger difference between the maximum and minimum static pressure at a given spanwise, meridional location and a higher average static pressure than the production compressor at each spanwise, meridional location within the vaneless space. In addition, differences were found in the relative influence of the 6 most influential harmonics.

Finally, the time-averaged diffuser inlet incidence angle was analyzed. The time-averaged diffuser inlet incidence angle distributions in the production and enhanced compressors were found to have differences. In addition, the time-averaged, pitch-averaged incidence angle distribution for the production and enhanced compressors were found to have differences: the incidence angle is greater in the enhanced design than in the production design from the hub until somewhere around mid-span, at which point the trend reverses, and the diffuser incidence angle is greater than the enhanced incidence angle.

4.5.2 Hypothesis

Although causality has not been established, a hypothesis has been formulated to explain the observed difference in the aeromechanic response of the production and enhanced impeller splitter blades based on the findings summarized above. It is hypothesized that the differences in the time-averaged incidence angle distribution at the diffuser inlet for the two designs result in differences in the unsteady static pressure distribution. These differences in the unsteady pressure distribution are propagated upstream, leading to the observed difference in the unsteady pressure distribution at the impeller trailing edge region. This unsteady pressure distribution is the excitation source for forced response, and thus the difference in incidence angle distribution between the production and compressor design could result in the observed aeromechanical difficulty in the enhanced compressor where there had been no such difficulty in the production compressor.

Chapter 5

Summary and Conclusions

5.1 Summary

A computational interrogation of the time-averaged and time-unsteady flow fields of two centrifugal compressors of nearly identical design has been undertaken in an effort to establish a causal link between impeller-diffuser interaction and the forced response behavior of the impeller blades. In this chapter, the contributions are outlined and the results are summarized. A hypothesis is then put forth regarding the causal link between impeller-diffuser interactions and aeromechanical difficulties. Finally, recommendations for future study are delineated.

5.2 Summary of Results and Hypothesis

The main contributions of this thesis are twofold. First, MSU Turbo was assessed as a computational tool for analyzing the unsteady flow fields and the time-averaged performance of centrifugal compressors; this assessment includes an assessment of MSU Turbo as part of a CFD/ FEA system for estimating strain in centrifugal impeller blades. Secondly, from an interrogation of the unsteady flow field of two compressors of nearly identical design, a hypothesis was formulated as to the causal link between IDI and the forced response behavior of impeller blades.

5.2.1 Assessment of MSU Turbo

Through assessments of MSU Turbo as a stand-alone CFD code, is was found that the trends in the time-averaged flow variables and performance metrics calculated in TURBO are in accord with data from test rigs, with ADPAC simulation results, and with trends reported in the literature. Based on these assessments, it is argued that the MSU Turbo CFD code is adequate to the task of distinguishing the unsteady flow fields of two

similar centrifugal compressor designs. Based on this argument, it can be inferred that MSU Turbo can be a useful tool in establishing a causal link between IDI and the forced response behavior of impeller blades. TURBO can help in establishing this link by enabling a comparison of the unsteady flow fields of two nearly identical compressors, one of which encountered aeromechanical difficulty, and the other of which did not. Through comparisons of TURBO/ ANSYS® estimates of strain with measured peak strain, MSU Turbo is also found to have the potential, as part of a CFD/ ANSYS® system, for serving as a predictive tool for forced response behavior in centrifugal compressors.

5.2.2 Unsteady flow field: Results and Hypothesis

Differences were found in the unsteady flow fields of two compressors of nearly identical design, only one of which encountered aeromechanical difficulty. These differences were found in the impeller passage, at the impeller exit, throughout the impeller-diffuser gap, and at the diffuser inlet.

- In the impeller passages, it was found that unsteadiness in the blade loading was greater for the compressor that experienced aeromechanical difficulty.
- At the impeller exit, it was found that there were differences in the Mach number distribution; the jet Mach number is higher at the enhanced impeller exit than at the production impeller exit, and there is a smaller gradient in Mach number both along the blade trailing edge and across the blade trailing edge for the production geometry, as compared to the gradients in the enhanced compressor
- In the impeller-diffuser gap, differences were found in the static pressure distribution and in the spatial harmonic content[4] of the production and enhanced compressors. It was found that in the compressor (enhanced) encountering aeromechanical difficulty, there is a larger difference in static pressure and a higher average static pressure on a given annular plane than in the compressor (production) encountering no such difficulty.

[4] Note that for the spatial harmonic content, the same six harmonics are excited. A difference in the spatial harmonic content refers to the differences in the relative amplitudes (i.e. which harmonic is dominant).

- Differences were found in the time-averaged and in the time- and pitch-averaged diffuser inlet incidence angle distributions. The time-averaged, pitch-averaged incidence angles were found to be greater in the enhanced design than in the production design until somewhere around mid-span. At this, point the trend reverses, and the diffuser inlet incidence angle is found to be greater in the production design.

Based on these observations, it is hypothesized that the difference in the time-averaged incidence angle distributions of the production and enhanced compressor designs causes differences in the unsteady static pressure field at the diffuser inlet. These differences in the unsteady flow field are then propagated upstream to the impeller, where they cause differences in the unsteady blade loading of the two impellers. This unsteady blade loading is the excitation source for the forced response of the impeller blades; thus, differences in the unsteady blade loading then lead to the observed forced response behavior in the two designs. In summary, it is hypothesized that the forced response behavior of the impeller blades is linked to the diffuser inlet incidence angle distribution.

5.3 Recommendations for Future Work

5.3.1 The TURBO/ ANSYS® System

The results presented have shown that the TURBO/ANSYS® system shows promise as a tool for predicting the forced response behavior. However, additional assessments of this system should be performed, in which the sources of error in this analysis are eliminated, or at least mitigated. Such a project should meet the following criteria:

- Capture blade-to-blade variations during testing, using advanced measurement techniques rather than strain gauges.
- Obtain precise information about the precise operating points at which strain measurements are taken and at which the aerodynamic tests are performed, particularly the corrected flow.

- Explore the difference in strain estimates from using damping coefficients estimates using various damping estimation techniques.

5.3.2 Unsteady Flow Field Analysis

Although a hypothesis regarding the causal link between impeller-diffuser interactions and aeromechanical difficulties has been put forth, causality has not been established. Therefore, future programs of study on this subject are recommended. Possible future investigation of this causal link might include the following:

- A further investigation of the unsteady flow fields of the production and enhanced compressors used as research vehicles in this thesis.
- An investigation of at least on other pair of centrifugal compressors of similar design, one of which encountered aeromechanical difficulty where the other did not, to determine if these differences in incidence angle distribution and pressure pattern are repeated in a different set of compressors.
- An investigation into the effects of changing the diffuser blade angle (and thus the incidence angle) on the forced response of the impeller blades.

Bibliography

[1] Cumpsty, N.A. *Compressor Aerodynamics.* Krieger Publishing Company, Malabar, FL, 2004.

[2] Kerrebrock, J. *Aircraft Engines and Gas Turbines.* The MIT Press, Cambridge, MA, London, England, 2001.

[3] Krain, H. "A Study on Centrifugal Impeller and Diffuser Flow," *ASME Journal of Engineering for Power, Vol. 103* (1981), pp. 688-697

[4] Krain, H., 1981 "A Study of Centrifugal Impeller and Diffuser Flow," ASME Paper 81-GT-9.

[5] Hah, C., Bryans A. C., Moussa, Z., Tomsho, M. E., 1988, "Application of Viscous Flow Computations for the Aerodynamic Performance of a Backswept Impeller at Various Operating Conditions," *ASME Journal of Turbomachinery*, Vol. 110, pp. 303-311.

[6] Hah, C., Krain, H., 1989, Secondary Flows and Vortex Motions in a High-Efficiency Backswept Impeller at Design and Off-Design Conditions," ASME Paper 89-GT-181.

[7] Dawes, W. N., 1995, "A Simulation of the Unsteady Interaction of a Centrifugal Impeller with its Vaned Diffuser: Flow Analysis," *ASME Journal of Turbomachinery*, Vol. 117, pp. 213-222.

[8] Domercq, O., and Thomas, R., 1997, "Unsteady Flow Investigation in Transonic Centrifugal Compressor Stage," AIAA Paper No. 97-2877.

[9] Hathaway, M. D., Wood, J. R., Wasserbauer, C.A., 1992, "NASA Low-Speed Centrifugal Compressor For Three-Dimensional Viscous Code Assessment And Fundamental Flow Physics Research", *ASME Journal of Turbomachinery*, Vol. 11, No. 2.

[10] Chriss, R. M., Hathaway, M. D., Wood, J. R., 1994, "Experimental and Computational Results from the NASA Lewis Low-Speed Centrifugal Impeller at Design and Part Flow Conditions," ASME Paper 94-GT-213.

[11] Kirtley, K., and Beach, T., 1992, "Deterministic Blade Row Interactions in a Centrifugal Compressor Stage," *ASME Journal of Turbomachinery*, Vol. 114, pp. 304-311.

[12] Filipenco, V.G., *Experimental Investigation of Flow Distortion Effects on the Performance of Radial Discreet-Passage Diffusers*, Massachusetts Institute of Technology, GTL Report #206, Cambridge, MA (PhD. Thesis), 1991.

[13] Rodgers, C., 1982, "The Performance of Centrifugal Compressor Channel Diffusers," ASME Paper 82-GT-10.

[14] Clements, A., Artt, D., 1989, "The Influence of Diffuser Vane Leading Edge Geometry on the Performance of a Centrifugal Compressor," ASME paper 89-GT-163.

[15] Waterman, W., AFOSR Workshop on "Inherence Nonsteadiness in Compressors and Turbines," Purdue University, 1993.

[16] Skoch, G., "Experimental Investigation of Diffuser Hub Injection to Improve Centrifugal Compressor Stability," *ASME Journal of Turbomachinery,* Vol. 127, January 2005.

[17] Phillips, M. "A Computational Investigation of the Effects of Inlet Flow Conditions on Vaned Diffuser Performance," Master Thesis, Massachusetts, Massachusetts Institute of Technology, 1997.
[18] Shum, Y.K, "Impeller-Diffuser Interaction in Centrifugal Compressors," PhD Thesis, Massachusetts Institute of Technology, 2000.
[19] Shum, Y. K., Tan, C. S., Cumpsty, N. A., 2000, "Impeller-Diffuser Interaction in a Centrifugal Compressor," *ASME Journal of Turbomachinery*, Vol. 122, No. 4.
[20] Ziegler, K., Gallus, H., Niehuis, R., "A Study in Impeller-Diffuser Interaction: Part I – Influence on the Performance", ASME GT-2002-30381.
[21] Ziegler, K., Gallus, H., Niehuis, R., "A Study in Impeller-Diffuser Interaction: Part II – Detailed Flow Analysis", ASME GT-2002-30382.
[22] Murray, N.P., "Effects of Impeller-Diffuser Interaction of Centrifugal Compressor Performance," Masters Thesis, Massachusetts Institute of Technology, 2003.
[23] Murray, N., Tan, C. S., "Aeromechanic Implications Associated With Time-Average Effect of Impeller-Diffuser Interaction on Centrifugal Compressor Performance," *Proceedings of the 9th National Turbine Engine High Cycle Fatigue Conference*, Pinehurst, NC, March 2004
[24] Sheng, C., 2004, "Full Annulus simulations of a high-Speed Centrifugal Compressor Using and Unstructured RANS Flow Solver," ASME Paper GT2004-53657.
[25] Mansour, M., Kruse, M., "Time Unsteady Impeller-Diffuser Interaction in Gas Turbine Engines," *Proceedings of the 5th National Turbine Engine High Cycle Fatigue (HCF) Conference*, Chandler, AZ, March 7, 2000.
[26] Chen, J. P., Briley, W.R., "A Parallel Flow Solver for Unsteady Multiple Blade Row Turbomachinery Simulations," *Proceedings of ASME TURBO Expo 2001*, New Orleans, LA, June 4-7, 2001.
[27] Hall, E. J., Heidegger, N. J., Delaney, R. A., "ADPAC v1.0 – User's Manual," NASA CR 206600, 1999
[28] Personal communication with Josef Panovsky, 2005
[29] Thompson, W.T., Dahleh, M.D., *Theory of Vibration with Applications.* Prentice Hall, Upper Saddle River, NJ, 1998.
[30] AFRL, *"Characterization of Aeromechanic Response and Instability in High Performance Centrifugal Compressor Stage/ Rocket Pump,"* Annual HCF Report Prepared for the U.S. Air Force, AFRL, 2003
[31] Personal communication with Jong Liu, 2005